LONGWAVE RADIATIVE TRANSFER IN THE ATMOSPHERE: MODEL DEVELOPMENT AND APPLICATIONS

A

THESIS

Presented to the Faculty

of the University of Alaska Fairbanks

in Partial Fulfillment of the Requirements

for the Degree of

DOCTOR OF PHILOSOPHY

By

Jennifer S. Delamere, B.A.

Fairbanks, Alaska

May 2003

ProQuest Information and Learning Company
300 North Zeeb Road
P.O. Box 1346
Ann Arbor, MI 48106-1346

LONGWAVE RADIATIVE TRANSFER IN THE ATMOSPHERE: MODEL DEVELOPMENT AND APPLICATIONS

By

Jennifer S. Delamere

RECOMMENDED:

Advisory Committee Chair

Chair, Department of Physics

APPROVED:

Dean, College of Science, Engineering and Mathematics

Dean of the Graduate School

5-5-03

Date

Abstract

A FLexible Radiative Transfer Tool (FLRTT) has been developed to facilitate the construction of longwave, correlated *k*-distribution, radiative transfer models. The correlated *k*-distribution method is a technique which accelerates calculations of radiances, fluxes, and cooling rates in inhomogeneous atmospheres; therefore, correlated *k*-distribution models are appropriate for simulations of satellite radiances and inclusion into general circulation models. FLRTT was used to build two new rapid radiative transfer models, RRTM_HIRS and RRTM_v3.0, which maintain accuracy comparable to the line-by-line radiative transfer model LBLRTM.

Iacono et al. [2003] evaluated upper tropospheric water vapor (UTWV) simulated by the National Center for Atmospheric Research Community Climate Model, CCM3, by comparing modeled, clear-sky brightness-temperatures to those observed from space by the High-resolution Radiation Sounder (HIRS). CCM3 was modified to utilize the rapid radiative transfer model RRTM and the separate satellite-radiance module, RRTM_HIRS, which calculates brightness temperatures in two HIRS channels. By incorporating these accurate radiative transfer models into CCM3, the longwave radiative transfer calculations have been removed as a significant source of error in the simulations. An important result of this study is that CCM3 exhibits moist and dry discrepancies in UTWV of 50% in particular climatic regions, which may be attributed to errors in the CCM3 dynamical schemes.

RRTM_v3.0, an update of RRTM, is a rapid longwave radiative transfer appropriate for use in general circulation models. Fluxes calculated by RRTM_v3.0 agree with those computed by the LBLRTM to within 1.0 W/m^2 at all levels, and the computed cooling rates agree to within 0.1 K/day and 0.3 K/day in the troposphere and stratosphere, respectively.

This thesis also assessed and improved the modeling of clear-sky, longwave radiative fluxes at the Atmospheric Radiation Measurement Program North Slope of Alaska site by simultaneously addressing the specification of the atmosphere, radiometric measurements, and radiative transfer modeling. Consistent with findings from other field sites, the specification of the atmospheric water vapor is found to be a large source of uncertainty in modeled radiances and fluxes. Improvements in the specification of carbon dioxide optical depths within LBLRTM resulted, in part, from this analysis.

Table of Contents

List of Figures

List of Tables

List of Acronyms

AER Atmospheric and Environmental Research, Inc.

ARM Department of Energy Atmospheric Radiation Measurement Program

AERI Atmospheric Emitted Radiance Interferometer

AERI-ER Extended-Range Atmospheric Emitted Radiance Interferometer

ARSCL VAP Active Remotely-Sensed Clouds Locations Value-Added Product

ASR Absolute Sky-scanning Radiometer

BBSS Balloon-Borne Sounding System

CCM3 National Center for Atmospheric Research Community Climate Model 3

CHARTS Code for High-Resolution Accelerated Radiative Transfer

DJF December, January, February

DU dobson units

ECMWF European Center for Medium-Range Weather Forecasts

FGM FLRTT-Generated Model

FLRTT Flexible Radiative Transfer Tool

GCM General Circulation Model

HIRS High Resolution Infrared Sounder

ICRCCM Intercomparison of Radiation Codes in Climate Models

IPASRC-I The First International Pyrgeometer and Absolute Sky-scanning Radiometer Comparison

IPASRC-II The Second International Pyrgeometer and Absolute Sky-scanning Radiometer Comparison

IWV Integrated column of water vapor

JJA June, July, August

LBLRTM Line-by-Line Radiative Transfer Model

MLS mid-latitude summer

MLW mid-latitude winter

MSD Original Vaisala sonde scaled to MWR

MWR Microwave Radiometer

NOAA CMDL National Oceanic and Atmospheric Administration Climate Monitoring and Diagnostics Laboratory

NSA CART North Slope of Alaska Cloud and Radiation Testbed

NWP Numerical Weather Predication Model

OSD Original Vaisala sonde

PIR Precision Infrared Radiometer

PIRd Precision Infrared Radiometer - Diffuse Measurement

PPMV parts per million by volume

QME Quality Measurement Experiment

RRTM Rapid Radiative Transfer Model

RRTMSW Shortwave Rapid Radiative Transfer Model

SAS sub-arctic summer

SAW sub-arctic winter

SHEBA Surface Heat Budget of the Arctic Ocean Project

SGP CART Southern Great Plains Cloud and Radiation Testbed

TOGA COARE Tropical Ocean and Global Atmosphere Coupled Ocean-Atmosphere Experiment

TRP tropical

TOMS Total Ozone Mapping Spectrometer

UTWV upper-tropospheric water vapor

VSD Original Vaisala sonde with Vaisala water vapor correction applied

Acknowledgements

This thesis work has been supported by a great crew of people from Fairbanks, Alaska to Boulder, Colorado, to Hoboken, New Jersey, to Cambridge and Lexington, Massachusetts. Foremost, I would like to thank my committee chair, Knut Stamnes, for not only his guidance in translating the complexities of radiative transfer into operational radiative transfer models, but also for his many thoughtful comments on the content of this thesis. I also thank Knut for the many opportunities he afforded me to travel from 70^{-1} South to 70^{-1} North. To my other committee members, Hans Nielsen, John Olson, and Brenton Watkins, thank you for serving on my committee and offering comments on this dense thesis.

In December, 1999, I had the opportunity to begin full-time employment with Atmospheric and Environmental Research, Inc. (AER), in Cambridge, Massachusetts. While I was saddened to leave my colleagues at the University of Alaska Fairbanks, I also looked forward to the new challenges presented to me at AER, Inc. My colleagues at AER, Inc. have played an enormous role in this thesis. My supervisor, Tony Clough, and colleague, Eli Mlawer, spent many hours discussing the construction of the FLexible Radiative Transfer Tool (FLRTT), the update of the rapid radiative transfer model RRTM, and closely examining the frenzied plots comparing high-resolution spectral calculations to observations. Their contributions are heavily reflected in the contents of Chapters 2 and 5. I would also like to commend Mike Iacono for the high-quality research he has undertaken in evaluating climate model simulations against satellite radiance observations. This work, which utilized a radiative transfer tool constructed by FLRTT, is described in Chapter 3 and will soon be published in Journal of Geophysical Research [*Iacono et al.*, 2003]. I also thank Karen Cady-Pereira for the computing and design effort she put forth in the rebuild of RRTM, as well as Mark Shephard and Pat Brown for providing assistance with the line-by-line radiative transfer model LBLRTM and computer support.

The research presented in Chapter 5 was inspired, in part, by the Second International Pyrgeometer and Absolute Sky-scanning Radiometer Comparison (IPASRC-II) [*Marty et al.*, 2003]. This effort was led by Christoph Marty and Rolf Philipona, and has resulted in a number of important conclusions about the quality of data obtained from pyrgeometers operating in Arctic environments. Rune Storvold was instrumental, indeed, in this re-

search work as he provided many details on not only the configuration of the North Slope of Alaska ARM site itself, but also on the performance of the instruments operating there.

I also extend thanks to those many friends who contributed to this thesis by either tossing me frisbees between plot-making episodes, having lunch with me at West Ridge Cafe when I needed a break from writing computer code, or just lending advice on the topic du jour. To my mother, I thank you for insisting that I continue my education when I wanted to quit kindergarten because I wasn't selected to be Little Red Riding Hood in the afternoon play. To my father, I thank you for providing to me a wonderful path of education through Phillips Exeter Academy, Johns Hopkins University, and the University of Alaska Fairbanks. To Sheila and Alan Delamere, thank you for providing so many meals and lattes in this last year while I have been writing this thesis.

Lastly, thanks to my husband, Peter. No written acknowledgements can express the gratitude I have to you for encouraging me to finish this thesis as we moved from Fairbanks to Boston to Boulder. And to my young son, Sam, while your sleeping patterns have remained nearly as they were since the day you were born!, your continued growth and expressions astound me daily. And, Sam, if you ever pursue your Ph.D., you have two parents who will know the challenges and rewards of such an endeavour.

Chapter 1

Introduction

Radiative energy emitted by the Sun and absorbed by the earth's atmosphere and surface fuels the earth's climate system. However, to maintain radiative equilibrium over long time periods requires the atmosphere-surface system to emit radiation back to space. The radiation emitted by the sun and the radiation emitted by the earth's atmosphere-surface system come from two distinct portions of the electromagnetic spectrum due to the difference in temperature of the emitters. The solar (or shortwave) radiation spectrum extends from 0.2 to 3.5 μm, peaking at 0.5 μm, whereas the terrestrial (or longwave) radiation spectrum extends from 3.5 to 100 μm, peaking at 11 μm. There is negligible overlap between the shortwave and longwave spectrum, which allows the two regimes to be treated independently. This thesis focuses on atmospheric radiative processes in the longwave spectral region.

1.1 Longwave Radiative Characteristics of Atmospheric Gases

Absorption and emission of electromagnetic radiation by molecular systems occur during transitions from initial to final energy states. For the radiative energy exchange to occur a mechanism must be present which couples the electromagnetic field to the molecules. For the terrestrial spectrum the strongest coupling occurs via the electric dipole moments of the molecule. Some molecules, such as water vapor and ozone, have permanent electric dipoles due to the configuration of the atoms within the molecule; some molecules, such

as nitrogen and oxygen, do not have permanent dipole moments, but utilize temporary dipole moments induced by molecular collisions to radiatively transition. For a dipole transition to occur the dipole moment must not only be present but differ between the initial and final energy states.

Figure 1.1 shows a longwave, synthetic absorption spectrum for a middle latitude summer atmosphere. The simulated atmosphere contains eight important gases (water vapor [H_2O], carbon dioxide [CO_2], ozone [O_3], nitrous oxide [N_2O], carbon monoxide [CO], methane [CH_4], oxygen [O_2], nitrogen [N_2]), whose individual absorption features collectively form the complete absorption spectrum. An absorption band is defined as a cluster of individual absorption lines that appear continuous at coarse spectral resolution. The most important absorption bands in longwave atmospheric studies have been identified in Figure 1.1. Absorption bands are classified not only by molecule but by the magnitude of the internal energy change associated with the transitions. Electronic transitions involve the largest energy changes, corresponding to wavenumbers above 10,000 cm^{-1}; rotational and translational transitions (bands) involve the smallest energy changes between 1 to 500 cm^{-1}. Vibrational energy changes occupy the region between 500 and 10,000 cm^{-1}[1]. The most general transition simultaneously involves electronic, vibrational, and rotational transitions. For longwave radiative transfer it is the vibration-rotation bands that are relevant. It is important to note that emission is the inverse process of absorption. Radiative energy is created when the internal energy of a molecule spontaneously transitions from a higher to a lower state.

This section describes the spectroscopic properties of the gases which are significant contributors to the longwave energy budget and potential climate change. Also briefly reviewed is the general concentration of each of these gases within the atmosphere, since their absorption optical depths are a function of their spectroscopic properties and concentration.

The material for this section is derived from several sources: *Goody and Yung* [1989], *Liou* [1992], *Salby* [1996], *Clough et al.* [1992], and *Clough and Iacono* [1995].

[1]This thesis will generally use wavenumber ($\nu = 1/\lambda$) rather than wavelength (λ) as the spectral variable.

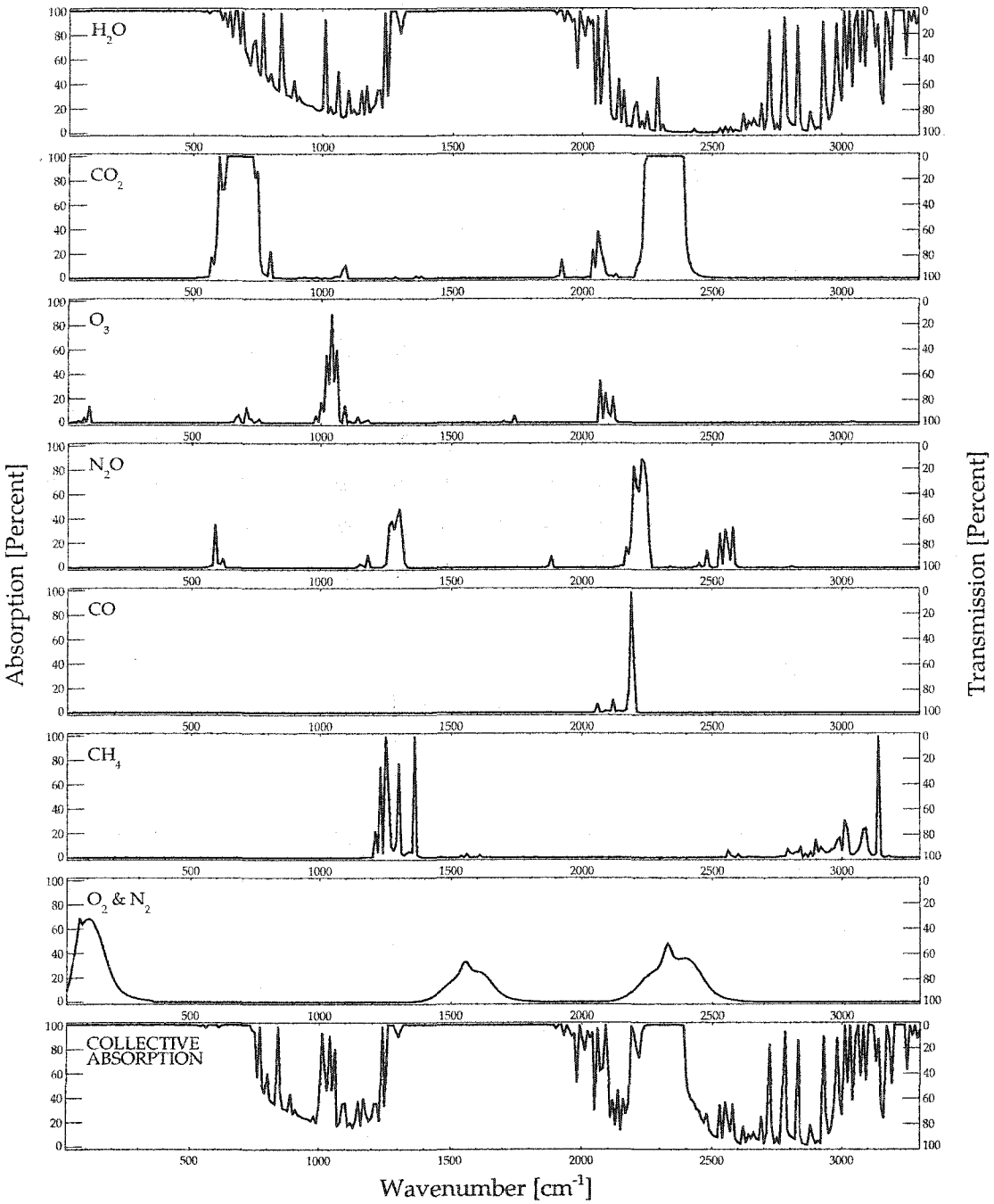

Figure 1.1. Longwave absorption spectra for a mid-latitude summer atmosphere. Individual and collective longwave absorption spectra of eight radiatively active gases within the mid-latitude summer atmosphere. Adapted from *Valley* [1965].

1.1.1 Water Vapor

The most influential radiative and dynamical trace species in the atmosphere is water vapor. The radiative impact of water vapor is a function both of its concentration and its spectroscopic properties. The absolute concentration of water vapor is highly variable both with geographic location and time, but it typically peaks at the surface and decreases significantly with altitude. Atmospheric water vapor is continually produced and destroyed in cloud dissipation/formation processes as well as through evaporation/condensation exchange with the oceans. As a consequence the vertical and horizontal distribution of water vapor in the atmosphere is highly variable.

Water vapor has significant absorption features throughout the entire longwave region. The important water vapor bands are distinctly classified as: the rotation band from 0 to 1000 cm^{-1}, the ν_2 band (or the 6.3 μm band) from 900 - 2400 cm^{-1}, and the combination of the ν_1 and ν_3 band (or the 2.7 μm band) from 2800 to 4400 cm^{-1}. The $\nu_{1,2,3}$ nomenclature refers to the three fundamental normal modes of vibration of a nonlinear, triatomic molecule, depicted in Figure 1.2.

In addition to the water vapor absorption bands noted above there is additional water vapor absorption that is smooth and continuous across the longwave spectral region. This continuous absorption, labeled the water vapor continuum, is defined as the absorption that must be added to the water vapor line-by-line absorption so that the total water vapor molecular absorption coefficient is consistent with spectral measurements. The continuum has two components: a self-broadened component (that is, water-water collisions), and a foreign-broadened component (that is, water-nitrogen-oxygen collisions). The self-broadened water vapor continuum dominates to the absorption in the atmospheric window[2], whereas the foreign-broadened continuum contributes most to the 50-300 and 1400-1800 cm^{-1} [*Clough et al.*, 1992]. The water vapor continuum will be further discussed in Section 2.2.3.

The combination of the absorption properties of the water vapor molecule and its relatively large tropospheric abundance make water vapor the most important gas in atmospheric radiation studies. The top panel of Figure 1.3 effectively displays the relationship

[2]Apart from a moderately strong ozone band from 980 - 1080 cm^{-1}, the absorption from 800 to 1200 cm^{-1} is relatively weak. This spectral region is known as the *atmospheric window*.

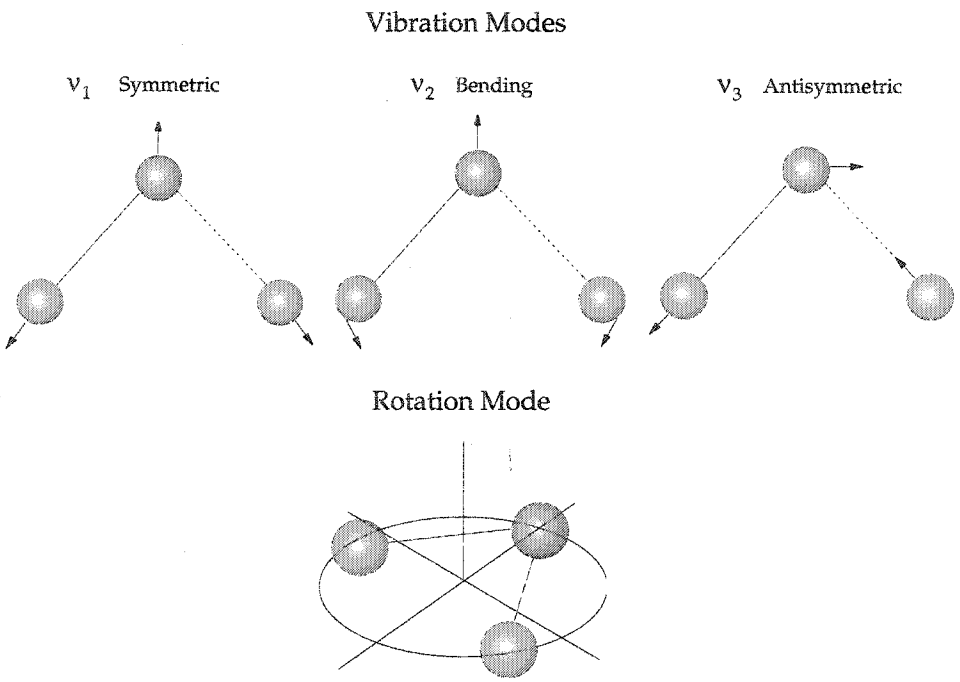

Figure 1.2. Water vapor molecule configuration. Vibrational modes and the axes of rotational freedom for the water vapor molecule, composed of two hydrogen atoms (red) and an oxygen atom (blue). Adapted from *Liou* [1992].

between the vertical distribution of water vapor, its spectral absorption properties, and longwave atmospheric cooling for the middle latitude summer climate. Since the spectral cooling rate is a function of the divergence of the net flux, the altitudes at which the atmosphere transitions from opaque to transparent correspond to the greatest cooling. In the spectral regions of strong absorption (10-400 and 1400-1800 cm^{-1}) the principal atmospheric cooling comes from the upper troposphere since the lower atmosphere is opaque. In the atmospheric window, the cooling is attributed principally to the water vapor self-continuum. The optical depth of the self-continuum has a quadratic dependence on water vapor abundance. Since the abundance drops dramatically with increasing altitude the transition from opaque to transparent occurs close to the surface. *Clough et al.* [1992] demonstrated that this picture of atmospheric cooling varies considerably with changes to the atmospheric temperature and water vapor profile.

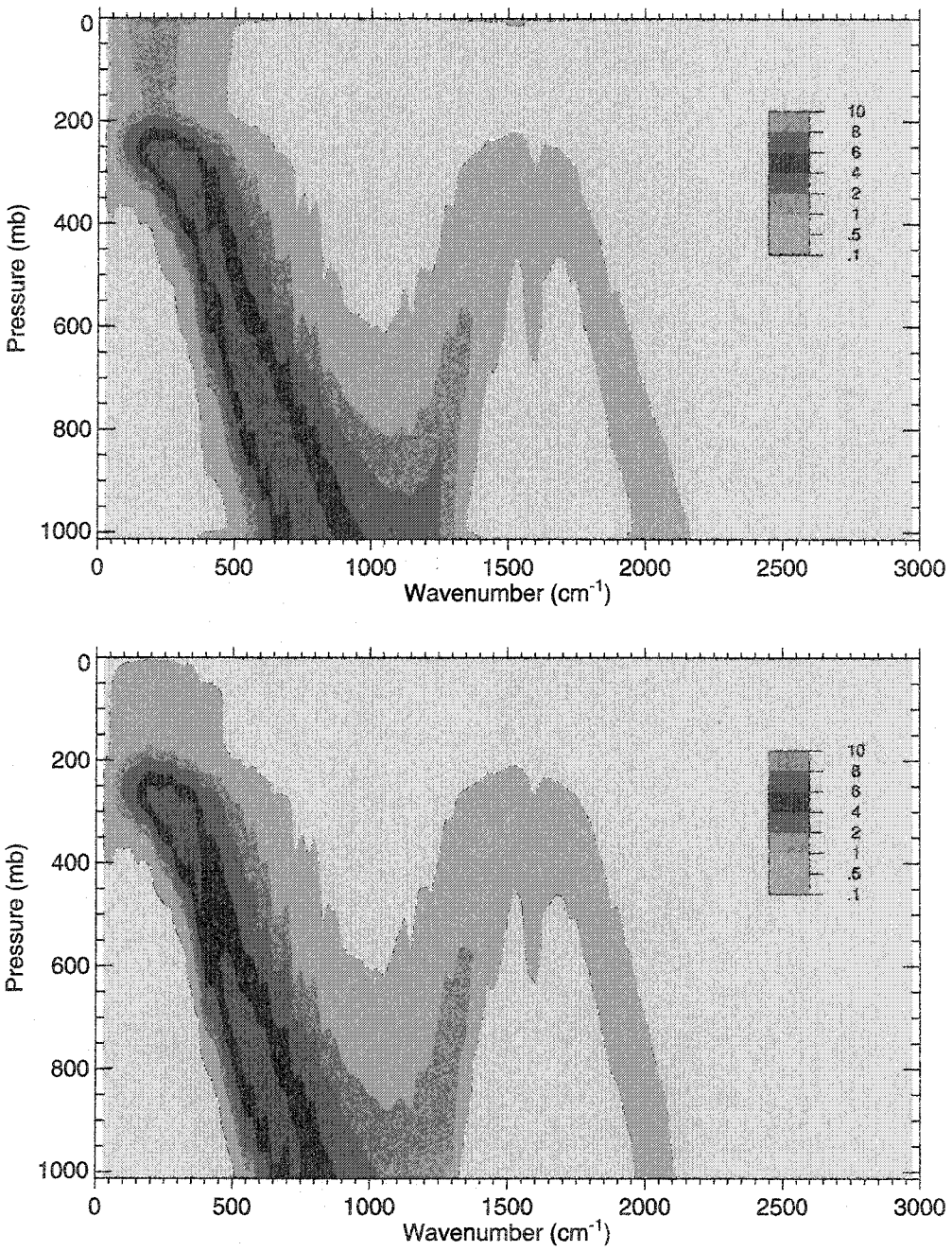

Figure 1.3. Contribution of water vapor to the atmospheric longwave radiation field. Top Panel: Spectral cooling rate profile for water vapor as a linear function of pressure for the ICRCCM mid-latitude summer atmosphere. Color scale x 10^{-3} is in units of K day^{-1} (cm^{-1})$^{-1}$. Bottom Panel: Contribution of atmospheric water vapor to the outgoing spectral radiance at the top of the atmosphere as a linear function of pressure. Color scale x 10^{-7} is in units of W (cm^2 sr cm^{-1})$^{-1}$. Figure and caption reproduced from *Clough et al.* [1992].

1.1.2 Carbon Dioxide

The carbon dioxide budget of the atmosphere depends on both human activities and natural biological and chemical processes. However, since the beginning of the industrial revolution the global concentration of carbon dioxide has increased roughly 30% to its current value of 360 ppmv. Carbon dioxide is an inert gas, well-mixed throughout the troposphere and stratosphere. Although the radiative effects of carbon dioxide occur in limited spectral regions, it is extremely influential in determining the surface temperatures (via the greenhouse effect). It also reduces the strength of the cooling rate associated with water vapor.

Carbon dioxide, like water vapor, is a triatomic molecule with three fundamental vibration modes, but its three atoms are linearly configured with the carbon atom in the center and the oxygen atoms on the outside. This configuration does not permit a purely rotational transition, but does allow vibrational-rotational transitions. The longwave spectrum of carbon dioxide is dominated by two strong bands: the ν_2 band, centered at 667 cm^{-1}, and ν_3 band, centered at 2349 cm^{-1}. There are also overtone and combination bands of carbon dioxide, produced by energy transitions between excited states, which result in relatively weak absorption in the atmospheric window.

1.1.3 Ozone

In the natural state of the atmosphere ozone is created and destroyed in the stratosphere in roughly equal amounts. Ozone, O_3, is created in a two-step process: (1) ultraviolet radiation, UV, is absorbed by molecular oxygen, O_2, which then dissociates into 2 oxygen atoms (2 O), then (2) the dissociated oxygen atoms can recombine with molecular oxygen to form ozone. UV radiation is also capable of destroying ozone through photodissociation. The closed system of natural ozone formation and destruction are described by two simple chemical reaction equations:

$$O + O_2 + M \Rightarrow O_3 + M \quad \text{(photolysis)} \tag{1.1}$$

$$O_3 + h\nu \Rightarrow O_2 + O \quad \text{(photodissociation)} \tag{1.2}$$

where $h\nu$ is the energy supplied by the UV radiation, and M represents any number of different atoms or compounds which carry away excess energy resulting from the combi-

nation of the O with the O_2. M does not change its own identity in this process. If there are sufficient number of M bodies present the oxygen atoms produced by the destruction of ozone will almost immediately recombine to form ozone.

Ozone is largely concentrated between 10 and 20 km, with the maximum total column abundance of ozone peaking at high latitudes. Most stratospheric ozone is produced in the tropics, but global dynamics transport it poleward. Smaller concentrations of ozone are also present in the troposphere. Tropospheric ozone comes from either penetration of the stratospheric ozone into the troposphere, or from chemical reactions involving hydrocarbons and nitrogen oxides, emitted by automobiles, refineries, and other industries. Since 1900 the amount of ozone near the earth's surface has more than doubled, but stratospheric ozone concentrations have decreased. Both of these changes are detrimental to human health as increasing tropospheric ozone can cause respiratory problems and decreasing stratospheric ozone increases exposure to harmful ultraviolet radiation.

Although ozone in radiative transfer processes is often associated with the shortwave spectral regime it also plays an important role in atmospheric cooling. Ozone is similar to water vapor in its atomic configuration. The ν_1 and ν_3 fundamental vibration modes combine to form a prominent ozone band (9.6 μm band) extending from 980 cm^{-1} to 1100 cm^{-1}. The ν_2 ozone band, centered at 705 cm^{-1}, has strong absorption properties, but it is usually masked by the even-stronger ν_2 carbon dioxide band. Finally a series of overtone and combination transitions produce a strong ozone band at 2105 cm^{-1}.

1.1.4 Methane, Nitrous Oxide, Carbon Monoxide, and Chlorofluorocarbons

Several other trace gases are also radiatively significant, particularly in context of climate change calculations. Methane and nitrous oxide are well mixed in the atmosphere and produced naturally, but anthropogenic sources are steadily rising to account for up to 20% of its total production. Carbon monoxide is primarily produced when carbonaceous materials are burned with insufficient oxygen; while there are natural sources of carbon monoxide, such as thunderstorms and forest fires, two thirds of current carbon monoxide emissions are produced by transportation sources. Chlorofluorocarbons (CFCs), such as CCl_4 and $CFCl_3$, are produced completely by human industrial activities. CFCs are long-lived and thus well mixed in the troposphere, and are transported to the stratosphere via

the meridional circulation. While CFCs are radiatively important in their own right, they also impact longwave radiative transfer through their participation in the destruction of stratospheric ozone.

Of these molecules carbon monoxide has the simplest atomic configuration and absorption spectrum. While carbon monoxide does have a weak rotation band, it is the fundamental band of the principal isotope (centered at 2143.27 cm^{-1}) which must be considered in radiative transfer calculations. Methane and nitrous oxide are more complex molecules, and have numerous rotational, fundamental, overtone, and combination bands that are active in the longwave spectral region. For methane the most important band climatically extends 1190 to 1380 cm^{-1}, while nitrous oxide is important between 550 and 620 cm^{-1} and between 1130 and 1320 cm^{-1}. CFC absorption occurs primarily in the atmospheric window. Although the contribution of these molecules to the total atmospheric longwave cooling is secondary, their presence in the atmospheric window make them important contributors to climate change.

1.1.5 Nitrogen and Oxygen

Nitrogen and oxygen comprise approximately 79% and 20%, respectively, of the molecules in the atmosphere. Their mixing ratios are constant through out the lowest 90 km of the atmosphere, and are not expected to change significantly due to human activities.

Due to the symmetrical configuration of these diatomic molecules electric dipole moments are not present in either their ground or excited state. However, collision-induced transitions do occur and must be accounted for due to the large amount of these gases present in the atmosphere. For nitrogen two collision-induced bands are climatically significant: the rotation band from 10 to 350 cm^{-1}, and the fundamental band from 2100 to 2600 cm^{-1}. For oxygen a rotational, fundamental, and overtone band have been observed, but it is the fundamental band from 1400 to 1800 cm^{-1} which is significant in atmospheric radiative transfer.

1.2 Longwave Radiative Transfer in Atmospheric Models

Radiative processes create regions of heating and cooling in the atmosphere which directly affect the dynamics and thermodynamics of earth's atmosphere. The accuracy of weather forecasts and prediction of climate change is, in part, determined by the accuracy of the radiative transfer calculations within the forecast and climate models. In the longwave spectral region, the complex line structures of the numerous radiatively active gases make radiative transfer calculations particularly demanding. Line-by-line models compute radiative quantities with fine spectral resolution and, therefore, are highly accurate but computationally expensive. As an alternative to this class of calculations band models have been developed which divide the spectrum into wide spectral regions and capture the salient features of the absorption spectrum within that region. The spectral intervals of the band models are often dictated by the important absorption features noted in Section 1.1

Analyzing the performance of band models has been the focus of many recent programs and research efforts. The Intercomparison of Radiation Codes in Climate Models (ICRCCM), a large program co-sponsored by several international agencies, analyzed clear-sky longwave flux and cooling rate calculations submitted by more than 35 research groups. Line-by-line model results were in general agreement to within 1%; band model quantities varied largely with a 5 to 10% rms difference with the line-by-line results, and exhibited even larger disagreement when important trace gases were perturbed from the standard atmosphere calculation [*Ellingson et al.*, 1991]. Similar intermodel variability has been found in other studies, such as the Atmospheric Model Intercomparison Project (AMIP) [*Duvel et al.*, 1997; *Cess and et al.*, 1997].

While comparisons of rapid band models against line-by-line measurements are vital, line-by-line models themselves are not approximation-free. Therefore, it is necessary to also assess the model performance against atmospheric radiation measurements. It is a difficult task to analyze model calculations against observations since a number of factors must be examined, including a) the input data required for radiative transfer calculations (atmospheric temperature, humidity), which may not accurately describe the atmospheric state, and b) the uncertainties in the radiance and flux measurements themselves.

The U.S. Department of Energy's Atmospheric Radiation Measurement (ARM) Program was established, in part, to provide high-quality, comprehensive measurements of the atmospheric state and atmospheric radiation from which radiative transfer models could be developed and validated. Of interest to this thesis is the ARM-supported effort to a) develop and validate the line-by-line radiative transfer model LBLRTM [*Clough et al.*, 1992; *Clough and Iacono*, 1995], and b) to build rapid radiation models which reproduce the results of LBLRTM within the constraints of increased computational efficiency. Such rapid radiation models can ultimately be used in both general circulation models and global climate models (GCMs) and for simulations of satellite radiances.

1.2.1 The Line-By-Line Radiative Transfer Model: LBLRTM

LBLRTM calculates spectral transmittances, radiances, and fluxes with high accuracy at monochromatic resolution. LBLRTM obtains such accuracy by utilizing: 1) at all altitudes the Voigt line shape and a detailed line parameter database to calculate the contribution of individual spectral lines to the absorption coefficient, 2) a complete water vapor, carbon dioxide, oxygen and nitrogen continuum model ([*Clough et al.*, 1989; *Thibault et al.*, 1997; *Mlawer et al.*, 1998; *Borysow and Frommhold*, 1986; *Lafferty et al.*, 1996]), and 3) an algorithm to treat the variation of the Planck function within a vertically inhomogeneous layer.

LBLRTM has been extensively validated against both surface-based and air-borne spectral radiance measurements [*Walden et al.*, 1998; *Tobin et al.*, 1999; *Clough et al.*, 2000]. Of particular significance have been the validations against a large dataset of high-resolution spectral measurements of downward surface radiance from the University of Wisconsin's Atmospheric Emitted Radiance Interferometer (AERI) [*Revercomb et al.*, 1996], located at the ARM Southern Great Plains Cloud and Radiation Testbed (SGP CART) site. LBLRTM and AERI typically agree to within 3 W m^{-2} for a variety of atmospheric conditions at the SGP CART site [*Clough et al.*, 2000]. It is important to note that this difference includes uncertainties in the model calculations due to inaccurate specification of the atmospheric state.

The Continuum Model

Water vapor continuum absorption and emission critically impacts the earth's climate by contributing as much as 40% to the total, near-surface longwave cooling rate and decreasing the outgoing longwave flux by more than 10 W m−2 for moist atmospheres.

The physical processes which result in the water vapor continuum absorption has been the subject of many scientific debates. A number of theories concerning the continuum absorption have been put forth, including that the absorption is due to water vapor dimers or multimers. A key development in the water vapor continuum debate was the introduction of the CKD model by Clough, Kneizys, and Davies [*Clough et al.*, 1980, 1989]. To account for the deviations between the observed absorption and the absorption calculated using the standard Lorentz line shape shape, a semi-empirical line shape formalism for the water vapor monomer was derived from laboratory measurements and applied to all water vapor spectral lines. This model demonstrated the continuum absorption could be explained by the interaction of a single water vapor molecule (monomer) with another water vapor molecule (self-continuum) or a different molecule (foreign-continuum).

The philosophy of the data-determined water vapor continuum has led to several revisions which incorporate recent high-resolution spectral radiance observations from field campaigns and laboratory measurements. These revisions have led to the current continuum model release, CKD 2.4.

In addition to the water vapor continuum, CKD 2.4 contains models of the continua of other gases, including nitrogen, oxygen, and carbon dioxide.

1.2.2 The Rapid Radiative Transfer Model: RRTM

To address the ARM program objective of improving radiation models in GCMs a rapid radiation model (RRTM) was created to obtain fluxes and cooling rates with an accuracy consistent with LBLRTM but with much greater computational speed [*Mlawer et al.*, 1997]. RRTM divides the longwave spectrum into 16 bands, and employs the efficient correlated-k method of radiative transfer (refer to Chapter 2 for a detailed description of the method). LBLRTM provides the absorption coefficients from which the k distributions in RRTM are calculated, as well as serving as a validation tool for RRTM. This utilization of LBLRTM

provides a link from RRTM to high-resolution spectral measurements. For a set of six standard clear-sky atmospheres the 1998 release of RRTM (version 2.3) compared with the 1996-1997 version of LBLRTM as follows: 0.6 W m^{-2} for net flux in each band at all altitudes relative to LBLRTM, with a broadband difference of less than 1.0 W m^{-2} at any altitude; 0.1 K day^{-1} for total cooling rate difference in the troposphere and lower stratosphere, and 0.75 K day^{-1} in the upper stratosphere and above.

RRTM also computes radiative quantities in the presence of clouds. Cloud optical properties are parameterized as a function of cloud droplet size and cloud water content [*Hu and Stamnes*, 1993], and random and maximum/random cloud overlap schemes are available. Cloudy-sky radiative transfer is not a topic in this thesis, but the cloudy-sky capability is a vital component of climate model calculations. RRTM and LBLRTM do not include the process of multiple scattering in their solutions to the radiative transfer equation. Scattering is an important process, but is typically ignored in rapid longwave radiative transfer calculations.

The potential role of RRTM in improving climate model calculations has been the topic of several studies. *Iacono et al.* [2000] assessed the impact of employing RRTM in a simulated climate system by incorporating it into the National Center for Atmospheric Research Community Climate Model, CCM3 [*Kiehl et al.*, 1998]. CCM3 was selected because it is widely used and highly regarded by the climate community. The results of the *Iacono et al.* [2000] study showed the use of RRTM in CCM3 significantly impacted the global radiative energy budget by a) reducing the outgoing longwave radiation by 6-12 W m^{-2} at tropical latitudes, and b) increasing the downward surface radiation by 8-15 W m^{-2} at polar latitudes. This enhancement of longwave absorption, relative to the standard CCM3 radiation model, was largely due to the inclusion of a modern and more spectrally extensive water vapor continuum model in RRTM.

Modifying the longwave fluxes results in a modified dynamic and thermodynamic structure of the atmosphere. In the RRTM-CCM3 simulations the lower tropospheric and surface temperatures increased as a result of increased downward flux. The introduction of RRTM into the *Iacono et al.* [2000] CCM3 climate simulations considerably reduced the known flux biases in CCM3, and potentially would have the same impact in other GCMs.

RRTM can also be used to improve weather forecasting models. RRTM[3] was integrated into the European Center for Medium-Range Weather Forecasts (ECMWF) operational model in June 2000[*Morcrette et al.*, 2001]. Prior to June 2000 the ECMWF longwave radiation scheme utilized just six spectral bands, whereas RRTM utilizes 16 spectral bands. More spectral bands will better capture the spectral signatures of surface and cloud properties. The implementation of RRTM in the ECMWF model corrects the major underestimation of clear-sky downward longwave radiation [*Morcrette*, 2002], which is consistent with the *Iacono et al.* [2000] study. The stratospheric temperatures and cooling rates also respond significantly to the improved treatment of radiation, ultimately altering high-level cloudiness. This radiative adjustment of stratospheric temperature is likely due to the proper treatment of upper-altitude line shapes, which are a factor in the calculation of absorption coefficients [*Morcrette et al.*, 2001].

1.3 Thesis Content and Organization

This thesis addresses longwave radiative transfer in the Earth's atmosphere from a variety of perspectives. Foremost is the continued improvement of rapid radiative transfer models with the goal of calculating radiative quantities that are consistent with the highly-validated line-by-line radiative transfer model LBLRTM. A Flexible Radiative Transfer Tool (FLRTT) has been developed which facilitates the creation of rapid radiative transfer models for user-specified spectral intervals. This is extensively described in Chapter 2. Two applications of FLRTT-generated models are detailed in Chapter 3 and Chapter 4.

Chapter 3 details a recent evaluation of upper tropospheric water vapor simulated in the National Center for Atmospheric Research Community Climate Model, CCM3, using modeled and observed High-resolution Infrared Radiation Sounder (HIRS) observations [*Iacono et al.*, 2003]. The model used for this evaluation was constructed using FLRTT, and therefore has close ties to the highly-accurate line-by-line radiation transfer model LBLRTM. By removing the uncertainties associated with less-accurate default radiative transfer model in CCM3, dynamical processes in the GCM can be more effectively evalu-

[3]Various changes were made to the general release of RRTM to adapt it to the ECMWF environment. These are described in *Morcrette et al.* [2001]

ated.

Chapter 4 describes the extensive update of the rapid radiation model RRTM from version 2.3 to version 3.0. RRTM v2.3 compared very well against the version of LBLRTM from which it was generated. However, there have been a number of spectroscopic changes in LBLRTM since 1998, thereby requiring that RRTM v2.3 be updated to reflect these changes as well. Other notable changes between RRTM v2.3 and RRTM v3.0 are improved stratospheric cooling rates, as well as improved flux and cooling rates for atmospheres with trace gas abundances substantially different from modern-day atmospheres.

Chapter 5 examines radiative transfer calculations of radiance and flux, respectively, from LBLRTM and RRTM v3.0 in the context of measurements. The AERI/LBLRTM Quality Measurement Experiment and the Broadband Quality Measurement Experiments (QMEs) at the ARM SGP CART site have extensively compared clear-sky longwave radiometric observations with model calculations from LBLRTM and RRTM. These QMEs have been critical in the identification of a number of issues, such as a dry bias in the radiosonde relative humidity measurements, as well as instrument calibration issues. A suite of instruments similar to that at the ARM SGP CART site is also operational at the ARM North Slope of Alaska Cloud and Radiation Testbed (NSA CART) site, but such QMEs have not been performed on the NSA CART site data. A number of clear sky time periods from the 2001 annual cycle have been utilized to simultaneously address the specification of the atmospheric state, longwave radiometric measurements, and radiative transfer at the NSA CART site. Results from this intercomparison are presented in Chapter 5.

Chapter 2

Generation and Operation of Rapid Longwave Radiative Transfer Models

Accurately quantifying molecular absorption and emission in the Earth's atmosphere is critical in solving numerous problems in atmospheric science, ranging from numerical weather prediction to interpreting measured satellite radiances. In the longwave spectral region, the complex line structures of the numerous radiatively active gases make radiative transfer calculations particularly demanding. Line-by-line models are used to compute radiative quantities with fine spectral resolution and, therefore, are highly accurate but computationally expensive. A number of numerical strategies have been developed to reduce computational expense but maintain accuracy in radiative transfer calculations. The correlated-k distribution is a popular method used to obtain this goal [*Goody et al.*, 1989; *Lacis and Oinas*, 1991; *Fu and Liou*, 1992; *Mlawer et al.*, 1997]. It is an efficient procedure that substantially reduces the number of calculations within a spectral interval compared to a line-by-line model without compromising accuracy. It is also conducive to calculations in inhomogenous atmospheres in which multiple scattering due to clouds and aerosols is present.

Although the theory behind the correlated-k distribution is well established, a substantial effort is often required to implement the method for specific applications. This chapter introduces a FLexible Radiative Transfer Tool (FLRTT), which facilitates the construction of correlated-k radiative transfer models. FLRTT creates k distributions from absorption

coefficients provided by the line-by-line radiative transfer model LBLRTM. One advantage of FLRTT is the flexibility it offers to users to choose not only the spectral bandwidth but also the absorbing species to be included. To accompany the k distributions FLRTT also constructs a module to calculate absorption optical depths from the k distributions. The k distributions and the routine to calculate absorption optical depths are modular in structure. The optical depths calculated from the k distributions can be employed by any algorithm which solves the radiative transfer equation, including those which account for multiple-scattering[1].

FLRTT provides the option to the user to combine the k distributions and optical depth routine it has generated with the radiative transfer routine employed by LBLRTM, thereby providing a complete radiative transfer code (hereafter referred to as a FLRTT-Generated Model (FGM)). FLRTT is typically run to produce either a radiance and brightness temperature model, or flux and cooling rate model. For computing radiative quantities for comparison to measurements, FLRTT has the capability to include instrument response functions. Finally, FLRTT has an automated validation scheme which compares radiances and brightness temperatures, or fluxes and cooling rates calculated by the newly generated FGM with those calculated by LBLRTM for a variety of atmospheres.

The modular design of FLRTT permits easy updates of the k distributions when improvements have been made to spectroscopic databases, the continuum, or the line-by-line model.

2.1 General Radiative Transfer Theory

As a beam of radiation passes through a medium its intensity[2], $I(\nu)$, at wavenumber ν is reduced through either absorption or scattering by molecules and particles in the medium[3]. The magnitude of this extinction varies linearly with both the incident intensity and the amount of optically active matter along the beam's path length ds. This relationship,

[1]Special care must be given to the treatment of the Planck function and any scattering properties when utilizing the correlated-k method in the longwave spectral region. This will be discussed in detail in Sections 2.3.

[2]Radiance is another common term for intensity.

[3]The material for this section is derived from three books: *Thomas and Stamnes* [1999], *Liou* [1992] and *Salby* [1996].

known as the *Extinction Law* or *Beer's Law*, is written as:

$$dI(\nu) = -I(\nu)\beta(\nu)ds \quad [\mathrm{W \cdot m^{-2} \cdot sr \cdot (cm^{-1})^{-1}}]. \tag{2.1}$$

where the constant of proportionality, $\beta(\nu)$, is called the extinction coefficient. There are three perspectives from which to view extinction: in terms of the path length ds, the mass path $du = \rho ds$, and the column abundance $dW = nds$ where ρ and n are the mass density [kg $\cdot$ m^{-3}] and the particle density [m^{-3}]. This leads to three formal definitions of extinction:

$$\beta(\nu) \equiv -\frac{dI(\nu)}{I(\nu)ds} \text{ extinction coefficient } [\mathrm{m^{-1}}] \tag{2.2}$$

$$\beta_m(\nu) \equiv -\frac{dI(\nu)}{I(\nu)du} \text{ mass extinction coefficient } [\mathrm{m^2 \cdot kg^{-1}}] \tag{2.3}$$

$$\beta_n(\nu) \equiv -\frac{dI(\nu)}{I(\nu)dW} \text{ extinction cross section } [\mathrm{m^2}]. \tag{2.4}$$

Analagous coefficients exist for both the absorption, $k(\nu)$, and scattering processes, $\sigma(\nu)$, whose sum is the total extinction.

A beam can also gain radiative energy from emission by the optically active particles in the medium. This process is formally described by an emission coefficient $j(\nu)$ [W $\cdot$ m^{-3} $\cdot$ sr^{-1} $\cdot$ (cm^{-1})$^{-1}$]. Combining the Extinction Law with the definition of emission, the total change in a beam's radiative energy as it passes through a medium is given by

$$dI(\nu) = -\beta(\nu)I(\nu)ds + j(\nu)ds. \tag{2.5}$$

Defining $\beta(\nu)\, ds$ as the differential slant optical path, $d\tau_s(\nu)$, Equation 2.5 can be expressed as

$$\frac{dI(\nu)}{d\tau_s(\nu)} = -I(\nu) + S(\nu) \tag{2.6}$$

where $S(\nu)$, the ratio of the emission to extinction coefficient, is termed the source function.

This thesis addresses clear-sky longwave radiative transfer in which several assumptions are made to simplify the solution to Equation 2.6: (1) the atmosphere is in thermodynamic equilibrium, and (2) scattering processes can be ignored (that is, the extinction coefficient, $\beta(\nu)$, is replaced by the absorption coefficient, $k(\nu)$). In accordance with assumption (1) Planck's Law can be used to quantify the emission from the medium. Planck's Law relates the intensity emitted by the population of molecules in the medium to their absolute

temperature:

$$S(\nu) = B(\nu,\Theta) = \frac{2h\nu^3c^2}{exp(hc\nu/k_B\Theta)-1} \tag{2.7}$$

where h is Planck's constant, k_B is Boltzmann's constant, and c is the velocity of light, and Θ is the absolute temperature. In the absence of scattering processes the source function is simply the Planck function.

An additional assumption is commonly made about the geometry of the medium. Since a planetary atmosphere is predominately stratified in the vertical direction due to the force of gravity, horizontal variability in the medium can be ignored. Plane-parallel geometry can, therefore, be employed. For convenience in radiative transfer analyses it is common to write the radiative transfer equation for both the upward intensity, $I^+(\nu,\tau_s,\theta \leq \pi/2)$, and downward intensity, $I^-(\nu,\tau_s,\theta > \pi/2)$. Equation 2.6 can be rewritten as

$$\mu\frac{dI^+(\nu,\tau,\mu)}{d\tau(\nu)} = I^+(\nu,\tau,\mu) - B(\nu,\tau) \tag{2.8}$$

$$-\mu\frac{dI^-(\nu,\tau,\mu)}{d\tau(\nu)} = I^-(\nu,\tau,\mu) - B(\nu,\tau) \tag{2.9}$$

where μ is the absolute value of the cosine of the zenith angle, $S(\nu) = B(\nu)$, and $B(\nu)$ is a function of the temperature at level τ. This geometry is illustrated in Figure 2.1. Note that the slant optical path, τ_s, has been replaced by the vertical optical path τ (or *optical depth*), using the relationship

$$d\tau(\nu,z) = -d\tau_s(\nu)\mu \tag{2.10}$$

$$= -k(\nu)\mu dz. \tag{2.11}$$

With the use of an integrating factor the radiative transfer equation can easily be solved. For the upward intensity the integration is performed from the bottom ($\tau = \tau^*$) to the top of the medium ($\tau = 0$) and vice-versa for the downward intensity. For a given wavenumber, the half-range solutions to the radiative transfer equation, with the assumptions outlined above, are:

$$I^+(\tau,\mu) = I^+(\tau^*,\mu)e^{-(\tau^*-\tau)/\mu} + \int_\tau^{\tau^*}\frac{d\tau'}{\mu}e^{-(\tau'-\tau)/\mu}B(\tau') \tag{2.12}$$

$$I^-(\tau,\mu) = I(0,\mu)e^{-\tau/\mu} + \int_0^{\tau}\frac{d\tau'}{\mu}e^{-(\tau-\tau')/\mu}B(\tau'). \tag{2.13}$$

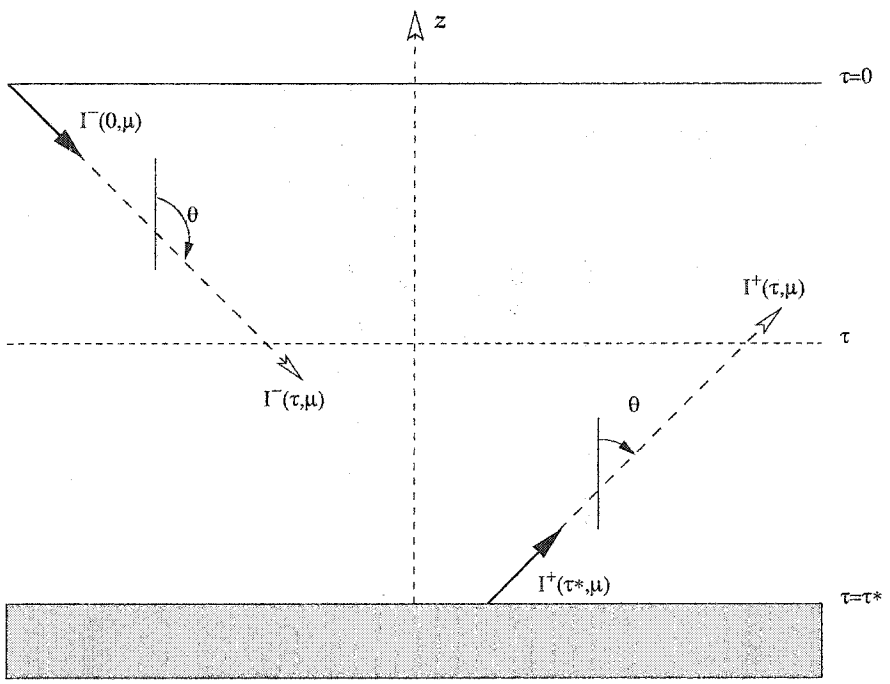

Figure 2.1. Half-range intensities in a slab geometry. The optical depth variable is measured from the top of the medium (τ=0) to the bottom (τ=τ^*). μ equals the absolute value of the cosine of the polar angle θ.

To use this equation practically an assumption must be made about the vertical variation of the Planck function across an atmospheric layer. It is common to assume that the Planck function varies linearly with optical depth from the value at the upper boundary B_U to that at the lower boundary B_L with slope $[(B_U - B_L)/\tau]$ [*Wiscombe*, 1976; *Ridgway et al.*, 1991; *Clough et al.*, 1992]. Consider the simple case of intensity exiting normal to a single homogeneous layer [that is τ=0, μ=1 in Equation 2.13],

$$I^+(0) = I^+(\tau^*)e^{-\tau^*} + \int_0^{\tau^*} d\tau' e^{-\tau'} B(\tau'). \tag{2.14}$$

where the spectral dependence has again been suppressed. With this "linear-in-τ" assumption Equation 2.14 can be rewritten as

$$I^+(0) = I^+(\tau^*)e^{-\tau^*} + \int_0^{\tau^*} d\tau' e^{-\tau'} \left[B_U + \left(\frac{2(\overline{B} - B_U)}{\tau^*} \right) \tau' \right] \tag{2.15}$$

where $\overline{B}$ is interpreted as the mean Planck function for the layer ($\frac{B_U + B_L}{2}$). The solution to Equation 2.14 is then expressed as

$$\begin{aligned} I^+(0) &= I^+(\tau^*)T + (1-T)\left[B_U + 2(\overline{B} - B_U)\left(\frac{1}{\tau^*} - \frac{T}{1-T} \right) \right] && (2.16) \\ &= B_{eff}(\tau^*) + \left[I^+(\tau^*) - B_{eff}(\tau^*) \right] T && (2.17) \end{aligned}$$

where T is the layer transmittance, $e^{-\tau^*}$, and the quantity in brackets in the upper equation is labeled the layer effective Planck function $B_{eff}(\tau^*)$. $B_{eff}(\tau^*)$ varies from $\overline{B}$ in the optically thin regime to B_U in the optically thick regime. Note that this approximation implies that the optical depth varies linearly across the layer and that the absorption coefficient is constant in the layer.

The hemispheric fluxes are obtained by integrating the directional intensities as follows

$$F^{\pm}(\tau) = 2\pi \int_0^1 I^{\pm}(\tau, \mu)\mu d\mu. \tag{2.18}$$

Finally, the radiative cooling rate, or the change in temperature of a parcel of air per unit time, is proportional to the divergence of the net flux, and is given by

$$\frac{\partial \Theta}{\partial t} = -\frac{1}{c_p \rho} \frac{dF}{dz} \tag{2.19}$$

where c_p is the specific heat at constant pressure and ρ is the density of the medium.

The accuracy of intensity, flux, and cooling rate calculations in the absence of scattering at a given wavenumber is dictated, in part, by the extent to which the optical properties of the medium are known. The optical properties of a non-scattering medium are embodied in the absorption coefficient. The absorption coefficient of a single absorbing species due to a single line at wavenumber ν is the product of its line strength and a line shape factor, which accounts for line broadening. When multiple lines and species are present the absorption coefficient is the collective contribution from each line of each species. There are two important line-broadening mechanisms in atmospheric applications: collisional broadening (Lorentz line shape) dominates in the lower atmosphere and velocity broadening (Doppler line shape) dominates in the upper atmosphere. These two sources of line broadening are treated jointly in the Voigt line shape. The Voigt half width for water vapor at 1000 cm^{-1}, assuming the midlatitude summer temperature profile, ranges from roughly 0.1 cm^{-1} at the surface to 0.001 cm^{-1} at the top of the atmosphere; at 10 cm^{-1} it ranges from 0.1 to 0.00001 cm^{-1}. The line-by-line method of radiative transfer is currently the most accurate method with which to calculate absorption coefficients because it adequately samples even the narrowest lines. As an example the line-by-line model LBLRTM samples four points per mean half width. To calculate the optical depth at the top of the atmosphere for the longwave region from 10 to 3000 cm^{-1} requires roughly 10^7 calculations at this sampling interval [*Clough et al.*, 1992].

Calculating spectrally integrated radiative quantities at the fine spectral resolution of the line-by-line method becomes computationally expensive. Band models, which capture the general features of the absorption spectrum, are often utilized for their computational efficiency. One particular method, the correlated-k method, reduces the number of calculations required to obtain the radiative quantities of a spectral band by orders of magnitude while maintaining an accuracy comparable to line-by-line models. This is accomplished by using a small set of characteristic absorption coefficients to represent the true spectrum of absorption coefficients. Consider the simple case of a single homogeneous layer of thickness, z, and transmittance $T(\nu) = e^{-\tau^*} = e^{-k(\nu)z}$. The spectrally averaged intensity exiting normal to the layer is described by

$$I^+(\bar{\nu})(0) = \frac{1}{\nu_2 - \nu_1} \int_{\nu_1}^{\nu_2} d\nu \left[B_{eff}(\nu, \tau^*) + (I^+(\nu, \tau^*) - B_{eff}(\nu, \tau^*)) e^{-k(\nu)z} \right] \tag{2.20}$$

where ν_1 and ν_2 are the starting and ending wavenumbers of the spectral interval. The absorption coefficient, equal to the extinction coefficient for a non-scattering atmosphere, is assumed not to vary across the layer. The correlated-k method reduces the number of calculations compared to the line-by-line method in two steps. Since the evaluation of the integral over wavenumber is independent of the ordering of $k(\nu)$, the rapidly varying absorption coefficient function is transformed into a smoothly varying, monotonic function. This is accomplished by ranking line-by-line calculated absorption coefficients, $k(\nu)$, by increasing strength, expressing the absorption coefficient strength distribution as a cumulative probability distribution, $g(k)$, and finally inverting the cumulative probability distribution to $k(g)$. The inverted cumulative frequency distribution is known as a k distribution[4]. This process is hereafter referred to as mapping $k(\nu)$ to $k(g)$ ($\nu \rightarrow g$) [*West et al.*, 1990], and is illustrated in Figure 2.2 for the important ozone band from 980 - 1080 cm^{-1}. Equation 2.20 is now expressed as

$$I^+(\bar{\nu})(0) = \int_0^1 dg \left[B_{eff}(g,\tau^*) + [I^+(g,\tau^*) - B_{eff}(g,\tau^*)]e^{-k(g)z} \right] \tag{2.21}$$

where all variables with a dependence on wavenumber have been transformed to g via the $\nu \rightarrow g$ mapping.

The second step is to approximate the integral in the preceeding equation by dividing the function into a small set of subintervals j, each corresponding to a subset of the $k(g)$ values, and averaging the $k(g)$ and $B_{eff}(g)$ within each interval to obtain a single characteristic absorption coefficient, κ_j, and effective Planck function, $B_{eff,j}$ for that interval. For each subinterval the intensity, I_j^+, is computed using a single characteristic absorption coefficient. The final solution to equation 2.14 is given by

$$I(\bar{\nu})^+(0) \approx \sum_j \mathcal{W}_j \left[B_{eff,j}(\tau^*) + [I_j^+(\tau^*) - B_{eff,j}(\tau^*)]e^{-\kappa_j z} \right] \tag{2.22}$$

where $\mathcal{W}_j$ is the weight of each subinterval ($\sum_j \mathcal{W}_j = 1$). Radiative transfer operations are performed on each subinterval, just as they would otherwise be performed in wavenumber space in a monochromatic model. The only error introduced for a subinterval in this procedure is the replacement of the $k(\nu)$, $B_{eff}(\nu)$, and $I^+(\nu)$ with single characteristic values of κ_j, I_j^+, and $B_{eff,j}$.

[4]For a complete description of this process, see *Lacis and Oinas* [1991]

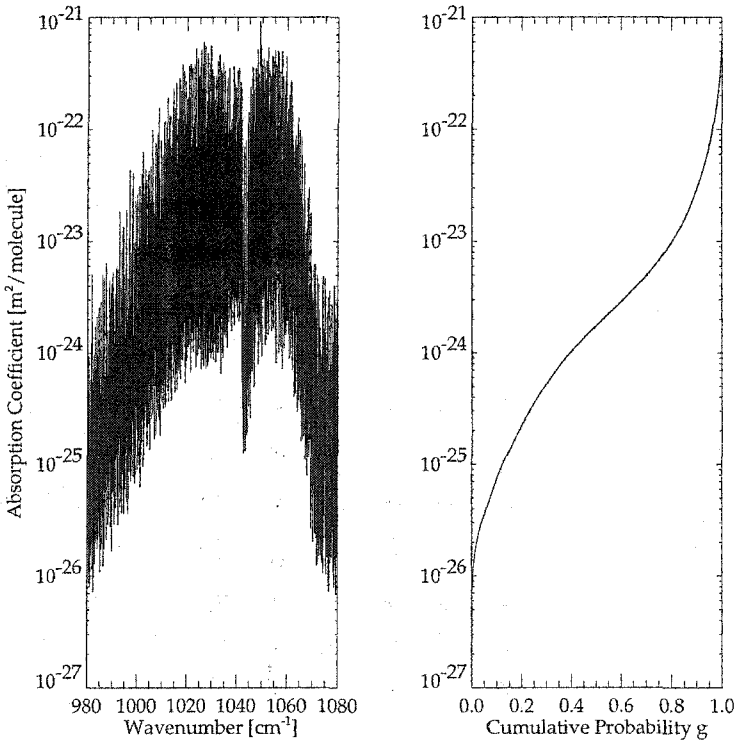

Figure 2.2. Mapping transformation of absorption coefficients for ozone band. Absorption coefficients for the 980-1080 cm^{-1} ozone band in the upper atmosphere of a midlatitude summer atmosphere as a function of wavenumber (left panel) and cumulative probability distribution (right panel).

The k distribution method can be extended to model realistic atmospheres in which temperature, pressure, and absorbing-species gradients exist. This is accomplished by dividing the atmosphere into layers and applying the k distribution method, described above, to each layer. The intensity exiting a layer at a given value of g enters the adjacent layer at the same g value. This is equivalent to the treatment of intensity at a given spectral point in monochromatic radiative transfer calculations. The accuracy of this method depends on to what extent the mapping of $\nu \rightarrow g$ is *correlated* between successive atmospheric layers. In the case of a single absorption line the correlation is exact since the strongest absorption occurs at the same frequency for all pressure levels and the weakest absorption occurs at frequencies in the line wings [*Lacis and Oinas*, 1991]. This is also true for lines that are periodically spaced and, to a large extent, in the limit of strong and weak absorption

[*Lacis and Oinas*, 1991; *Fu and Liou*, 1992]. Under real atmospheric conditions the degree of correlation between k distributions in a given spectral interval depends on the temperature, pressure and molecular concentration profiles between radiatively interacting layers. Judicious choice of band boundaries can mitigate possible correlation errors.

As an alternative to allowing the mapping to vary from one layer to the next, a fixed mapping for a spectral interval could be applied to all layers. This forces correlation between layers but does not necessarily produce monotonically increasing k distributions in each layer. Therefore, the range of magnitudes of the absorption coefficients in each subinterval could vary substantially, and the use of a single characteristic κ_j for each subinterval may then result in errors that exceed those incurred by use of the correlated-k method.

2.2 Development and Properties of a FLRTT-Generated Radiative Transfer Model

Numerous correlated-k models have been developed in the last decade. These models are used not only for climate applications but also for the simulation of space-based and ground-based radiometric observations. One example of such a model is the rapid radiative transfer model RRTM [*Mlawer et al.*, 1997]. RRTM calculates longwave fluxes and cooling rates using the correlated-k method. RRTM's accurate results combined with its rapid execution have made it a popular model both as a general radiative transfer tool and as a radiative transfer routine for numerical weather prediction and climate models [*Pinto et al.*, 1997; *Morcrette et al.*, 2001; *Dudhia et al.*, 2002].

RRTM was developed with a series of tools that facilitated the calculation of k distributions and the subsequent characteristic absorption coefficients κ_j. However, for each spectral band, the tools would have to be adjusted to account for different absorbing species and other band subtleties. These tools have now been compiled, improved, and expanded into the FLexible Radiative Transfer Tool (FLRTT). FLRTT is a comprehensive package which allows the easy generation of a correlated-k model that will output either radiances and brightness temperatures or fluxes and cooling rates for any spectral interval in the longwave (10 - 3250 cm^{-1}).

The primary tasks of FLRTT are to execute LBLRTM to obtain absorption coefficients

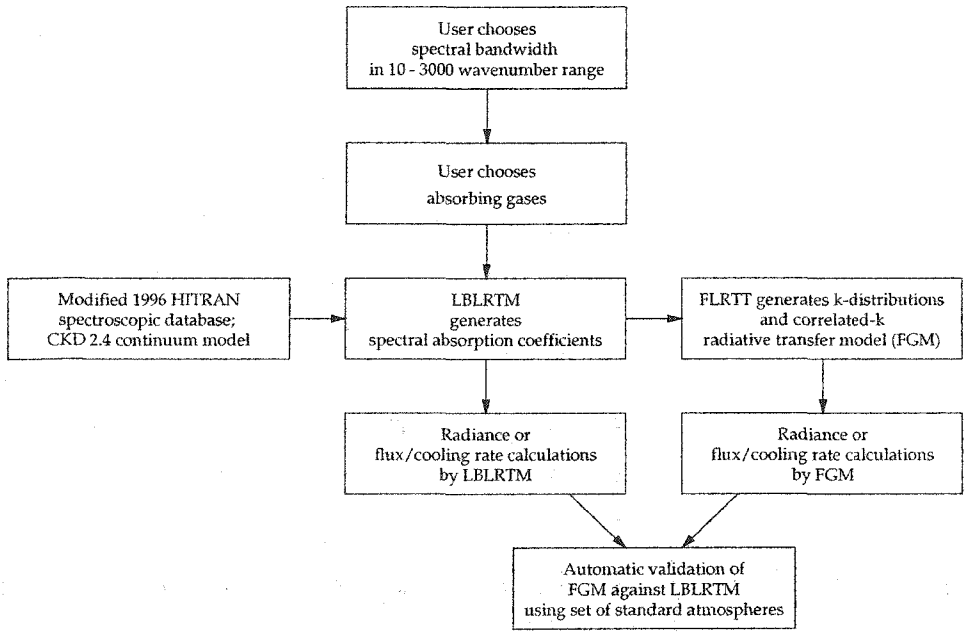

Figure 2.3. Development and validation flow chart of a FLRTT-generated model.

as a function of wavenumber for a spectral interval, produce the k distributions and κ_j values, compile these values and a suite of radiative transfer routines into an executable code (the FGM), and finally to validate the new FGM against LBLRTM for a suite of atmospheres. Figure 2.3 illlustrates the structure of FLRTT and its relation to LBLRTM. If multiple-scattering capability and/or three-dimensional radiative transfer is desired, the modular structure of the k distributions and optical-depth calculation algorithm are easily ported to other radiative transfer algorithms, such as the popular Discrete Ordinate Method (DISORT) [*Stamnes et al.*, 1988] or the Spherical Harmonic Discrete Ordinate Method (SHDOM) [*Evans*, 1998].

To generate a radiative transfer model with FLRTT requires a minimal input of information. First, the application of the model must be declared: "radiance/brightness temperature" or "flux/cooling rates". This dictates the structure of the radiative transfer routines, and the validations calculated at the end of the FLRTT process. Second, the spectral interval for the FGM must be specified, and the absorbing species must be (a) identified and (b) classified as either a *key* or *minor* species. FLRTT includes eight absorbing species: water vapor, carbon dioxide, ozone, nitrous oxide, carbon monoxide, methane,

oxygen, and nitrogen. A key species is defined as having significant absorption within the band, and a minor species has small but nonneglible absorption[5]. The optical depths for a key species are calculated rigorously within the FGM whereas the minor species optical depth calculations are treated with simplifying assumptions. This classification of absorbing species was developed to keep the operational run time for the rapid FGM as short as possible without losing significant accuracy. The algorithms which address absorption by key species permit only two key species to be designated. Since there is a large dynamic range of species abundance with altitude this two key-species restriction would certainly decrease the quality of the calculations. Therefore, two sets of key and minor absorbing species must be identified for the lower atmosphere (surface to 96 mbar) and upper atmosphere (96 mbar to 0.1 mbar).

The choice of number and spacing of intervals in g space is also a a crucial factor in accurate calculation of cooling rates in both the troposphere and stratosphere [*Chou et al.*, 1995; *Mlawer et al.*, 1997]. In many spectral regions the high end of the k distribution, which is dominated by the line centers, drives the cooling rate. An FGM uses 16 intervals in g space, placing seven intervals between g = 0.98 and g = 1.00, to most accurately capture the cooling rates yet retain computational efficiency. Table 2.1 lists the FGM g intervals and weights. Allowing the user of FLRTT to choose this number and spacing or developing the capability of FLRTT to optimize the number of intervals which best suit a spectral band is a topic of future research.

2.2.1 Generation of k Distributions and Optical Depths for Key Species in a FLRTT-Generated Model

The optical depth is the variable at the core of a radiance calculation. In an FGM the total layer optical depth for any subinterval j is the sum of the key-species optical depth and the minor constituent optical depths. An optical depth is a function of both an absorption coefficient and an absorber amount. To obtain accurate optical depths a correlated-k model must address two important issues associated with the absorption coefficient contribution: the pressure and temperature dependence of the absorption coefficients, and the overlap

[5]At this time oxygen and nitrogen are only considered as minor species. Additionally, the halocarbons are not included as an option in FLRTT, but this will be implemented in future versions.

Table 2.1. Boundaries and weights of subintervals in g space. Each spectral band in a FLRTT-Generated Model is divided into 16 intervals in g space. The boundaries and weights of these 16 intervals were chosen to most accurately determine cooling rates yet retain computational efficiency [*Mlawer et al.*, 1997].

Subinterval	Initial g Value	Final g Value	Weight
1	0.00000	0.15275	0.15275
2	0.15275	0.30192	0.14917
3	0.30192	0.44402	0.14210
4	0.44402	0.57571	0.13169
5	0.57571	0.69390	0.11819
6	0.69390	0.79583	0.10193
7	0.79583	0.87911	0.08328
8	0.87911	0.94178	0.06267
9	0.94178	0.98427	0.04249
10	0.98427	0.98890	0.00463
11	0.98890	0.99273	0.00383
12	0.99273	0.99576	0.00303
13	0.99576	0.99798	0.00222
14	0.99798	0.99939	0.00141
15	0.99939	0.99993	0.00054
16	0.99993	1.00000	0.00007

of absorption bands of different species. The pressure and temperature dependencies can be handled in two ways. The first approach is to scale a set of reference κ_j values by a pressure and temperature dependent function for each absorbing species. Alternatively, FLRTT calculates sets of κ_j values for a range of atmospheric pressures and temperatures. These tables of κ_j are stored and later recalled by the FGM. The FGM performs linear interpolation in pressure and temperature to produce an absorption coefficient appropriate for an atmospheric layer. Specifically, for the key-species, the κ_j values are stored for 59 pressure levels from 1050 - 0.01 mbar, successively spaced in increments of 0.2 on a logarithmic scale to permit linear interpolation in log pressure. For each reference pressure level, P_{ref}, κ_j values are stored for values of temperature Θ_{ref}, $\Theta_{ref} \pm 15$ K, $\Theta_{ref} \pm 30$ K, where Θ_{ref} is the temperature corresponding to this pressure in the standard mid-latitude summer (MLS)

atmosphere profile. Extrapolation is used for cases in which a given pressure or temperature is outside the range of stored values. The minor species are treated less rigorously, and are stored for a single reference pressure but a varying range of temperatures.

The capability to efficiently and accurately treat spectral intervals with more than one key species [*Goody et al.*, 1989; *Fu and Liou*, 1992; *Zhu*, 1995; *Mlawer et al.*, 1997] can be handled by several different approaches. The most common approach in climate modeling applications is to utilize the multiplication property of band transmission which states that the band-averaged transmittance is equal to the product of the average transmittance of each absorbing species. The multiplication property is only valid when the correlation between the absorption line positions is small [*Thomas and Stamnes*, 1999]. This assumption may break down over broad spectral intervals [*Sun and Rikus*, 1999] although it generally achieves good accuracy [*Fu and Liou*, 1992]. While the method is conceptionally simple it has been shown to be computationally expensive relative to other methods.

Another approach, developed by *Mlawer et al.* [1997], accurately and efficiently handles overlapping absorption bands. Consider, first, the case in which only two absorbing species are present in the band, and both are considered key species. Rather than consider each absorbing species separately, as is done with the transmission method discussed above, the method of *Mlawer et al.* [1997] characterizes the absorption properties of a two-gas mixture using an additional interpolation variable η, the binary species parameter. The binary species parameter, η, is defined as

$$\eta = \frac{S_A W_A}{S_A W_A + S_B W_B} = \frac{W_A}{W_A + \frac{S_A}{S_B} W_B} \tag{2.23}$$

where A and B are the two key species, S_A and S_B are the respective integrated line strengths in the spectral band, and W_A and W_B are their corresponding layer column amounts. η reflects the relative radiative importance of each species since the products of the integrated line strengths and the species column amounts are equivalent to the average species optical depth in the band. A value of η near zero indicates that species B dominates radiatively whereas a value near one indicates that species A dominates. For each reference pressure and temperature, values of κ_j are calculated and stored for atmospheres with values of η suitably spaced for linear interpolation. Reference κ_j are stored for η values of 0, 1/8, 2/8,...,1 in the lower atmosphere and 0, 1/4, 1/2, 3/4, 1 in the upper

atmosphere. To calculate the absorption coefficients for each value of η column amounts for key species A and B must be chosen. W_A can be established as a function of η and W_B by inverting Equation 2.23. By holding W_B to its MLS value at the reference pressure level for which the κ_j's are being calculated, W_A is uniquely determined for a particular η. The exception is $\eta = 1$ when key species B is set to zero and W_A is set to its MLS value.

The ratio of the column abundance of species A to B can vary by orders of magnitude throughout a typical atmospheric profile. Since the ratio of line strengths is a fixed quantity (the temperature dependence of the line strengths is neglected) the value of η can vary by orders of magnitude between 0 and 1. In particular spectral intervals $k(g)$ has a strong non-linear dependence near $\eta = 0$ and $\eta = 1$. These nonlinearities lead to inaccuracies when using linear interpolation in η to calculate κ_j values in atmospheres whose η values are approaching either 0 or 1. In these problematic spectral bands of RRTM additional κ_j values were calculated and stored for values of η near 0 and 1.

The current FGM employs a modified version of the RRTM key species method in its calculation of optical depths. Following the work of *Sun and Rikus* [1999] the definition of η has been modified from a spectroscopic-based definition to one that is based on the typical abundances of the radiating key species. A pressure-dependent binary species parameter is defined as

$$\eta_P = \frac{S_A W_A}{S_A W_A + \left(\frac{S_A W_{A,MLS}}{S_B W_{B,MLS}}\right)_P S_B W_B} \tag{2.24}$$

which simplifies to

$$\eta_P = \frac{W_A}{W_A + \left(\frac{W_{A,MLS}}{W_{B,MLS}}\right)_P W_B} \tag{2.25}$$

where $W_{A,MLS}$ and $W_{B,MLS}$ are the column amounts of the standard midlatitude summer (MLS) atmosphere at pressure P. With this new definition, atmospheres similar to the MLS atmosphere are spread about $\eta_p = 1/2$. The accuracy of the linear interpolation scheme is compromised less frequently by avoiding non-linear regions of η .

The FGM will calculate the key-species optical depth using interpolation between characteristic absorption coefficients, stored as a function of pressure, temperature and the binary species parameter. The calculation of these stored coefficients is performed only once by FLRTT in a number of steps as outlined in Figures 2.2 and 2.3. The mapping $\nu \rightarrow g$ that will be applied to the absorption coefficients of the key species must first be determined.

This is achieved by calculating spectral optical depths with LBLRTM for an atmospheric layer at the specified pressure and temperature and with key species abundances determined by the value of η_P and all remaining species set to their abundances in the MLS atmospheric profile. The optical depths are spaced by no more than 1/4 of the mean spectral line half-width over the band. These optical depths are then sorted in ascending order and assigned to the subintervals j. This assignment of spectral elements to subinterval j is the mapping $\nu \rightarrow g$. It is important to underscore that this mapping is applied not only to the generation of characteristic absorption coefficients for the key species but also the minor species, which is why all species are included in this mapping.

The mapping is now applied to a set of LBLRTM-generated optical depths for an atmospheric layer at the same pressure, temperature but containing *only* key species[6]. An effective absorption coefficient is obtained for the key-species optical depth $\tau_{key,g}$ from the relation

$$\tilde{k}_g = \frac{\tau_{key,g}}{W} \tag{2.26}$$

where the effective column amount W for the layer is defined for a single key species as

$$W = W_A \tag{2.27}$$

and for a binary species as

$$W = W_A + \left(\frac{W_{A,MLS}}{W_{B,MLS}}\right)_P W_B. \tag{2.28}$$

The characteristic κ_j values are obtained for each key-species k distribution by averaging the $k(g)$ values in each of the subintervals j. FLRTT utilizes linear averaging of the $k(g)$, in contrast to other methods such as: using the absorption coefficient at the mid-point of the interval [*Sun and Rikus*, 2001], transmission-weighted averaging [*Lacis and Oinas*, 1991], or weighting of the transmittance by the Planck function [*Chou et al.*, 1995]. A recent study by *Sun and Rikus* [2001] for a limited spectral interval illustrated that there is no significant differences between the methods for g values less than 0.98 but the difference increases when g is greater than 0.98. The linear average method generally fares well when there is

[6] In the case that water vapor is considered a key species the continuum contribution to the optical depth is considered separately and the LBLRTM-generated optical depths contain only the line contributions. The consideration of the continuum is explained in 2.2.3.

a sufficient number of quadrature points, and avoids the use of an additional interpolation variable, absorber amount, which is required by the latter two methods listed above.

The FGM constructs the key-species optical depth for a layer in an arbitrary atmosphere using a three-dimensional, linear interpolation scheme which uses the stored $\kappa_j(lnP, \Theta, \eta_P)$ values and an effective column amount of the absorbers in the layer. In the upcoming discussion of the interpolation scheme, the subscript j on κ will be replaced by a series of subscripts which describe the pressure, temperature, and η_P dependence of the reference κ values. The interpolation method applies to each subinterval j.

Initially the algorithm finds the stored reference pressure below (P_0) and above (P_1) the pressure of the layer P. The layer optical depth is defined as a weighted sum,

$$\tau_{layer} = (1 - \mathcal{P})\tau_0 + (\mathcal{P})\tau_1 \tag{2.29}$$

$$\mathcal{P} = \frac{P_{layer} - P_0}{P_1 - P_0} \tag{2.30}$$

where τ_0 and τ_1 are the optical depths at the reference pressures. Since the optical depth is the product of the column abundance and an absorption coefficient, Equation 2.29 can be rewritten as

$$\tau_{layer} = (1 - \mathcal{P})W_0\kappa_0 + (\mathcal{P})W_1\kappa_1 \tag{2.31}$$

where W_0 and W_1 and κ_0 and κ_1 are the column amount and characteristic absorption coefficients at the reference pressures.

To determine the values of κ at P_0 and P_1, interpolation must be done to account for the temperature and η_P dependence. At each reference pressure (P = 0,1) the reference temperature below ($\Theta_{0,P}$) and above ($\Theta_{1,P}$) the temperature of the layer are found and

$$\kappa_P = (1 - \mathcal{T}_P)(\kappa_{0,P}) + (\mathcal{T}_P)(\kappa_{1,P}) \tag{2.32}$$

$$\mathcal{T}_P = \frac{\Theta_{layer} - \Theta_{0,P}}{\Theta_{1,P} - \Theta_{0,P}}. \tag{2.33}$$

An additional subscript has been added to the κ's on the right side of the equation to indicate that κ is a function of temperature and pressure. A diagram of the interpolation variables used in the calculation of a single key-species optical depth is presented in Figure 2.4.

For a single key species, there is no η_P dependence and the effective column amounts for the lower and upper reference level are simply equal to the column amount of the single

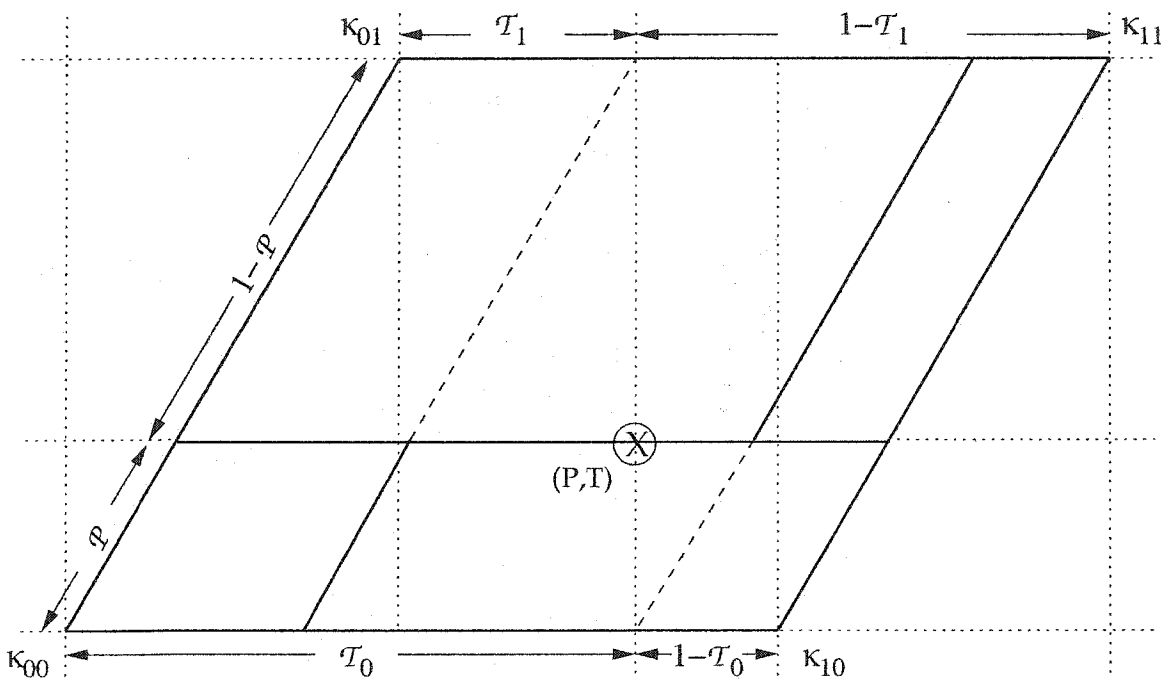

Figure 2.4. Diagram of interpolation method for key-species optical depth calculation. Diagram of the interpolation method used in the calculation of single key-species optical depths at pressure P and temperature T. The stored absorption coefficients are labeled by κ where the first and second subscript represent the reference temperature and pressure levels, respectively.

key species, $W_0 = W_1 = W_{key}$. The layer optical depth for a single key species (Equation 2.31) is explicitly written as

$$\tau_{layer} = W_{key}\{(1-\mathcal{P})[(1-\mathcal{T}_0)\kappa_{00} + (\mathcal{T}_0)\kappa_{10}] + (\mathcal{P})[(1-\mathcal{T}_1)\kappa_{01} + (\mathcal{T}_1)\kappa_{11}]\} \tag{2.34}$$

In a layer in which two key species, A and B, are present, W_0 and W_1 in Equation 2.31 have a pressure dependence, such that

$$W_0 = W_A + \left(\frac{W_{A,MLS}}{W_{B,MLS}}\right)_0 W_B \tag{2.35}$$

$$W_1 = W_A + \left(\frac{W_{A,MLS}}{W_{B,MLS}}\right)_1 W_B \tag{2.36}$$

where W_A and W_B are the layer column abundances.

The η_P dependence of the absorption coefficient is addressed with a final interpolation analagous to the pressure and temperature interpolations. The $\kappa_{\Theta,P}$ from the right side of Equation 2.32 are expanded to

$$\kappa_{\Theta,P} = (1-\mathcal{S}_P)\kappa_{0,\Theta,P} + \mathcal{S}_P\kappa_{1,\Theta,P} \tag{2.37}$$

where $\mathcal{S}_P$ is analagous to $\mathcal{T}_P$ and the η_P dependence of κ is described with the addition of a third subscript to κ on the right side of the equation.

In atmospheric layers in which η_P approaches 0 or 1 linear interpolation between two κ values is not suitable. Instead, a three point interpolation is used when the value of η_P is between 0 and 1/8 or 7/8 and 1 (for the lower atmosphere). In this scheme the simple weighted-sum interpolation is replaced with a quadratic function such that Equation 2.37 becomes

$$\kappa_{\Theta,P}(x) = c_0 + c_1x^2 + c_2x^4 \tag{2.38}$$

where $x = \mathcal{S}_P - 1$ for $\eta \to 0$ and $x = -\mathcal{S}_P$ for $\eta \to 1$. Figure 2.5 presents the nine stored absorption coefficients (+) for each subinterval j as a function of η_P. These coefficients are for a lower-atmosphere spectral band from 500 to 630 cm^{-1}, which contains H_2O and CO_2 as key species. If linear interpolation is used the value of the absorption coefficient would fall on the black line, whereas the absorption coefficient for the quadratic fit would fall on the green line.

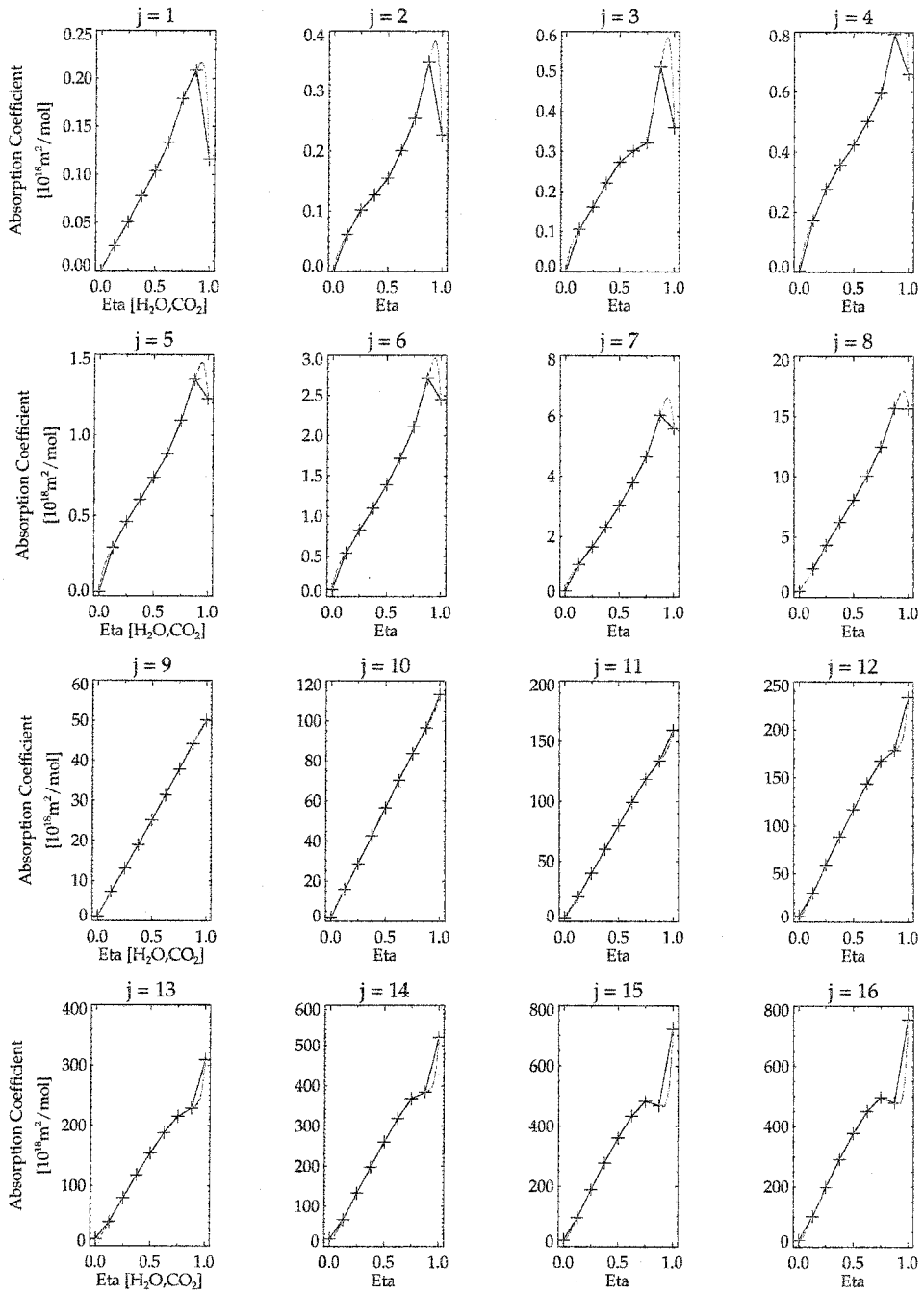

Figure 2.5. Interpolation schemes for η_P in the 500-630 cm^{-1} spectral region. Absorption coefficients for each subinterval j plotted as a function of η_P for the lower-atmosphere spectral interval from 500 - 630 cm^{-1}. H_2O and CO_2 are the key species. The black line represents linear interpolation and the green line represents a quadratic fit.

In summary an FGM calculates optical depth for a mixture of two key gases within an atmospheric layer by (a) calculating η_P from Equation 2.24, and (b) obtaining the optical depth by interpolation from the stored characteristic absorption coefficients at appropriate reference values of P, Θ, and η_P. *Sun and Rikus* [1999] employed a scheme similar to the FGM to address the overlapping absorption issue. *Sun and Rikus* [1999] studies found a speed improvement of an order of magnitude from the standard transmission multiplication method to the η_P method, and that the η_P method performed better relative to the line-by-line method since the assumptions behind the standard transmission multiplication method fail for wide spectral bands.

2.2.2 Generation of k Distributions and Optical depths for Minor Species in a FLRTT-Generated Model

The key species method has been designed for only two absorbers. However, in many spectral intervals more than two absorbers exist. After choosing the two most radiatively important species, the remaining active species are treated by a less rigorous but similar method. For each minor species m in the lower atmosphere FLRTT generates $\kappa_{j,m}$ values for only one reference pressure and two corresponding MLS temperatures $(\Theta_{ref}, \Theta_{ref} - 15K)$. The reference pressure is chosen by FLRTT from the pressure grid on which the key-species characteristic absorption coefficients are stored. The mapping $\nu \rightarrow g$ for the full atmospheric profile at the reference pressure is applied to the absorption coefficients from only the minor species, and the results are averaged for each subinterval in g space to obtain $\kappa_{j,m}$. The number of stored $\kappa_{j,m}$ values is extended to 19 equally spaced temperature grid points from the original two temperature points using interpolation and extrapolation. This adequately accounts for the temperature dependence of the species' absorption yet does not have significant computational overhead in building the k distributions. When two key species are present in a spectral interval, the minor species $\kappa_{j,m}$ are generated not only for the temperatures, as noted above, but also for each combination of key species used to generated the stored, pressure-dependent binary species parameter, η_p. This method is applied identically to any minor species in the upper atmosphere.

To calculate the minor species optical depth for an arbitrary atmospheric layer, the FGM utilizes a linear interpolation similar to that used in the key species optical depth

calculation. When a single key species is present in the layer, a weighted-sum interpolation in temperature is performed to obtain the appropriate absorption coefficient. When two key species are present in the layer, for each j subinterval, linear interpolation is performed in two dimensions: temperature and η_m, where η_m is defined as

$$\eta_m = \frac{W_A}{W_A + \left(\frac{W_{A,MLS}}{W_{B,MLS}}\right)_{PM} W_B} \tag{2.39}$$

where the subscript PM indicates the reference pressure for which $\kappa_{j,m}$ was initially calculated and the subscripts A and B refer to column abundances for the key species. The minor species optical depth is the product of the absorption coefficient and the column abundance of the minor species.

Treatment of Oxygen and Nitrogen

The procedure for optical depth calculations of oxygen and nitrogen is modified from that described above. Absorption by oxygen and nitrogen is collision-induced, resulting in smooth and continuous absorption features. There are two spectral regions in which the nitrogen continuum is active, 10-350 cm^{-1} and 2085-2670^{-1}, and one active oxygen region, 1340-1850 cm^{-1}. While a number of theoretical approaches to modeling collision-induced absorption have been proposed, experimental techniques have proven more accurate [*Borysow and Frommhold*, 1986; *Lafferty et al.*, 1996; *Thibault et al.*, 1997]. With the appropriate assumptions and experimental data the oxygen and nitrogen absorption coefficients are given in the form:

$$k_{O_2}(\nu, \Theta, \rho_{O_2}, \rho_{air}) = \rho_{O_2}\rho_{air}B_{O_2}(\nu, \Theta) \tag{2.40}$$

$$k_{N_2}(\nu, \Theta, \rho_{N_2}, \rho_{air}) = \rho_{N_2}\rho_{air}B_{N_2}(\nu, \Theta) \tag{2.41}$$

where ρ is a density and B is a function of a density-normalized collision-induced absorption coefficient (in units of amagat[7]) and an appropriate scale factor.

The absorption properties of oxygen and nitrogen are computed within the continuum model CKD 2.4. FLRTT stores the κ_j values as a function of the coefficient B rather than the

[7] An amagat is the ratio of the density of a species to the density of the species at STP, the standard temperature and pressure of 273.15 K and 1 atmosphere, respectively.

conventional absorption coefficient; the final optical depth calculation requires multiplication of the absorber amount, the appropriate density factors, and the oxygen/nitrogen κ_j value.

The methodology for calculating the key-species *k* distributions, described in the above text, differs from the physics in the original version of RRTM. In the original RRTM the *k* distributions were calculated from a single profile in which all species not determined by the value of η were set to their respective MLS abundances, excluding only the contribution from the water vapor self-continuum. Therefore, the *k* distribution would *also* include contributions from the continua and minor species. In bands in which it was known that minor species were present, an algorithm was in place to calculate the radiative impact of any deviation of the minor species concentration from its MLS value. In an FGM the optical depth is the sum of individual contributors, eliminating the need for the additional minor species algorithm described above. The new method is computationally more expensive for FLRTT since two sets of line-by-line calculations must be performed to build the key-species *k* distributions. However, it is now easier to update individual components when spectroscopic advances occur.

2.2.3 Generation of *k* Distributions and Optical depths for the Water Vapor Continuum in an FGM

As outlined in the introductory chapter the water vapor continuum is a critical component of the longwave radiative budget. The water vapor continuum absorption coefficient k_{wvc} has both a self-broadened and foreign-broadened component, and is given by the relation:

$$k_{wvc}(\nu,\Theta) = \nu \tanh(\frac{hc\nu}{2k_B\Theta}) \left[(\frac{\rho_s}{\rho_0}) C_s(\nu,\Theta) + (\frac{\rho_f}{\rho_0}) C_f(\nu) \right] \tag{2.42}$$

where h is the Planck's constant, c is the speed of light, k_B is Boltzmann's constant, ρ_s, ρ_f and ρ_0 are the water vapor, dry air, and air densities, and C_s and C_f are self- and foreign-broadened continuum coefficients. The term $\nu \tanh(\frac{hc\nu}{2k\Theta})$ is referred to as the radiation term. The coefficients used in CKD 2.4 were obtained by comparing measurements with LBLRTM calculations for the local line contributions and applying a fitting technique to the differences. Note that the self-continuum coefficient has temperature dependence while the foreign-continuum coefficient does not. For atmospheric conditions the foreign

continuum dominates absorption near water vapor band centers while the self continuum dominates outside band centers, such as in the atmospheric windows.

The water vapor self-continuum and foreign continuum are explicitly addressed in layer optical depth calculations in an FGM. The self-continuum is treated only in the lower atmosphere while the foreign continuum is present in both the lower and upper atmosphere. FLRTT calculates and stores the water vapor self, $\kappa_{j,wvc-s}$, and foreign continuum coefficients, $\kappa_{j,wvc-f}$. The radiation term is built into the stored continuum coefficients. The procedures used ensures that the continuum contribution is included in a manner consistent with the correlation between the continuum absorption spectrum and the full absorption spectrum in the band. For the self continuum the $\kappa_{j,wvc-s}$ depend both on the mapping $\nu \rightarrow g$ in the band and the temperature-dependent self continuum coefficients. To accomodate these dependencies the $\kappa_{j,wvc-s}$ are calculated for two reference layers from the MLS profile with temperatures 296 and 260 K and pressures at 970 and 475 mbar, respectively. Exponential interpolation is then used to expand the number of stored $\kappa_{j,wvc-s}$ values on an equally spaced temperature grid. The foreign continuum coefficients do not have a temperature dependence but do depend on the mapping. The $\kappa_{j,wvc-f}$ are calculated for three reference layers in the lower atmosphere (Θ = 296, 260, 224 K and P = 970, 475, 219 mbar) and two reference layers in the upper atmosphere (Θ = 224, 260 K and P = 219 and 3 mbar). The continuum optical depths are constructed by determining the correct $\kappa_{j,wvc-s}$ and $\kappa_{j,wvc-f}$ using linear interpolation in temperature and by multiplying these new values with a scaling factor in accordance with Equation 2.42 and the water vapor column abundance.

At the current time there is no η dependence in the stored continuum κ_j values. For consistency with the minor species the next version of FLRTT will treat the η dependence. For the current applications of FLRTT this approximation suffices.

2.3 Radiative Transfer Algorithms in an FGM

Once the total optical depth has been calculated from the individual optical depths of the absorbing species, a radiative transfer algorithm is called by the FGM to calculate either the radiance at a given angle or fluxes and cooling rates. For each subinterval in a spectral

band the radiative transfer equation is solved layer-by-layer.

In a non-scattering atmosphere the radiative transfer equation used to calculate the upward radiance for each layer is written as (see Equation 2.22)

$$I_{\nu}^{+} = \sum_{j} W_j \left[B_{eff,j} + [I_{j,0}^{+} - B_{eff,j}] e^{-\kappa_j z} \right] \tag{2.43}$$

where $I_{j,0}^{+}$ is the radiance entering the layer and $B_{eff,j}$ is the layer effective Planck function. The same equation applies to downward radiance, where the + sign is replaced by the − sign. While the determination of κ_j was straightforward, the determination of $B_{eff,j}$ is not. Each subinterval j contains a myriad of frequencies which have been obtained from the mapping $\nu \rightarrow g$. Corresponding to each frequency there is a unique value of the Planck function. The range of the Planck function values depends on the range of frequencies associated with each subinterval, thereby limiting the accuracy of approximating the effective Planck function with a single value obtained at a single frequency [*Mlawer et al.*, 1997]. The valuation of the effective Planck function, which is a combination of both the Planck function at the layer and boundary temperature(Equation 2.17), in each subinterval is handled in a two-part procedure. First, FLRTT calculates and stores the band-integrated Planck function, which depends only on temperature, on a 1 K temperature grid. The FGM can then call these values to calculate the integrated Planck function for a given temperature using linear interpolation. Second, for an appropriate reference temperature and pressure, FLRTT utilizes the mapping for the full atmospheric profile $\nu \rightarrow g$ to calculate the fraction of the band-integrated Planck-function radiance associated with each subinterval j such that

$$B_j = \frac{1}{N} \sum_{i=1}^{N} B_{\nu,i}(\Theta) \tag{2.44}$$

where N is the total number of frequency values contributing to the subinterval. The Planck fraction, f_j, for each subinterval is defined by the relation

$$f_j = \frac{B_j W_j}{\frac{1}{\nu_2 - \nu_1} \int_{\nu_1}^{\nu_2} B_{\nu}(\Theta) d\nu} \tag{2.45}$$

where W_j is the quadrature weight of the subinterval, and ν_1 and ν_2 are the frequency limits of the band. These fractions are then stored for later use by the FGM.

For each subinterval and layer, the layer and boundary Planck functions can be calculated in an FGM by multiplying the stored fraction of the band-integrated Planck function, f_j, with the integrated Planck function, obtained by linear interpolation from the grid of stored integrated Planck functions. The layer and boundary Planck functions are then easily combined into the effective Planck function for the subinterval.

In bands with two key species, f_j is calculated both as a function of temperature and the pressure-dependent binary species parameter. Therefore, an interpolation in η_P space, identical to that used to determine the minor species absorption coefficient, is performed to obtain the appropriate f_j.

When an FGM is constructed for simulations of atmospheric radiance measured by an instrument, the instrument's filter function must also be accounted for in the radiative transfer calculations. The method of calculating the Planck function for a subinterval, as just described, is expanded to include this filter function. The integrated product of the Planck function and the appropriate normalized filter function value ($\mathcal{F}$) is stored on a 1 K grid. The Planck fraction definition is then expanded to

$$f_{j,instrument} = \frac{H_j W_j}{\frac{1}{\nu_2 - \nu_1}\int_{\nu_1}^{\nu_2} B_\nu(\Theta) d\nu} \tag{2.46}$$

$$H_j = \frac{1}{N}\sum_{i=0}^{N} B_{\nu,i}(\Theta)\mathcal{F}_{\nu,i}(\Theta) \tag{2.47}$$

where H_j is the average value of the product of the Planck function and the filter function, and all other variables are analogous to the previously defined Planck fraction.

Each time the radiance for a layer and subinterval is calculated there are numerous expoentiations and divisions associated with the transmittance. To decrease computational time in the radiative transfer calculations, a high-resolution table, which contains the transmittance as a function of optical depth, is created at the beginning of each execution of an FGM. This table results in substantial savings in computing resources, which is a benefit to any climate modeling applications.

It is noteworthy that the linear-in-τ method was not fully implemented in the original version of RRTM or in the version of LBLRTM available at the time of its development. In the original RRTM, a simple Pade approximant to Equation 2.17 was used to calculate the effective Planck function for a layer. This method was correct in the optically thick

and thin limits but deviated to some extent from the linear-in-τ method elsewhere. It had the advantage of being computationally fast and the parameters of the Pade approximant could be adjusted as necessary. The new look-up table method retains the efficiency of the Pade method and the accuracy of the linear-in-τ method.

The radiances calculated by the methods described above can be integrated over a hemisphere to yield fluxes. At this time an FGM uses 3 angles from standard Guassian quadrature, but a future upgrade to FLRTT will permit additional choices. From the fluxes the cooling rates are calculated.

2.4 Validation of the FGM

After FLRTT has constructed an FGM it provides a set of validations to the user. The validations of the FGM are performed against the line-by-line model LBLRTM. For applications in which the FGM will be used for calculation of satellite radiances LBLRTM and FGM are run for a set of 42 atmospheric profiles. For calculations in which fluxes are desired the standard version of FLRTT validates the FGM for only three standard atmospheric profiles (midlatitude summer, tropical, and subarctic winter). The difference in the number of atmospheric profiles used in the validation is simply a matter of FLRTT-timing since it takes a considerable amount of computing time for LBLRTM to calculate fluxes. However, future versions of FLRTT will offer the user the choice to use either the small or full set of atmospheres.

The success of the FGM in reproducing the LBLRTM-calculated radiation quantities must be assessed by the individual user. Accuracy requirements for an FGM are likely to be user specific. FLRTT produces a diagnostic set of plots as it generates the FGM, which can be used to determine if improvements are possible.

Examples of the FLRTT validation are presented in Chapter 3 and 4.

2.5 Summary

Radiative transfer computations in the infrared spectral region are notoriously demanding due to the complex line structures of the many radiatively active gases. Numerous satel-

lite and ground-based sensors currently in development and operation require accurate and rapid radiative transfer calculations for both data analysis and retrieval. Although many capable radiative transfer techniques and models are widely available, a significant amount of time is often required to tailor the model to the user's needs. A FLexible Radiative Transfer Tool (FLRTT) has been developed to facilitate the generation of rapid radiative transfer models.

Features of FLRTT include:

- Flexible bandwidths chosen by the user within the 10 - 3250 cm^{-1} range.
- Permits inclusion of major molecular species and their accompanying continua.
- Creates k distributions and incorporates them into the correlated-k radiative transfer algorithm employed by LBLRTM.
- Modular structure provides easy portability of optical depths for an atmospheric profile into other radiative transfer algorithms, such as DISORT [*Stamnes et al.*, 1988] or SHDOM [*Evans*, 1998].
- Easy inclusion of instrument filter functions into the calculations.
- Automatic validation of FLRTT-generated radiative transfer model with LBLRTM.

Chapter 3

Evaluation of Upper Tropospheric Water Vapor in the National Center for Atmospheric Research Community Climate Model, CCM3

This thesis chapter discusses a recent evaluation of upper tropospheric water vapor in the National Center for Atmospheric Research Community Climate Model, CCM3, using modeled and observed High-resolution Infrared Radiation Sounder measurements (HIRS) [*Iacono et al.*, 2003]. In particular the development and validation of a radiative transfer model, RRTM_HIRS, used in this evaluation is discussed. RRTM_HIRS was created using the FLexible Radiative Transfer Tool, extensively documented in Chapter 2.

3.1 Background

Water vapor is an active constituent in many physical processes in the atmosphere. It is a major contributor to Earth's energy budget through radiative energy transfer and the release of latent heat from condensation during cloud formation. Water vapor is an element of a fundamental, but complex, climate feedback in which warmer ocean temperatures increase the water vapor amount in the atmosphere via evaporation and, hence, increase

water vapor absorption. The increased absorption further warms the surface and amplifies the original temperature perturbation.

The radiative properties and global distribution of atmospheric water vapor must be simulated precisely by numerical weather prediction models (NWPs) and general circulation models (GCMs) to accurately predict weather and climate change. Essential to diagnosing deficiencies in modeled water vapor processes are the large observational data sets obtained from satellites. *Clough et al.* [1992] demonstrated that the spectral outgoing longwave radiation at the top of the atmosphere is partially a function of the distribution of water vapor within the atmosphere and the absorption characteristics of water vapor itself (bottom panel, Figure 1.3). This suggests that comparisons between modeled radiances and/or brightness temperatures within specific spectral intervals to those measured by satellites will yield useful information from which to gauge the success of large-scale models in capturing water vapor processes.

A number of studies over the last decade have made comparisons between model calculations and satellite measurements with the focus of assessing upper tropospheric water vapor (UTWV) distribution in several popular GCMs and NWPs [*Soden and Bretherton*, 1994; *Salathe et al.*, 1995; *Iacono et al.*, 2003]. Overall the models captured the general features of the global water vapor distribution but did not simulate well the regional details. A recent study extended earlier efforts by evaluating UTWV simulated by the widely used National Center for Atmospheric Research Community Climate Model, CCM3. This was achieved by comparing modeled top of the atmosphere, clear-sky brightness-temperatures from CCM3 to those observed by two channels of the spaceborne HIRS. CCM3 was modified to utilize the accurate longwave rapid radiative transfer model, RRTM, for all internal flux calculations. Since RRTM does not calculate radiances for satellite channels a separate radiance module, RRTM_HIRS, was developed to produce the clear-sky HIRS brightness temperatures. The physics between RRTM and RRTM_HIRS is consistent; therefore, the radiative transfer calculations are closely linked to line-by-line calculations. This removes most of the uncertainty from the radiative transfer calculations, and allows the dynamical components of CCM3 to be more effectively evaluated.

3.2 Mechanics of Evaluating Upper Tropospheric Water Vapor in CCM3

The primary climate simulations for this analysis used a version of CCM3 modified to include RRTM and RRTM_HIRS; a secondary set of simulations was performed using the original CCM3 longwave radiation module and the original accompanying radiance module. The only difference in the two simulations are the radiative transfer routines and the cloud overlap treatment. For these simulations the globe was divided into grid cells (2.8° latitude by 2.8° longitude), and the vertical column of each grid cell was divided into 18 layers. Modeled HIRS brightness temperature data were output from CCM3 every six hours.

3.2.1 HIRS Channels

The *Iacono et al.* [2003] evaluation of UTWV utilizes radiances from the HIRS instrument, a component of the Television Infrared Observation Satellite Operational Vertical Sounder (TOVS). Since 1978 a TOVS package has flown aboard the polar-orbiting series of National Ocean and Atmospheric Administration (NOAA) satellites. The model analysis period 1982 - 1984, following the Atmospheric Model Intercomparison Project protocol, corresponds to the NOAA-6, NOAA-7, and NOAA-8 satellites. Two channels from the NOAA-7 HIRS package were selected as the basis for this study: a temperature channel (CH04, 675 - 732 cm^{-1}), and a water vapor channel (CH12, 1382 - 1572 cm^{-1}). CH04 radiances are sensitive to the temperature profile from the middle troposphere to the lower stratosphere, while CH12 radiances are sensitive to tropospheric water vapor. Although this study focused on UTWV it is important to establish any possible contamination from clouds in the CH12 measured radiances. CH04 was utilized for this purpose; brightness temperature differences of 2 K or less in CH04 indicate that cloud and temperature effects are not responsible for differences between calculated and measured CH12 brightness temperatures.

This study uses the *Bates et al.* [1996] HIRS database, which contains cloud-cleared HIRS brightness temperatures for monthly and 5-day means on a 2.5° x 2.5° grid for the period examined. The largest source of error in this dataset is the cloud-clearing algorithm,

Table 3.1. RRTM_HIRS radiative transfer module spectral bands and absorbing species in each spectral band.

		Species Implemented in RRTM_HIRS			
		Lower Atmosphere		Upper Atmosphere	
HIRS Channel	Wavenumber Range, cm^{-1}	Key	Minor	Key	Minor
04	674.74 - 731.89	CO_2	H_2O, O_3	CO_2	O_3
12	1382.4 - 1571.7	H_2O	CH_4, O_2	H_2O	CH_4, O_2

so the brightness temperature comparisons were limited to 60° South to 60° North. Estimated brightness temperature errors for all sources combine to 2.48 K for an individual measurement and less than 1 K for longer-term averages [*Wu et al.*, 1993].

3.2.2 RRTM_HIRS Module

A key element of the *Iacono et al.* [2003] comparison is the development of RRTM_HIRS, which calculates clear-sky radiances/brightness temperatures in HIRS CH04 and CH12 using the CCM3-generated atmospheric profile. RRTM_HIRS was created using the Flexible Radiative Transfer Tool (FLRTT), which generates correlated-*k*, longwave radiative transfer models for user-specified spectral intervals. The physics of RRTM_HIRS is consistent with RRTM, the radiative transfer model embedded in CCM3. Table 3.1 presents the spectral widths of the two channels, listed with their respective key and minor absorbing species.

An important aspect of this model development is the inclusion of the instrument spectral response function for each channel. Figure 3.1 shows the spectral response function for NOAA-7 HIRS CH04 and CH12 superimposed upon the LBLRTM-calculated radiance at the top of the atmosphere. Monochromatic radiances were calculated assuming a middle latitude summer atmosphere, and interpolated to a one wavenumber grid for clarity of presentation. The CH04 spectral response function peaks just to the right of the center of the strongest carbon dioxide band at 667 cm^{-1}, whereas the CH12 spectral response function peaks to the left of the center of the ν_2 water vapor absorption band at 1595 cm^{-1}. In a line-by-line radiative transfer model the monochromatic radiance calculations are ex-

plicitly convolved with this function, but this isn't possible in a correlated-k band model. FLRTT constructed the RRTM_HIRS module to fold the spectral response function into the stored Planck fractions, which represent the portion of the integrated Planck function associated with each g value (see detailed description in Section 2.3).

Validation of the RRTM_HIRS Module

A set of guidelines and benchmarks for radiation codes have recently been established by two large model intercomparison efforts [*Soden et al.*, 2000; *Garand et al.*, 2001]. The *Garand et al.* [2001] and *Soden et al.* [2000] studies compared line-by-line models not only against one another but also against both narrow-band and single-band radiative transfer models. The line-by-line radiative transfer model intercomparison showed general agreement to within 0.5 K in terms of equivalent blackbody brightness temperatures, while the rapid models agree to within 1 K. *Garand et al.* [2001] established a desired accuracy of 0.25 K standard deviation against a line-by-line radiative transfer model, but noted that this is not possible in all satellite channels.

For the validation of the RRTM_HIRS module an ensemble of 42 atmospheric profiles, each containing 43 pressure levels, from the *Garand et al.* [2001] study were used. For these profiles RRTM_HIRS-calculated brightness temperatures was compared to those generated by the line-by-line radiative transfer model LBLRTM (version 5.21). Figure 3.2 shows the brightness temperature differences between the two models for HIRS CH04 and CH12. The mean and standard deviation for RRTM_HIRS - LBLRTM CH04 for the 42 atmospheres is -0.05 and 0.22 K, respectively; for CH12 the mean and standard deviation is 0.012 and 0.05 K, respectively. These standard deviations are within the benchmark set by the *Garand et al.* [2001] study.

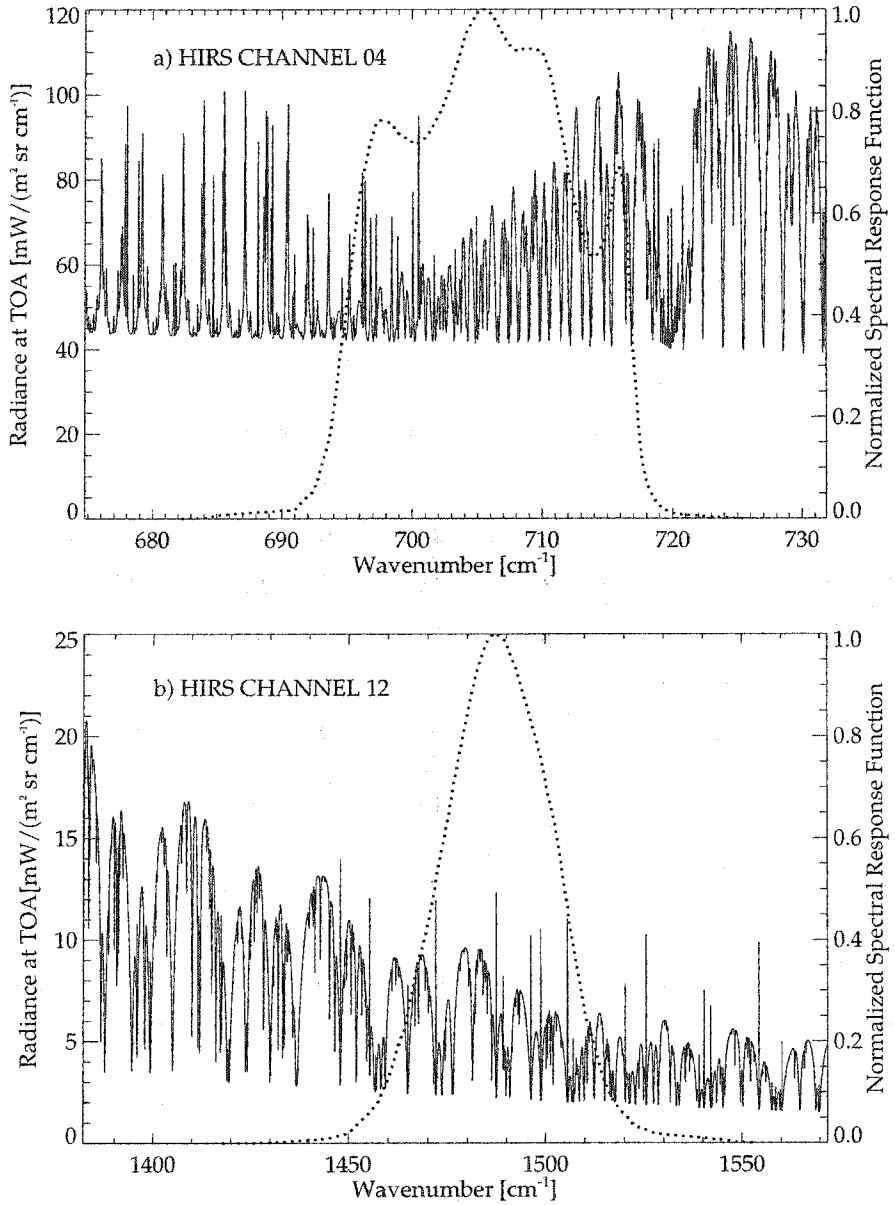

Figure 3.1. NOAA-7 HIRS Channel 4 and 12 spectral response function and top of the atmosphere radiances simulated by LBLRTM. The normalized spectral response functions (dotted line) for NOAA-7 HIRS a) CH04, and b) CH12 are superimposed upon the LBLRTM-calculated radiances at the top of the atmosphere (solid line). The LBLRTM-calculated radiances must be convolved with the HIRS spectral response function to simulate the radiance measured by HIRS.

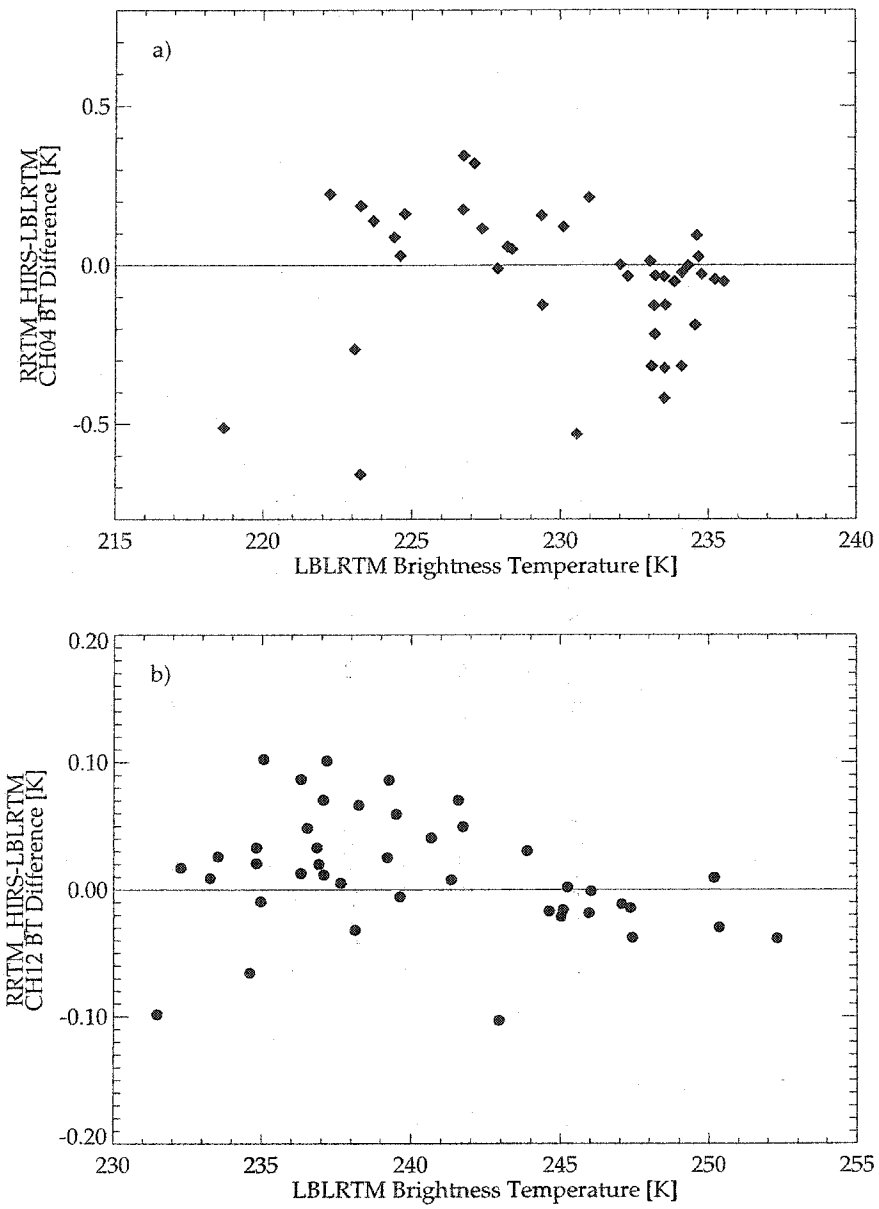

Figure 3.2. Validation of RRTM_HIRS against LBLRTM for 42 atmospheric profiles. Brightness temperature differences between RRTM_HIRS and LBLRTM for the NOAA-7 HIRS a) CH04, and b) CH12 for 42 atmospheric profiles from the *Garand et al.* [2001] intercomparison. The mean and standard deviation for RRTM_HIRS - LBLRTM CH04 is -0.05 and 0.22 K, respectively; for CH12 the mean and standard deviation is 0.012 and 0.05 K, respectively.

3.3 CCM3 Upper Tropospheric Water Vapor Evaluation

A summary of the *Iacono et al.* [2003] study is presented in Figure 3.3 through Figure 3.6. First, analysis of the brightness temperatures of CH04 revealed that the cloud-clearing method applied to the HIRS data was effective. Figure 3.3 shows the difference between the observed and simulated CH04 brightness temperatures for June, July, and August (JJA) 1982 (left panels) and for December, January, and February (DJF) 1982-1983 (right panels). Results are shown for both CCM3 with the highly accurate longwave-RRTM package (that is, RRTM and RRTM_HIRS) (top panels) and original CCM3 longwave radiation package (bottom panels). Similar brightness temperatures differences are shown for JJA 1983 and DJF 1983-1984 in Figure 3.4. The area-weighted average and root-mean-square ('AVG' and 'RMS' in Figure 3.3 and Figure 3.4) seasonal brightness temperatures differences are less than 1.5 K and 0.9 K, respectively, over latitudes 60° South to 60° North. This good agreement between the HIRS-measured brightness temperatures and those calculated by CCM3/RRTM leads to two important conclusions that: a) there are relatively small model temperature errors in the upper troposphere for tropical and middle latitudes, and b) the cloud-clearing method applied to observed HIRS data was effective.

Also noteworthy in Figure 3.3 and Figure 3.4 is that the CCM3 simulation with the RRTM package produced warming at high latitudes relative to the original CCM3, and, therefore, reduced the error between observed and modeled brightness temperatures. This warming is attributed to the improved treatment of the foreign water vapor continuum by RRTM/RRTM_HIRS.

CH12 provides a suitable means from which to evaluate the CCM3-modeled upper tropospheric distribution of specific humidity since the emission it observes peaks between 500 and 200 mbars. Figure 3.5 shows the CH12 1982-1983 seasonal differences between the HIRS-observed and CCM3-calculated CH12 brightness temperatures for JJA (left panels) and DJF (right panels) for the CCM3/RRTM (top panels) and the original CCM3 simulations (bottom panels). Figure 3.6 depicts seasonal brightness temperatures for 1983-1984. In regions of relatively low UTWV radiation from lower and warmer layers in the atmosphere passes through the upper troposphere and stratosphere to the satellite sensor. Conversely, in regions of higher UTWV radiation from the lower layers is absorbed and the

emission measured by the satellite comes from the higher, colder, absorbing layers (and thus colder brightness temperatures). Differences between the measured and modeled brightness temperatures in Figure 3.5 and Figure 3.6 are analyzed in context of these concepts. A positive difference indicates that the radiation calculated by CCM3 is emitted from higher (and colder) atmospheric layers, which is a consequence of higher UTWV in the model relative to the real atmosphere. A negative difference indicates that the modeled UTWV is lower than that in the real atmosphere. Globally the AVG brightness temperature and RMS for the two figures are less than 2 K. These differences may be partly explained by problems with the modeled temperature fields and by diurnal sampling issues described by *Engelen et al.* [2000]. While the global averages seem small it is important to note the large regional differences of up to 5-10 K, which corresponds to a greater than 50% discrepancy between modeled and real upper-tropospheric specific humidity. CCM3 overestimates UTWV relative to HIRS particularly over Central America, the Indian Ocean, and Western Pacific, whereas in the sub-tropical dry areas there is good agreement between model and measurement. The CH12 regional differences persist not only on weekly time scales but also through several annual cycles.

In both seasons, the CCM3/RRTM and the original CCM3 calculations show overall similar regional brightness temperature differences. Reiterating that the primary difference in these two simulations is the radiation algorithm, it can then be concluded that the discrepancies in UTWV are primarily caused by deficiences in the dynamical component of the climate model rather than the radiation component. However, there are seasons and regions (such as over North America in DJF 1982-1983) in which utilizing the accurate RRTM package measurably impacts the model dynamics, yielding significantly improved agreement with the CH12 HIRS measurements.

3.4 Summary

Satellite radiances are a useful tool for examining the robustness of temperature fields and UTWV calculated by climate models. The *Iacono et al.* [2003] study, which compared modeled clear-sky brightness temperatures to those observed from space by HIRS, suggested that the UTWV calculated by the commonly used global climate model CCM3 can have

regional moist and dry discrepancies of 50% or more. These biases are likely due to issues with the dynamical component of CCM3.

In future years additional sounders will be spaceborne, providing greater spectral resolution with which to validate GCMs. Additionally, climate models undergo continuous improvements in which they incorporate knowledge gained from studies such as the one presented in this thesis chapter.

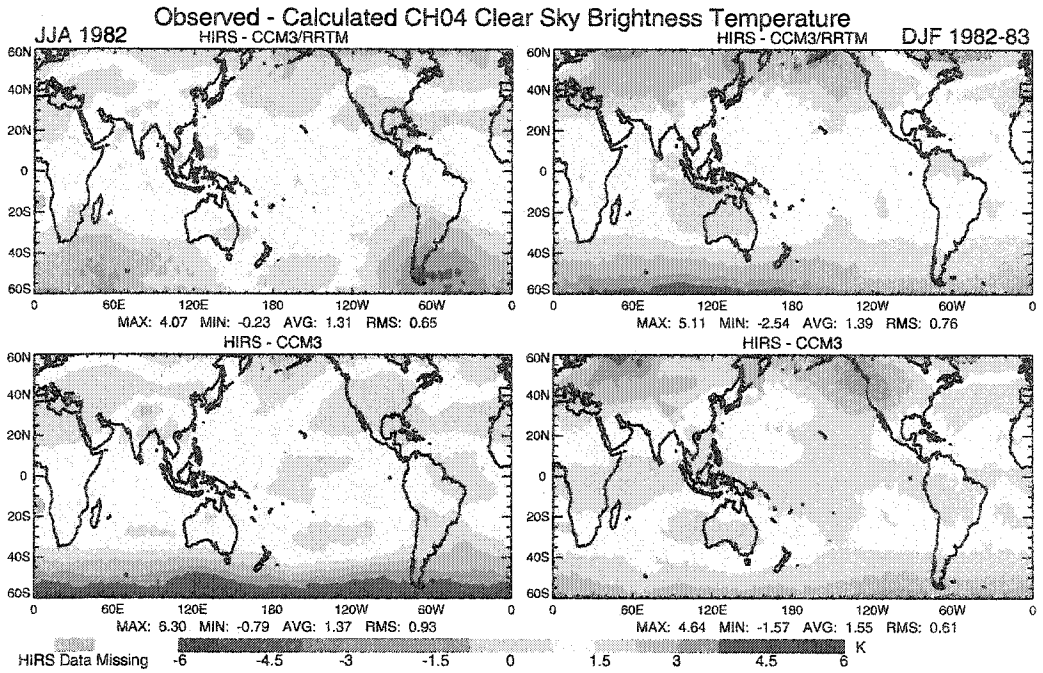

Figure 3.3. Difference between HIRS-CH04 observed and CCM3-calculated 1982-1983 seasonal brightness temperatures. Difference between HIRS-observed and CCM3-calculated seasonal brightness temperature for HIRS CH04. Difference between the HIRS-observed and CCM3-calculated CH04 clear-sky brightness temperature [in Kelvin] for June, July, August 1982 (left panels) and December, January, February 1982-1983 (right panels). Results are shown for CCM3 with the RRTM package (top panels) and with the original CCM3 longwave models (bottom panels). Reproduced from *Iacono et al.* [2003].

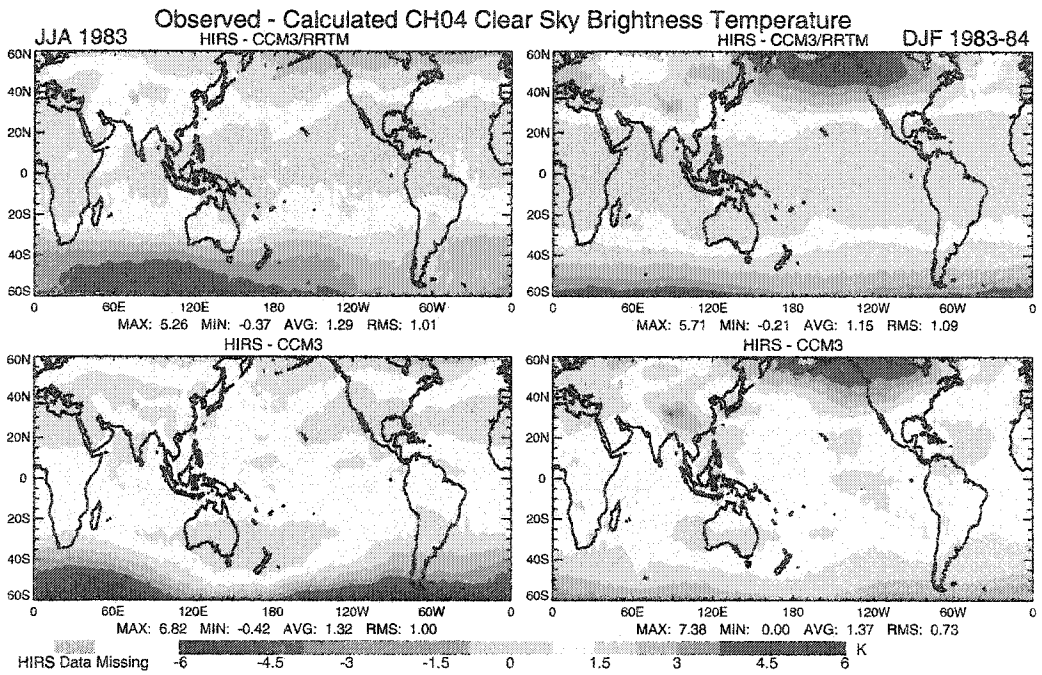

Figure 3.4. Difference between HIRS-CH04 observed and CCM3-calculated 1983-1984 seasonal brightness temperatures. Difference between the HIRS-observed and CCM3-calculated CH04 clear-sky brightness temperature [in Kelvin] for June, July, August 1983 (left panels) and December, January, February 1983-1984 (right panels). Results are shown for CCM3 with the RRTM package (top panels) and with the original CCM3 longwave models (bottom panels). Reproduced from *Iacono et al.* [2003].

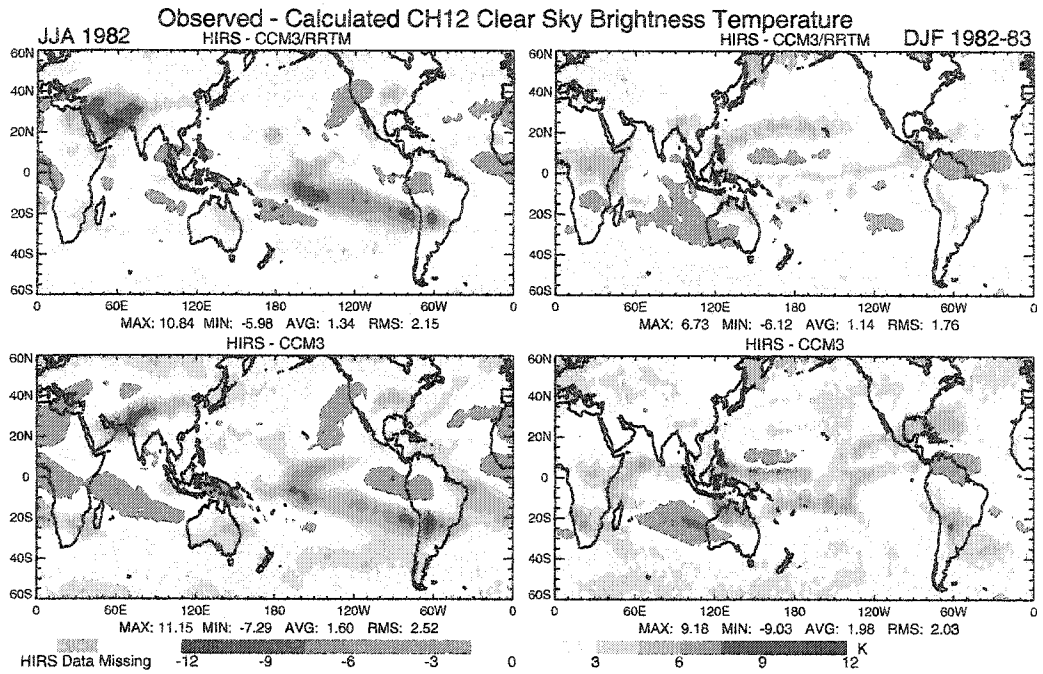

Figure 3.5. Difference between HIRS-CH12 observed and CCM3-calculated 1982-1983 seasonal brightness temperatures. Difference between the HIRS-observed and CCM3-calculated CH12 clear-sky brightness temperature [in Kelvin] for June, July, August 1982 (left panels) and December, January, February 1982-1983 (right panels). Results are shown for CCM3 with the RRTM package (top panels) and with the original CCM3 longwave models (bottom panels). Reproduced from *Iacono et al.* [2003].

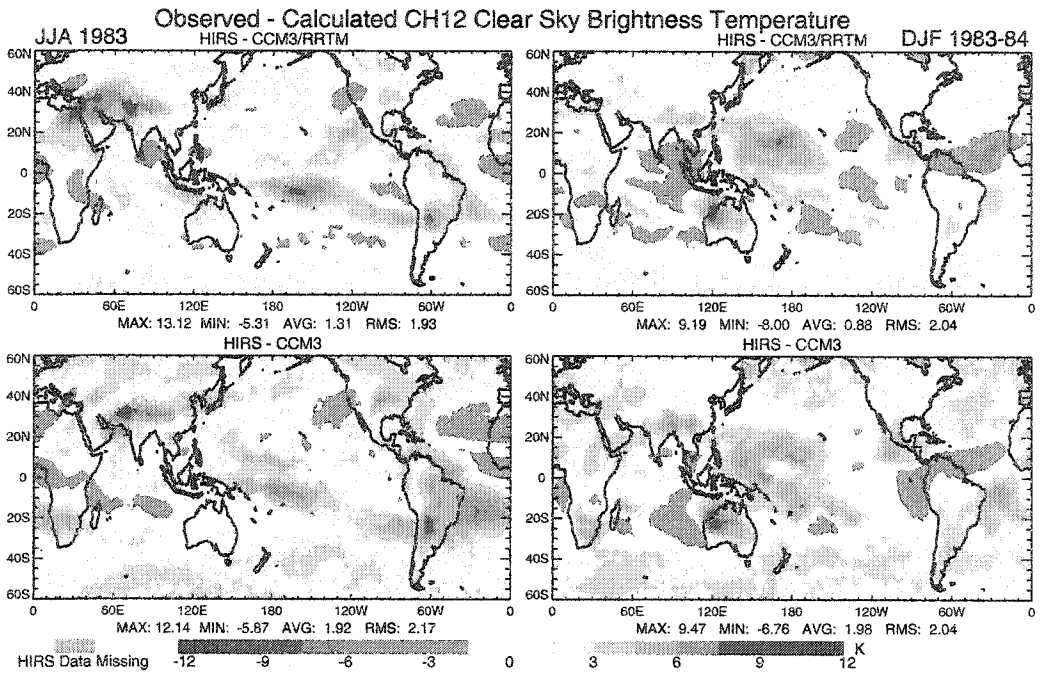

Figure 3.6. Difference between HIRS-CH12 observed and CCM3-calculated 1983-1984 seasonal brightness temperatures. Difference between the HIRS-observed and CCM3-calculated CH12 clear-sky brightness temperature [in Kelvin] for June, July, August 1983 (left panels) and December, January, February 1983-1984 (right panels). Results are shown for CCM3 with the RRTM package (top panels) and with the original CCM3 longwave models (bottom panels). Reproduced from *Iacono et al.* [2003].

Chapter 4

The Rapid Longwave Radiative Transfer Model: A New Version

In 1997 a rapid longwave radiative transfer model, RRTM, was developed by Dr. Eli Mlawer and colleagues at Atmospheric and Environmental Research, Inc. [*Mlawer et al.*, 1997]. The development of RRTM was funded by the Department of Energy Atmospheric and Radiation Measurement Program (ARM), whose primary mission is to improve radiative transfer modeling in general circulation models (GCMs). RRTM was designed to accurately and efficiently calculate fluxes and cooling rates using the correlated-*k* method for radiative transfer. The absorption coefficients utilized by RRTM were obtained directly from the line-by-line radiative transfer model LBLRTM, and the output of RRTM was validated against LBLRTM. Since LBLRTM has been validated against many radiation data sets, including those produced by the ARM program, a link has been established between RRTM and radiation observations. The speed of execution of RRTM and the accuracy of its flux and heating rate calculations have made it a popular radiative transfer model. Users of RRTM could choose between using a full-version of RRTM and a climate-model version. Differences in the two versions are related to efficiency issues, such as reducing the number of quadrature points used in the correlated-*k* scheme from 256 to 140.

RRTM has been adopted in a number of numerical weather prediction and climate models. In June 2000 RRTM became the operational longwave radiation scheme at the European Center for Medium-Range Weather Forecasts [*Morcrette et al.*, 2001]. Studies

at ECMWF indicated that RRTM positively impacted a large range of parameters, particularly the surface radiation and the stratospheric temperatures [*Morcrette et al.*, 2001; *Morcrette*, 2002]. Much of this improvement can be attributed to the more accurate water vapor absorption, particularly the treatment of the water vapor continuum, relative to the original ECMWF longwave radiation scheme.

In August 2002, AER, Inc. released version 3.0 of RRTM. This model has a number of significant algorithm changes from the previously released RRTM v2.3 (released in 1998), as well as updated k distributions derived from newer line parameters. The most important algorithmic changes involve the calculation of the molecular optical depths. The new algorithms improve the ability of RRTM to calculate fluxes and cooling rates under atmospheric conditions which differ substantially from the standard mid-latitude summer profile. Examples of these improvements will be illustrated in the validation section below.

The core of RRTM v3.0 was generated by the Flexible Radiative Transfer Tool (FLRTT), extensively described in Chapter 2. FLRTT was used to calculate the k distributions for the absorbing species and the initial set of band-by-band validations. However, to maintain compatibility with the RRTM v2.3 and to make some particular improvements RRTM v3.0 has additional features not available in a FLRTT-generated model. The additional features will be noted throughout the text.

The development of RRTM was sponsored by the Department of Energy Atmospheric Radiation Measurement Program, and is available to the scientific community on the AER web-site (http://rtweb.aer.com).

4.1 General Features of RRTM v3.0

RRTM v3.0 calculates fluxes and cooling rates for the longwave spectral region (10-3250 cm^{-1}) for arbitrary clear and cloudy sky atmospheres. The molecular species treated in this model are water vapor, carbon dioxide, ozone, methane, nitrous oxide, carbon monoxide, oxygen, nitrogen, and the common halocarbons[1]. The longwave region is divided into 16 spectral bands, and the atmosphere is divided into two regimes to account for the dy-

[1]FLRTT does not compute the halocarbon contribution. The halocarbon absorption coefficients were taken directly from RRTM v2.3 and are not discussed further in this thesis

namic range of abundance of certain species with altitude. Table 4.1 notes which species considered for each spectral band and altitude. The spectral bandwidths were chosen to coincide, where possible, with the major spectral absorption band (as shown in Chapter 1, Figure 1.1).

Table 4.1. RRTM v3.0 spectral bands and absorbing species included in each band.

		Species Implemented in RRTM v3.0			
		Lower Atmosphere		Upper Atmosphere	
Band Number	Wavenumber Range, cm^{-1}	Key Species	Minor Species	Key Species	Minor Species
1	10-350	H_2O	N_2	H_2O	N_2
2	350-500	H_2O		H_2O	
3	500-630	H_2O, CO_2	N_2O	H_2O, CO_2	N_2O
4	630-700	H_2O, CO_2		CO_2, O_3	
5	700-820	H_2O, CO_2	O_3, CCl_4	CO_2, O_3	CCl_4
6	820-980	H_2O	CO_2, CFC-11*, CFC-12		CFC-11*, CFC-12
7	980-1080	H_2O, O_3	CO_2	O_3	CO_2
8	1080-1180	H_2O	CO_2, O_3, N_2O, CFC-12, CFC-22*	O_3	CO_2, N_2O, CFC-12, CFC-22*
9	1180-1390	H_2O, CH_4	N_2O	CH_4	N_2O
10	1390-1480	H_2O		H_2O	
11	1480-1800	H_2O	O_2	H_2O	O_2
12	1800-2080	H_2O, CO_2			
13	2080-2250	H_2O, N_2O	CO_2, CO		O_3
14	2250-2380	CO_2		CO_2	
15	2380-2600	N_2O, CO_2	H_2O, N_2		
16	2600-3250	H_2O, CH_4		CH_4	

* Optical depths of these halocarbons are increased to account for other absorption bands of these species that are not implemented.

The FLRTT-generated absorption coefficients in RRTM v3.0 were obtained from LBLRTM v5.21. The line parameters were obtained from HITRAN 1996 database [*Rothman et al.*, 1998]. The water vapor lines in the HITRAN 1996 database in the spectral range of 500 to 2880 cm^{-1} were replaced with water vapor line parameters measured by Dr. Bob Toth at the Jet Propulsion Laboratory (personal communication to AER, Inc.). Line coupling coefficients have been utilized for the important Q-branches of carbon dioxide. These line coupling coefficients are consistent with the HITRAN 1996 carbon dioxide line strengths. The water vapor, nitrogen, and oxygen continuum coefficients were obtained from CKD 2.4. Since RRTM v3.0 was constructed a new line parameter database has been released, HITRAN 2000. There are no significant changes between the line parameter database used to build RRTM v3.0 and HITRAN 2000.

RRTM v3.0 considers only the processes of absorption and emission in its radiative transfer algorithm, that is, multiple-scattering events are ignored. In the longwave spectral region this is a common assumption, valid for clear-sky calculations. Several options are available in RRTM v3.0 for flux calculations: a) the diffusivity approximation, and b) up to 4 angles in standard Gaussian quadrature.

A full summary of the RRTM v3.0 updates is presented in Appendix A.

4.2 Clear Sky Validations

RRTM v3.0 has been validated against the accurate line-by-line model LBLRTM under a variety of atmospheric conditions. As *Mlawer et al.* [1997] point out there two primary advantages to comparing the rapid model with the line-by-line model: the accuracy of the rapid model algorithms are best tested against the line-by-line model on which they are based, and model-model validations do not have to account for inaccuracies in the specification of the atmospheric state, which is a crucial component in model-observation comparisons. Model-model and model-observations validations are complementary, and model-observation comparisons are presented in Section 5.

The validations presented in this section are for a set of 42 atmospheres which encompass a wide range of temperature and trace gas profiles. An ensemble of 42 atmospheric profiles were selected by *Garand et al.* [2001] for a radiative transfer model intercompar-

ison[2]. Profiles 1-6 are composed of the six standard atmospheres (tropical (TRP), mid-latitude summer (MLS), mid-latitude winter (MLW), sub-arctic summer (SAS), sub-arctic winter (SAW), and U.S. standard (US)). Profiles 7-18 are characterized by increasing mean atmospheric temperature. Profiles 19-30 are characterized by increased integrated water vapor. Profiles 31-42 are characterized by increasing the total ozone column.

Fluxes are computed using a three-angle integration. Note that the validations presented compare RRTM against LBLRTM v6.01, CKD 2.4, and an updated HITRAN 2000 database. These are not the set of models from which RRTM v3.0 was constructed. This set of validations illustrates how well RRTM v3.0 performs against the latest spectroscopic advancements, rather than how the rapid model algorithms compare against those which they were built to emulate. However, the changes between a recent LBLRTM-package and the LBLRTM-package used to generate RRTM v3.0 are not significant for longwave broadband flux calculations.

The format for the plots in the validation sections is similar to those presented in *Mlawer et al.* [1997]. However, the atmospheric profiles referred to as the standard atmospheres in *Mlawer et al.* [1997] differ from the standard atmospheres in the *Garand et al.* [2001] set. Therefore, a direct comparison of the plots in the two papers can not be made.

4.2.1 Standard Atmosphere Validations

The atmospheric profiles for the six standard atmospheres are illustrated in Figure 4.1. Figures 4.2, 4.3, 4.4 show the full longwave results for three of the standard atmospheres (TRP, MLS, SAW). The left-side panels on each figure shows the reference quantity calculated by LBLRTM, and the right-side panels on each figure shows the difference between the calculations from RRTM and LBLRTM (that is, RRTM-LBLRTM). The upward, downward, net flux[3], and the cooling rate are plotted as a logarithmic function of pressure. The residuals for each flux quantity do not exceed 1.0 W m^{-2} at any altitude and are a small percentage of their respective values; the residuals for the cooling rates do not exceed 0.3 K day^{-1} at any altitude. The flux and cooling rate residuals for the TRP and MLS atmosphere are quite similar in both the lower and upper atmosphere. However, the shape of the net-flux

[2]These profiles were used in the HIRS-CCM3 validations in Chapter 3

[3]The net flux is defined as upward flux minus downward flux.

tropospheric residuals for the colder, drier SAW atmosphere differs from that of the MLS and TRP atmospheres. The differences cannot be contributed to a single band, but rather to all bands in which water vapor is an absorber. Overall these figures demonstrate that RRTM v3.0 agrees well with LBLRTM for a wide range of atmospheric parameters.

Additional insight into the broadband differences between LBLRTM and RRTM is gained from an examination of the band-by-band validations. Figure 4.5, 4.6, and 4.7 present the band-by-band validations for the MLS atmosphere. The individual band results again show good agreement between RRTM v3.0 and LBLRTM, indicating that the good broadband results are not due completely to cancellation of errors. Figure 4.5 shows the results for the first five bands, spanning the spectral range (10-820 cm^{-1}) where the bulk of the Planck emission resides. The left-side panels show the reference quantities calculated by LBLRTM, and the right-side panels shows the residuals between RRTM v3.0 and LBLRTM. Residuals in these bands do not exceed 0.4 W m^{-2} for any flux quantity. Band 5, in which water vapor and carbon dioxide are the key absorbers, has the largest percentage error in upward and downward flux, primarily caused by the lack of correlation of the k distributions in the tropospheric layers. In the lower troposphere water vapor and carbon dioxide make important contributions in the determination of the mapping $\nu \rightarrow g$ of the absorption coefficients. Since the water vapor concentration decreases with increasing altitude the carbon dioxide becomes increasingly dominant in determining the mapping $\nu \rightarrow g$ in the upper troposphere. The lack of correlation leads to increasing errors in the flux residuals in the mid to upper troposphere. The cooling rate residuals do not exceed 0.2 K day^{-1} in any band at any altitude.

Figure 4.6 shows the flux and cooling rate residuals for spectral region from 820-1390 cm^{-1}. This spectral space contains the important atmospheric window, from which a large portion of the surface emission escapes to space when the atmosphere is clear. The largest net flux residual occurs in the 1180-1390 cm^{-1} band. This band suffers from the same correlation problem as that described for the 700-820 cm^{-1} band. The largest cooling rate residual occurs in the ozone band from 980-1080 cm^{-1}. This residual just exceeds 0.1 K day^{-1} in the stratosphere, which is less than 10% of the reference cooling rate for that altitude.

Figure 4.7 presents the band residuals for the bands from 1390-3250 cm^{-1}. The mag-

nitude of the residuals in these bands are small relative to the first 9 bands. The largest flux residual does not exceed 0.05 W m^{-2}, and the largest cooling rate residual does not exceed 0.02 K day^{-1}. This cooling rate residual occurs in the 1800-2080 cm^{-1} band, where no absorbing species have been included in RRTM.

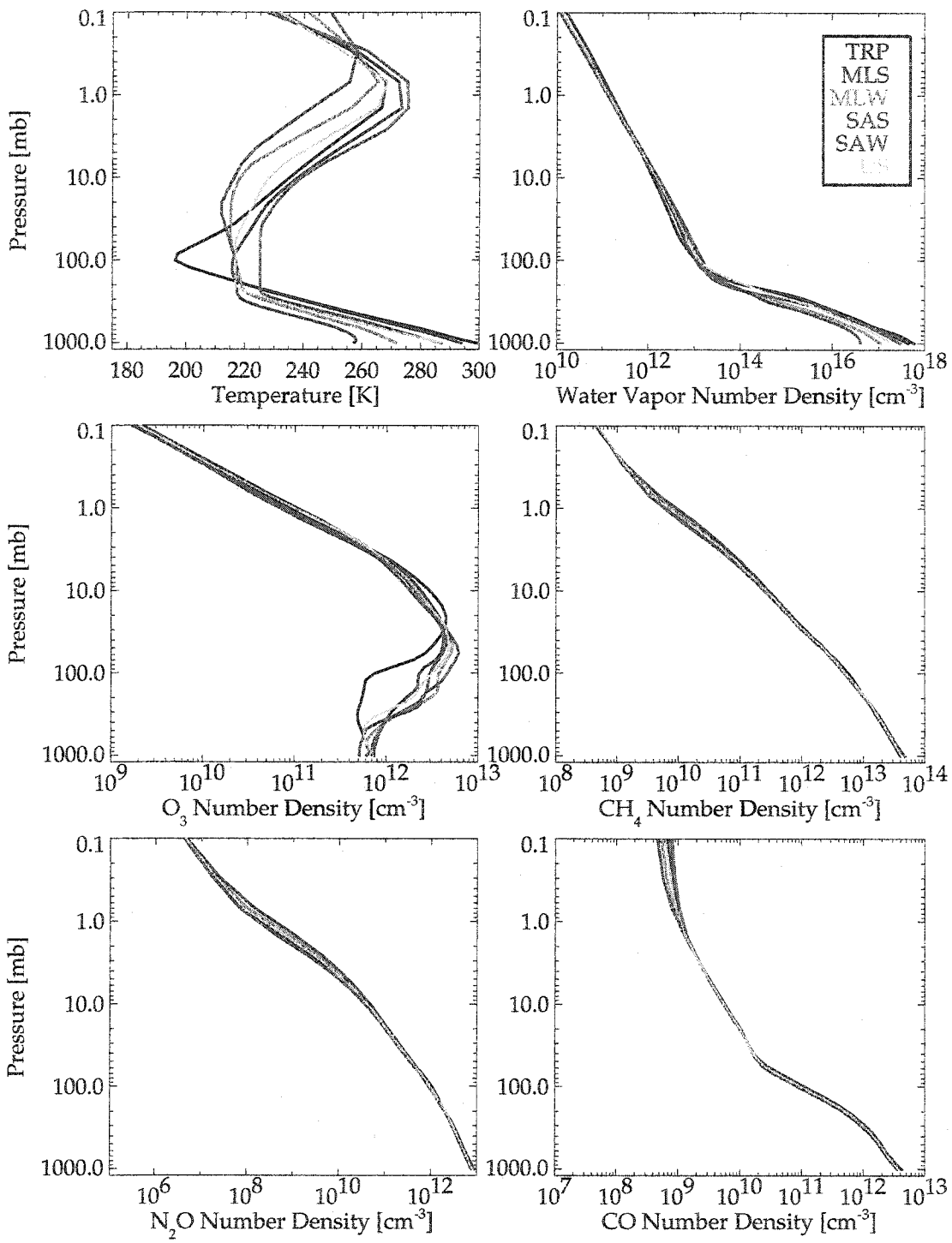

Figure 4.1. Atmospheric Parameters for Standard Atmospheres. The atmospheric profiles for the six standard atmospheres, including the temperature profile and the number density profile of some of the radiatively active gases included in RRTM.

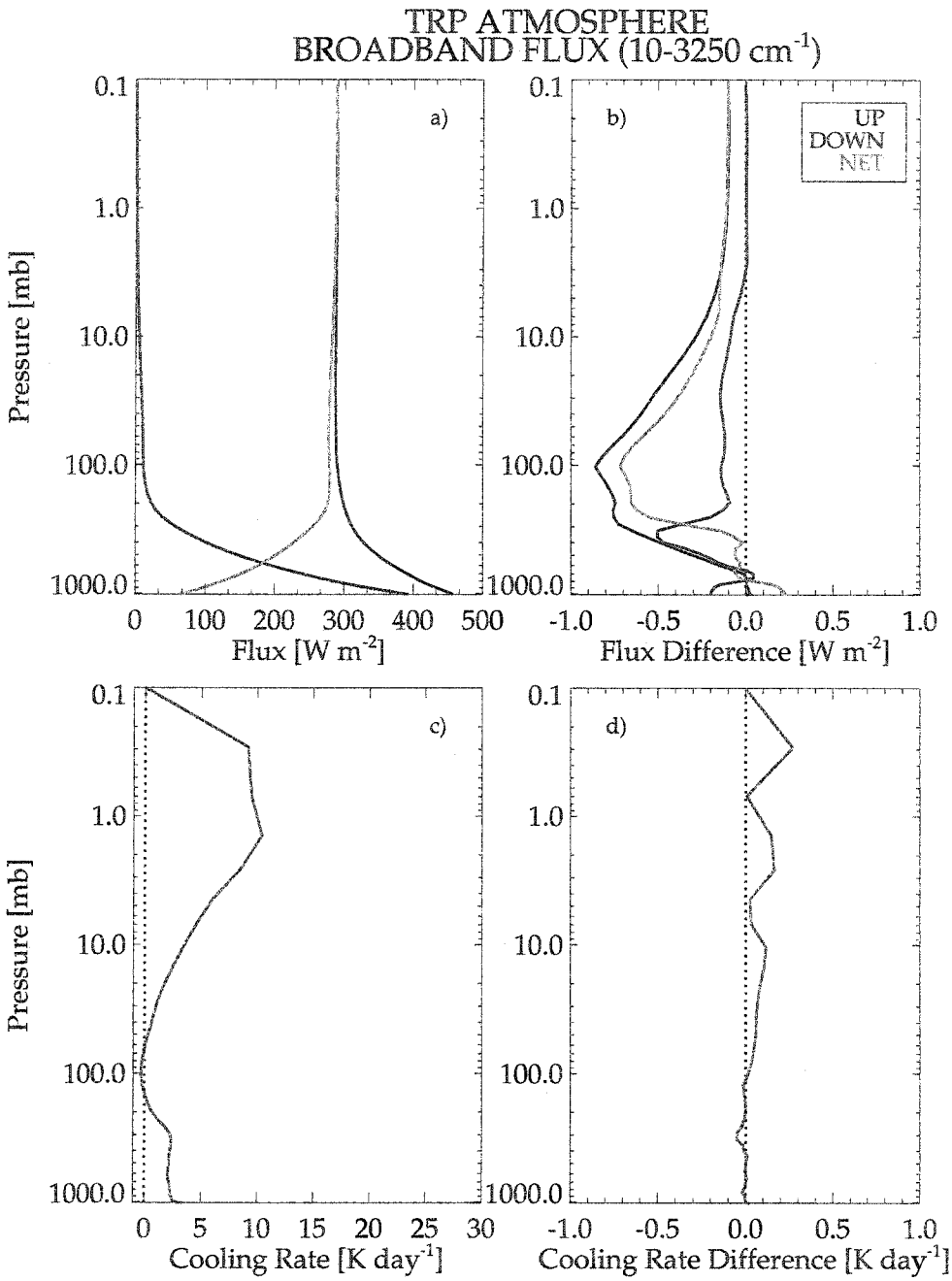

Figure 4.2. Broadband flux residual profile for tropical atmosphere. Tropical (TRP) atmosphere: (a) spectrally integrated longwave up, down, and net fluxes calculated by LBLRTM, (b) flux differences between quantities calculated by RRTM and LBLRTM (RRTM-LBLRTM), (c) spectrally integrated cooling rates calculated by LBLRTM, and (d) cooling rate differences between RRTM and LBLRTM. All quantities are plotted as a logarithmic function of pressure.

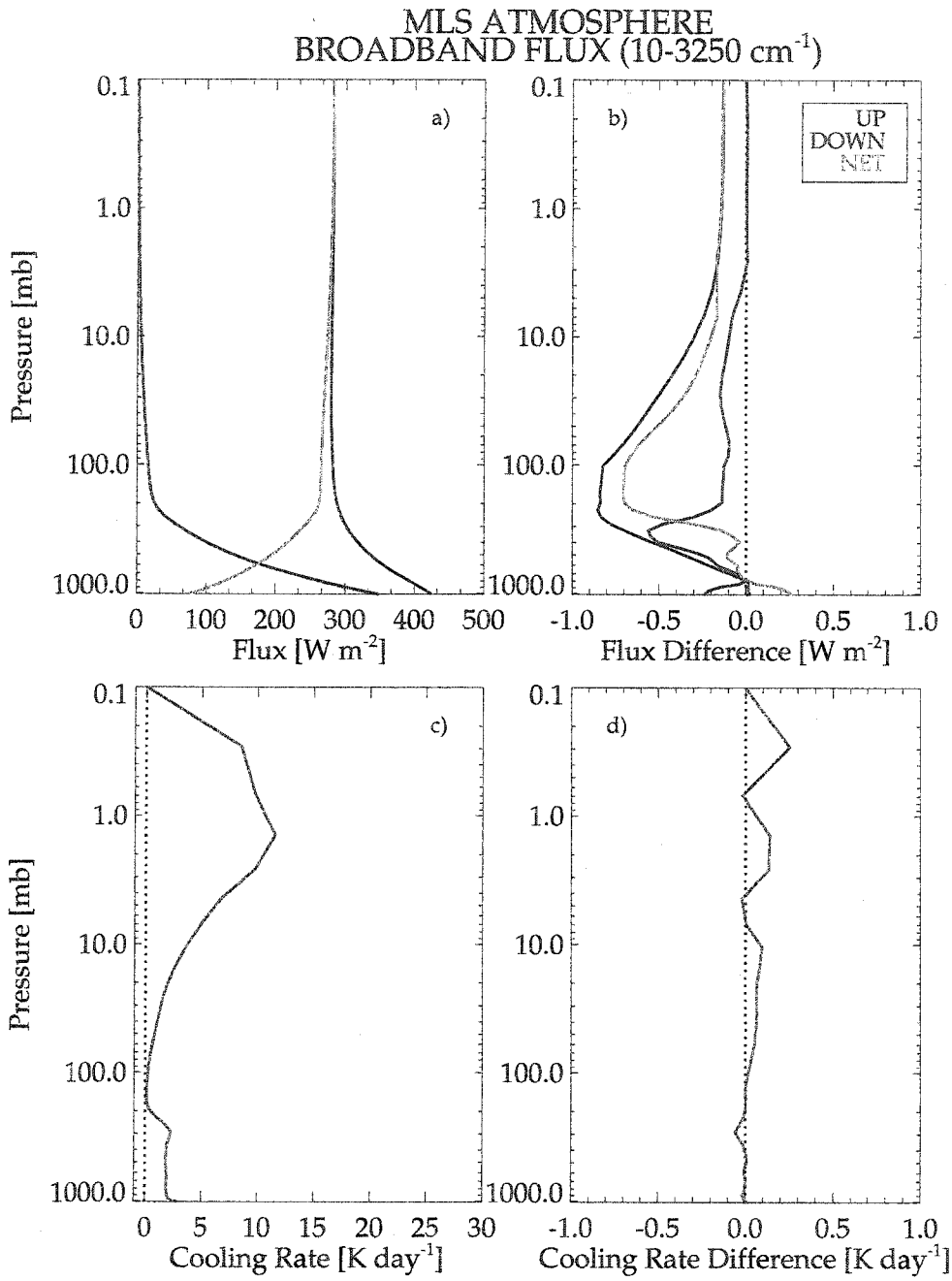

Figure 4.3. Broadband flux residual profile for mid-latitude summer atmosphere. Mid-Latitude summer (MLS) atmosphere: (a) spectrally integrated longwave up, down, and net fluxes calculated by LBLRTM, (b) flux differences between quantities calculated by RRTM and LBLRTM (RRTM-LBLRTM), (c) spectrally integrated cooling rates calculated by LBLRTM, and (d) cooling rate differences between RRTM and LBLRTM. All quantities are plotted as a logarithmic function of pressure.

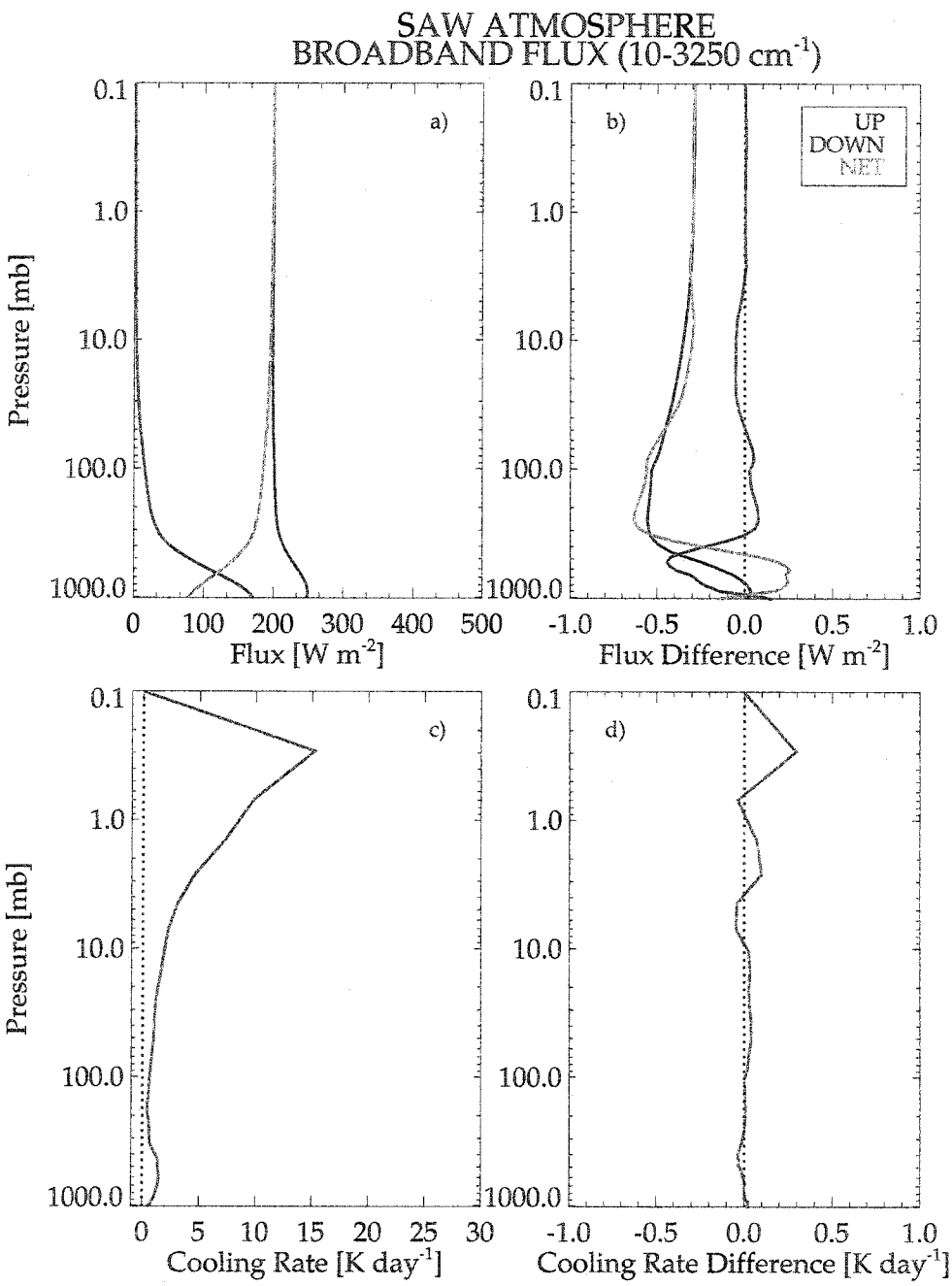

Figure 4.4. Broadband flux residual profile for sub-arctic winter atmosphere. Sub-Arctic winter (SAW) atmosphere: (a) spectrally integrated longwave up, down, and net fluxes calculated by LBLRTM, (b) flux differences between quantities calculated by RRTM and LBLRTM (RRTM-LBLRTM), (c) spectrally integrated cooling rates calculated by LBLRTM, and (d) cooling rate differences between RRTM and LBLRTM. All quantities are plotted as a logarithmic function of pressure.

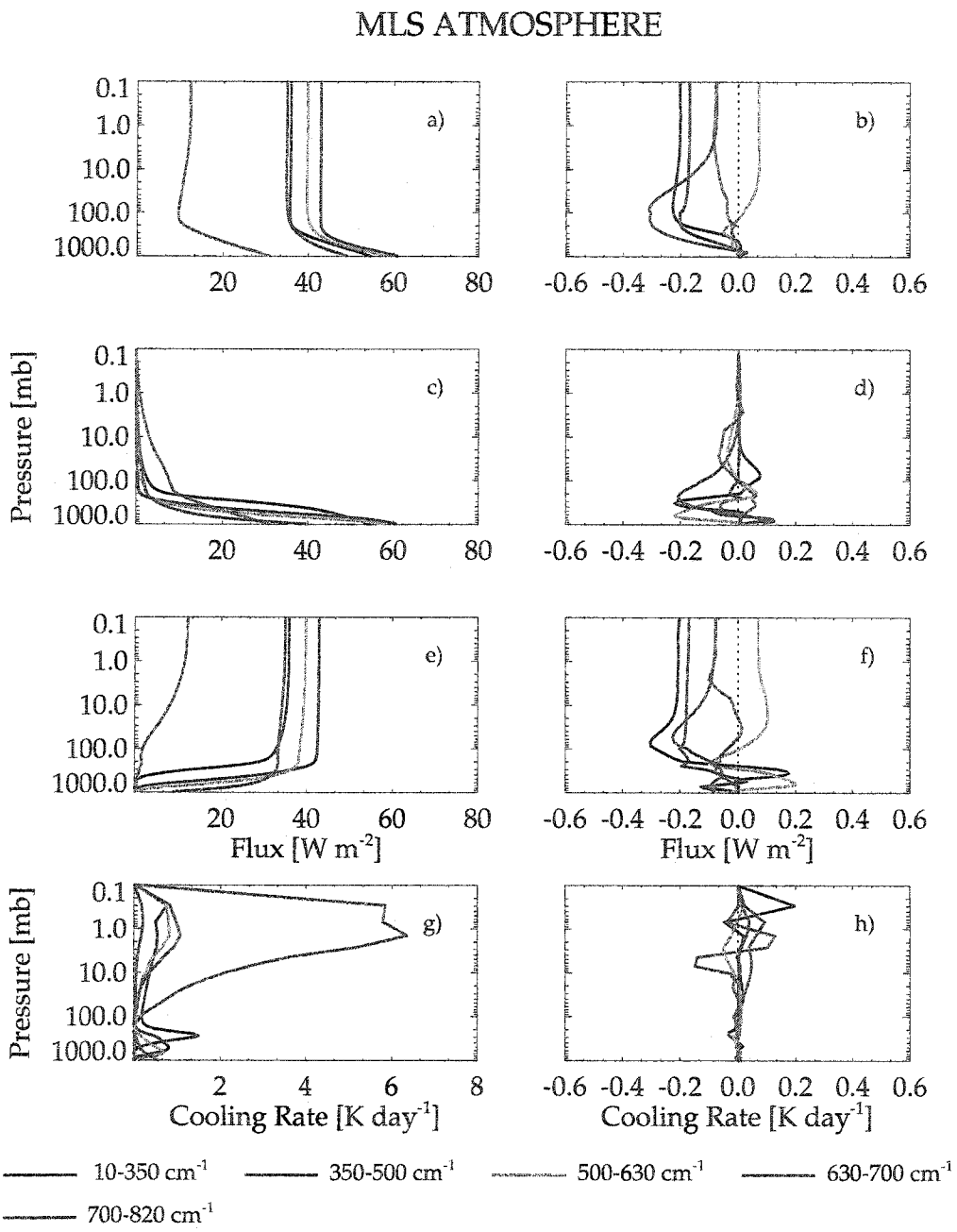

Figure 4.5. RRTM band 1-5 vertical profile flux residuals for MLS atmosphere. Spectrally integrated (a) up, (c) down, (e) net fluxes, and (g) cooling rates for band 1-5 calculated by LBLRTM for the mid-latitude summer (MLS) atmospheres. Difference between RRTM and LBLRTM for the quantities are shown in panel (b), (d), (f), and (h), respectively. All quantities are plotted as a logarithmic function of pressure.

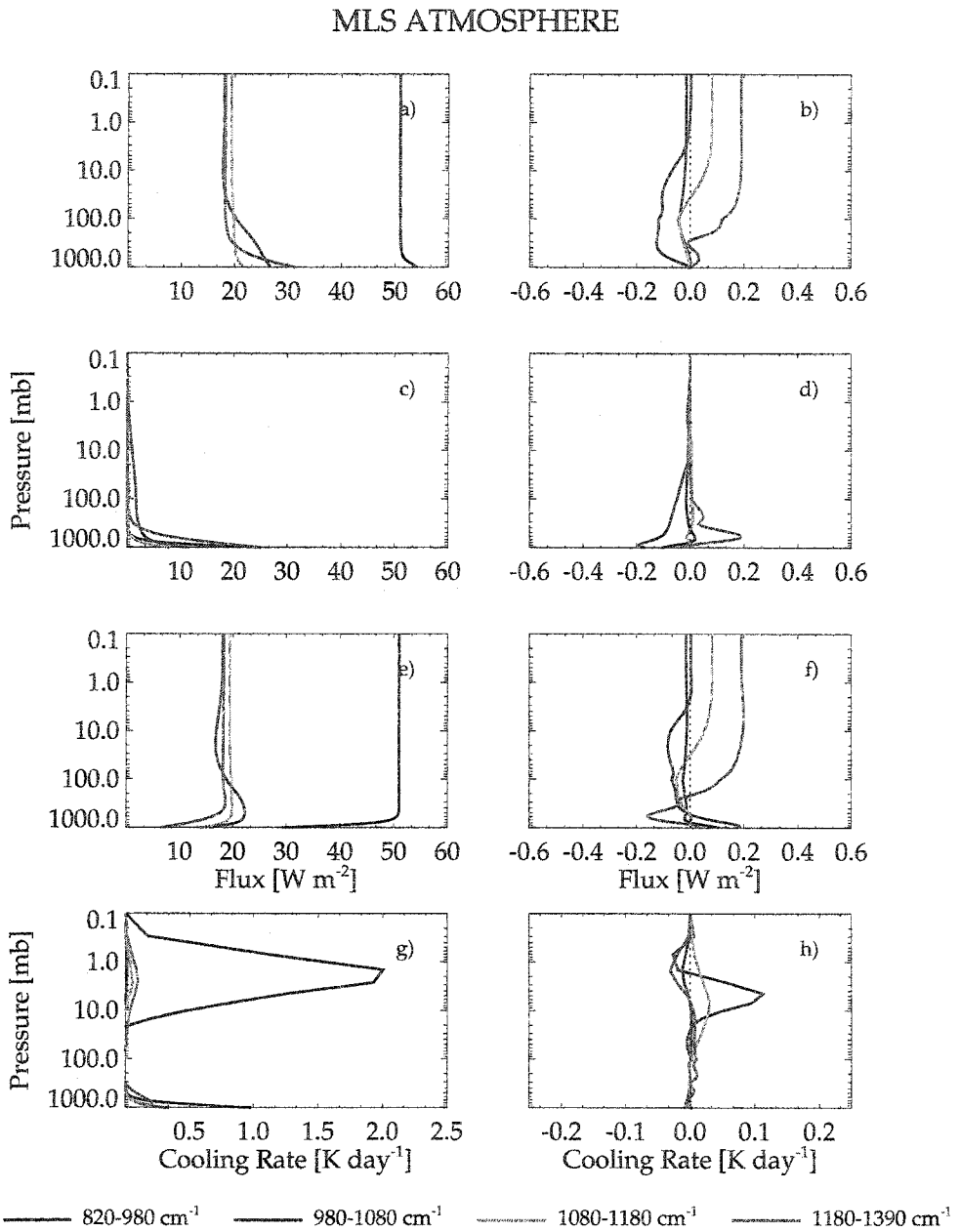

Figure 4.6. RRTM band 6-9 vertical profile flux residuals for MLS atmosphere. Spectrally integrated (a) up, (c) down, (e) net fluxes, and (g) cooling rates for band 6-9 calculated by LBLRTM for the mid-latitude summer (MLS) atmospheres. Difference between RRTM and LBLRTM for the quantities are shown in panel (b), (d), (f), and (h), respectively. All quantities are plotted as a logarithmic function of pressure.

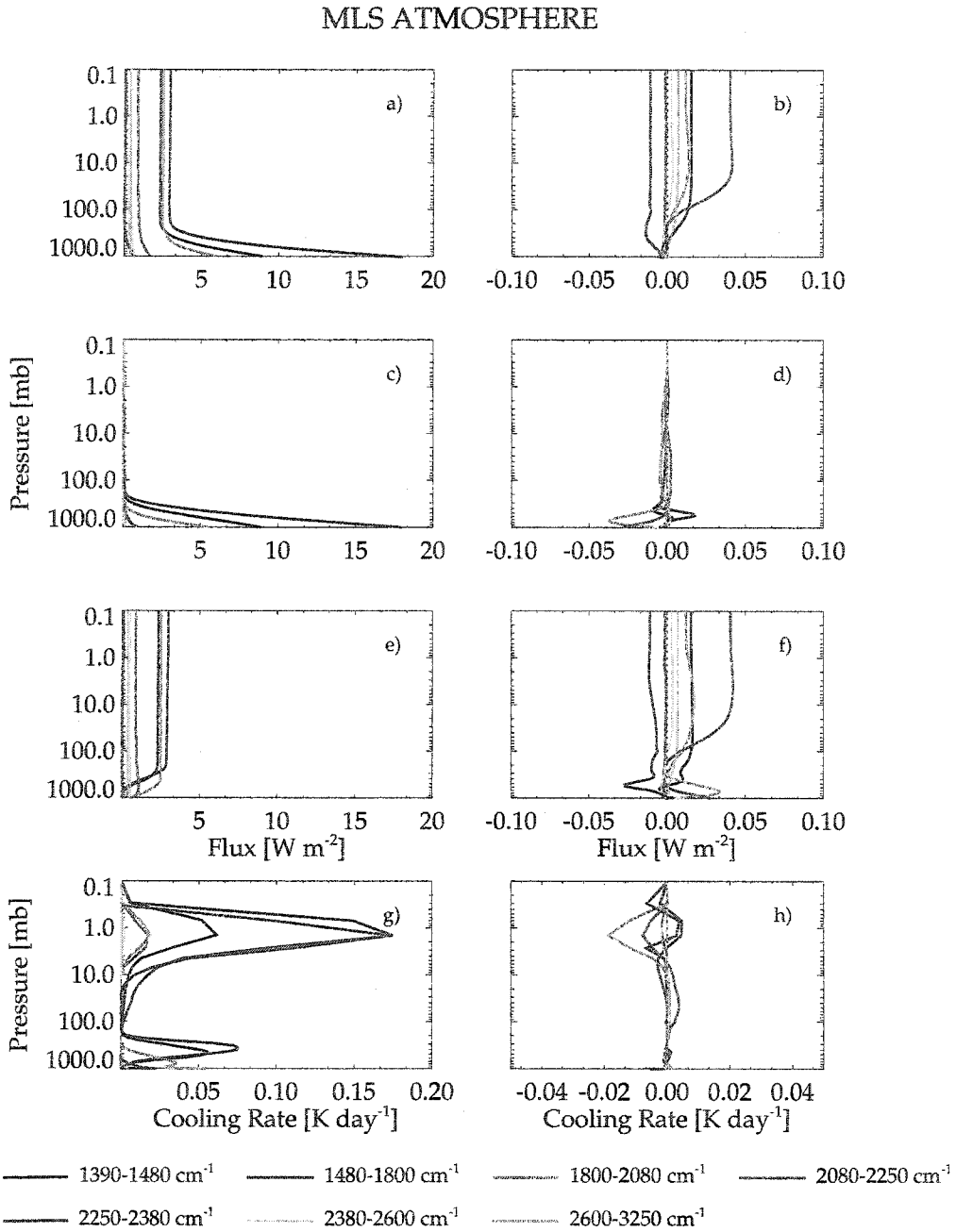

Figure 4.7. RRTM band 10-16 vertical profile flux residuals for MLS atmosphere. Spectrally integrated (a) up, (c) down, (e) net fluxes, and (g) cooling rates for band 10-16 calculated by LBLRTM for the mid-latitude summer (MLS) atmospheres. Difference between RRTM and LBLRTM for the quantities are shown in panel (b), (d), (f), and (h), respectively. All quantities are plotted as a logarithmic function of pressure.

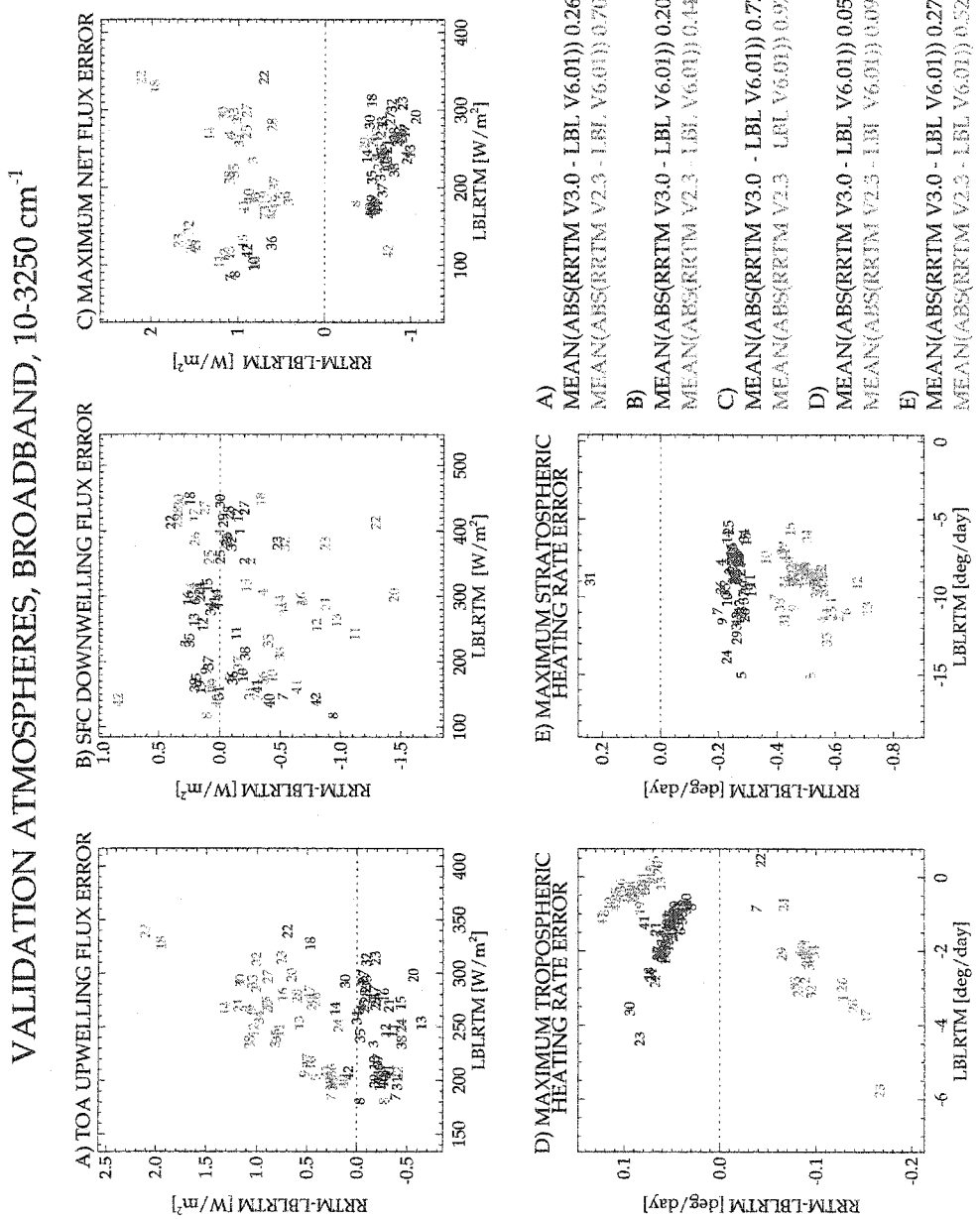

Figure 4.8. [Broadband RRTM - LBLRTM residuals for *Garand et al.* [2001] atmospheres. Broadband (10-3250 cm^{-1}) differences between RRTM and LBLRTM for 42 atmospheric profiles for a) upward flux at the top of the atmosphere, b) downward flux at the surface, and the maximum residual in c) net flux, d) tropospheric cooling rate, and e) stratospheric cooling rate plotted as a logarithmic function of pressure.

4.2.2 *Garand et al.* [2001] Atmospheres

The diverse set of atmospheres compiled for the *Garand et al.* [2001] study have been extremely useful in evaluating the performance of RRTM v3.0 not only against LBLRTM but also against RRTM v2.3. Figure 4.8 shows the broadband flux and cooling rate residuals for the 42 atmospheric profiles. Residual quantities plotted are the upward flux at the top of the atmosphere, the downward flux at the surface, the maximum net flux discrepancy at any altitude, and the maximum tropospheric and stratospheric cooling rate discrepancy. The mean of the absolute value of the profile residuals are also quantified on the bottom, right panel of each figure. RRTM v3.0 agrees with LBLRTM to within 1.0 W m^{-2} at all levels for 42 different atmospheres; the computed cooling rates agree to within 0.1 K day^{-1} in the troposphere and 0.3 K day^{-1} in the stratosphere. The RRTM v2.3 residuals exceed those of RRTM v3.0 for all the mean quantities. This is due, in part, to improvements in the algorithms, but also to the fact that RRTM v2.3 was constructed from an older version and line parameter database than RRTM v3.0.

Appendix A shows the band-by-band residuals in a format identical to that in Figure 4.8. This plots show the contribution of each band to the broadband calculations.

The following text and figures highlight the band-by-band differences between the two versions of the model.

Improvement in Stratospheric Cooling Rates

Stratospheric radiative cooling plays an important role in the dynamics of the upper atmosphere. The bulk of the radiative cooling can be attributed to the ν_2 carbon dioxide band (580-750 cm^{-1}) and the strong ν_3 band of ozone (980-1080 cm^{-1}) [*Clough and Iacono*, 1995]. Two spectral bands in RRTM contain the bulk of this cooling, band 4 (630-700 cm^{-1}) and band 7 (980-1080 cm^{-1}). In RRTM v2.3 the broadband cooling rate discrepancy for the MLS atmosphere exceeded 0.5 K day^{-1} relative to the version of LBLRTM and the line parameter database from which it was built. The discrepancy was attributed to RRTM calculating downward fluxes that were too large relative to LBLRTM.

These cooling rate discrepancies were of concern to the climate modeling community, so a goal of RRTM v3.0 was to improve these residuals. When RRTM v3.0 was first con-

structed, the new methodology of RRTM was not sufficient to reduce the cooling rate discrepancies, so an empirical method was employed. *Mlawer et al.* [1997] showed that the cooling rates for band 4 calculations are sensitive to the spacing and number of intervals used in g space, and that for the upper atmosphere the dominant region of the k distribution contributing to the peak of the cooling is for g values from 0.796 to 0.989. Simple empirical scaling factors were applied to the optical depths for these important g values. Of course altering the optical depths will affect both the upward and downward fluxes. Therefore, these particular factors, chosen to improve the downward flux but to minimize the change in upward flux residuals, resulted in improved cooling rates. The mean band 4 stratospheric cooling rate residual was reduced from 0.431 in RRTM v2.3 to 0.129 in RRTM v3.0 for the 42 validation atmospheres; the mean band 7 stratospheric cooling rate were similarly reduced from 0.129 to 0.076. Figure A.5 and Figure A.8 illustrate the improved cooling rates from RRTM v2.3 to RRTM v3.0 for each validation atmosphere.

Note that FLRTT did not generate these empirical factors, since FLRTT was primarily designed for model generation for satellite simulations. This ability to improve stratospheric cooling rates will be added in the next generation of FLRTT.

4.2.3 Trace Gas Sensitivity

Tropospheric water vapor impacts radiative flux throughout the entire longwave spectral region, making it of primary importance in longwave calculations [*Clough et al.*, 1992]. However, the absorption bands of other trace species, such as CO_2, CH_4, and N_2O, strongly influence particular spectral domains. These trace species are particularly important in the context of climate change studies. Atmospheric concentrations of carbon dioxide have increased by 30%, methane concentrations doubled, and nitrous oxide concentrations have increased by 15% since the start of the industrial revolution (http://www.epa.gov). It is important to assess the ability of RRTM to calculate accurate fluxes in scenarios in which these important greenhouse gases are varied substantially from their current values. A goal successfully achieved in RRTM v3.0 was to improve the calculation of fluxes and cooling rates in climate change predictions. The following subsections present comparisons of the flux change from the mid-latitude summer atmosphere to an increase in a given species, calculated by LBLRTM, RRTM v3.0, and RRTM v2.3.

Increasing CO_2

The results of two comparisons are shown in this section: doubling CO_2 from its current value of 360 ppmv to 720 ppmv, and increasing CO_2 one hundred times to 36000 ppmv. Table 4.2 presents flux differences (i.e. (Double CO2 - Normal CO2)) for the surface, tropopause (100 mbar), and the top of the atmosphere for doubling CO_2. Discrepancies in the broadband net flux for RRTM v2.3 and RRTM v3.0 do not exceed 8% at any altitude, and the discrepancies in stratospheric cooling rate do not exceed 16%. It is clear that RRTM v2.3 captures the upward flux sensitivity to doubling CO_2 slightly better than RRTM v3.0. Table 4.2 demonstrates that RRTM v2.3 benefits more from cancellation of errors in upward flux from the individual bands than does RRTM v3.0.

Table 4.3 illustrate the performance of RRTM when the CO_2 is increased dramatically to 100 times the current level. This table is formatted identically to the double CO_2 set. Discrepancies in broadband net flux and stratospheric cooling rates for RRTM v3.0 do not exceed 5% at any altitude, but the discrepancies for RRTM v2.3 are extremely large. The RRTM v2.3 residuals are primarily due to differences in the 500-630 cm^{-1} band, which may be attributed to the abnormal behavior in the original *Mlawer et al.* [1997] binary-species method.

There is an additional issue revealed in this intercomparison regarding the treatment of the CO_2 in the longwave atmospheric window (bands 6-8, 820-1180 cm^{-1}). In this spectral region CO_2 is characterized as a minor species (that is, the calculation of the CO_2 optical depth is treated less rigorously than if it were considered a key species). When the values of CO_2 are pushed well past their standard MLS values the minor-species assumption will break down since it would likely have the radiative impact of a key species. In bands in which CO_2 is treated as a minor species RRTM v3.0 scales the column abundance of CO_2 to bring the fluxes in check with LBLRTM. The scale factor was empirically derived for each band by computing the LBLRTM fluxes at several values of CO_2, and computing a scale factor as a function of mixing ratio to bring RRTM v3.0 to LBLRTM. This same technique was applied to bands in which climate-sensitive trace gases are treated as minor species. Note that this scale factor was not generated by FLRTT, but future versions of FLRTT may have this capability.

Doubling CH_4 and Doubling N_2O

Methane and nitrous oxide are the most radiatively important trace gases following water vapor, carbon dioxide, and ozone *Clough et al.* [1992]. CH_4 is most significant in the 1180-1390 cm^{-1} (band 9), but also absorbs in the 2600-3250 cm^{-1} (band 16). The difference in fluxes and cooling rates resulting from doubling the CH_4 mixing ratio from its current MLS level (see Figure 4.1) calculated by LBLRTM and RRTM are illustrated in Table 4.2.3. RRTM v3.0 has improved sensitivity to changes in CH_4 relative to RRTM v2.3, and captures the net flux difference to just over 10% of LBLRTM.

Similar results occur for N_2O doubling, and are illustrated in Table 4.2.3. Again it is important to reiterate that an empirical scaling factor is applied to N_2O and CH_4 when they are treated as minor species in RRTM v3.0.

Table 4.2. Effects on fluxes due to doubling CO_2 mixing ratio from current levels. Effects on fluxes [W m^{-2}] due to doubling CO_2 from current levels (360 ppmv) at the surface, tropopause, and TOA.

Band	Wavenumber	SURFACE NET FLUX			TROPOPAUSE UP FLUX			TROPOPAUSE DOWN FLUX			TROPOPAUSE NET FLUX			TOA NET FLUX		
	cm-1	LBL	R v3.0	R v2.3	LBL	R v3.0	R v2.3	LBL	R v3.0	R v2.3	LBL	R v3.0	R v2.3	LBL	R v3.0	R v2.3
3	500-630	-0.05	-0.02	-0.03	-1.21	-1.18	-1.08	0.49	0.50	0.51	-1.70	-1.68	-1.60	-1.11	-1.09	-1.03
4	630-700	-0.02	-0.02	-0.02	-0.20	-0.20	-0.19	0.73	0.76	0.77	-0.93	-0.96	-0.95	0.58	0.61	0.59
5	700-820	-0.90	-1.00	-0.90	-1.94	-2.10	-2.02	0.47	0.42	0.40	-2.41	-2.51	-2.43	-1.73	-1.92	-1.87
6	820-980	-0.34	-0.35	-0.28	-0.19	-0.24	-0.23	0.01	0.00	0.00	-0.19	-0.24	-0.23	-0.19	-0.24	-0.23
7	980-1080	-0.33	-0.37	-0.30	-0.16	-0.13	-0.13	0.00	0.01	0.00	-0.16	-0.14	-0.14	-0.13	-0.08	-0.09
8	1080-1180	-0.10	-0.12	-0.07	-0.05	-0.07	-0.04	0.00	0.00	0.00	-0.05	-0.07	-0.05	-0.05	-0.07	-0.04
9	1180-1390	0.00	0.00	0.00	-0.02	0.00	0.00	0.00	0.00	0.00	-0.02	0.00	0.00	-0.02	0.00	0.00
12	1800-2080	-0.02	-0.01	0.00	-0.05	-0.05	-0.03	0.00	0.00	0.00	-0.05	-0.05	-0.03	-0.05	-0.05	-0.03
13	2080-2250	-0.02	-0.03	0.00	-0.02	-0.04	0.00	0.00	0.00	0.00	-0.02	-0.04	0.00	-0.02	-0.03	0.00
14	2250-2380	0.00	0.00	0.00	0.00	0.00	0.00	0.00	0.00	0.00	0.00	0.00	0.00	0.01	0.01	0.01
15	2380-2600	-0.02	-0.01	-0.07	-0.02	-0.02	-0.07	0.00	0.00	0.00	-0.02	-0.02	-0.07	-0.02	-0.02	-0.07
Total	10-3250	-1.81	-1.93	-1.67	-3.85	-4.02	-3.80	1.70	1.69	1.69	-5.55	-5.70	-5.48	-2.72	-2.88	-2.76

Table 4.3. Effects on fluxes due to increasing CO_2 by 100 times from its current level. Effects on fluxes [W m^{-2}] due to increasing CO_2 100 times from current levels (360 ppmv) at the surface, tropopause, and TOA.

Band	Wavenumber	SURFACE NET FLUX			TROPOPAUSE UP FLUX			TROPOPAUSE DOWN FLUX			TROPOPAUSE NET FLUX			TOA NET FLUX		
	cm-1	LBL	R v3.0	R v2.3	LBL	R v3.0	R v2.3	LBL	R v3.0	R v2.3	LBL	R v3.0	R v2.3	LBL	R v3.0	R v2.3
1	10-350	0.00	0.00	0.00	0.00	0.01	0.00	-0.01	-0.02	0.00	0.01	0.02	0.00	0.00	0.01	0.00
2	350-500	0.00	0.00	0.00	-0.03	0.00	0.00	0.01	0.00	0.00	-0.03	0.00	0.00	-0.03	0.00	0.00
3	500-630	-0.24	-0.18	-0.23	-8.01	-7.68	35.47	5.59	5.80	6.08	-13.59	-13.47	29.39	-5.76	-5.57	35.03
4	630-700	-0.05	-0.05	-0.05	-0.32	-0.28	-0.27	1.50	1.50	1.51	-1.82	-1.78	-1.77	5.99	6.02	5.97
5	700-820	-6.60	-6.66	-6.62	-12.90	-13.30	-13.94	4.51	4.40	4.48	-17.42	-17.70	-18.41	-9.97	-10.45	-11.20
6	820-980	-8.98	-8.17	-12.78	-5.52	-6.10	-10.91	0.20	0.00	0.00	-5.71	-6.10	-10.91	-5.57	-6.10	-10.91
7	980-1080	-6.75	-7.82	-10.58	-3.56	-3.47	-6.47	0.09	0.17	0.34	-3.65	-3.65	-6.81	-2.84	-2.50	-4.92
8	1080-1180	-2.10	-2.03	-4.30	-1.24	-1.21	-2.91	0.03	0.03	0.04	-1.27	-1.24	-2.95	-1.20	-1.25	-2.81
9	1180-1390	-0.29	0.00	0.00	-0.92	0.00	0.00	0.07	0.00	0.00	-0.99	0.00	0.00	-0.94	0.00	0.00
12	1800-2080	-0.23	-0.21	-0.13	-0.65	-0.67	-0.78	0.02	0.00	0.00	-0.66	-0.67	-0.78	-0.64	-0.67	-0.78
13	2080-2250	-0.33	-0.32	0.00	-0.39	-0.44	0.00	0.01	0.00	0.00	-0.40	-0.44	0.00	-0.34	-0.42	0.00
14	2250-2380	-0.01	-0.01	-0.01	-0.01	0.00	0.00	0.00	0.00	0.00	-0.01	-0.01	-0.01	0.10	0.10	0.10
15	2380-2600	-0.22	-0.23	-0.46	-0.23	-0.24	-0.46	0.00	0.00	0.00	-0.23	-0.24	-0.46	-0.22	-0.24	-0.46
Total	10-3250	-25.80	-25.67	-35.16	-33.78	-33.39	-0.26	12.01	11.88	12.44	-45.79	-45.27	-12.71	-21.45	-21.05	10.02

Table 4.4. Effects on fluxes due to doubling CH_4 from its current level. Effects on fluxes [W m^{-2}] due to doubling CH_4 from current levels at the surface, tropopause, and TOA.

Band	Wavenumber	SURFACE NET FLUX			TROPOPAUSE UP FLUX			TROPOPAUSE DOWN FLUX			TROPOPAUSE NET FLUX			TOA NET FLUX		
	cm-1	LBL	R v3.0	R v2.3	LBL	R v3.0	R v2.3	LBL	R v3.0	R v2.3	LBL	R v3.0	R v2.3	LBL	R v3.0	R v2.3
8	1080-1180	-0.01	0.00	0.00	-0.01	0.00	0.00	0.00	0.00	0.00	-0.01	0.00	0.00	-0.01	0.00	0.00
9	1180-1390	-0.29	-0.27	-0.23	-0.70	-0.64	-0.35	0.05	0.06	0.09	-0.75	-0.70	-0.44	-0.69	-0.63	-0.37
16	2600-3250	-0.01	0.00	-0.01	-0.01	-0.01	-0.01	0.00	0.00	0.00	-0.01	-0.01	-0.01	-0.01	-0.01	-0.01
Total	10-3250	-0.30	-0.27	-0.24	-0.73	-0.65	-0.36	0.05	0.06	0.09	-0.78	-0.71	-0.45	-0.72	-0.63	-0.38

Table 4.5. Effects on fluxes due to doubling N_2O from its current level. Effects on fluxes [W m^{-2}] due to doubling N_2O from current levels at the surface, tropopause, and TOA

Band	Wavenumber	SURFACE NET FLUX			TROPOPAUSE UP FLUX			TROPOPAUSE DOWN FLUX			TROPOPAUSE NET FLUX			TOA NET FLUX		
	cm-1	LBL	R v3.0	R v2.3	LBL	R v3.0	R v2.3	LBL	R v3.0	R v2.3	LBL	R v3.0	R v2.3	LBL	R v3.0	R v2.3
3	500-630	0.00	0.00	0.00	-0.24	-0.24	-0.37	0.08	0.05	0.07	-0.32	-0.29	-0.44	-0.24	-0.24	-0.37
8	1080-1180	-0.13	-0.14	-0.12	-0.15	-0.18	-0.16	0.01	0.01	0.01	-0.15	-0.19	-0.16	-0.16	-0.19	-0.16
9	1180-1390	-0.19	-0.17	-0.22	-0.54	-0.61	-0.90	0.03	0.03	0.00	-0.57	-0.64	-0.90	-0.55	-0.61	-0.88
13	2080-2250	-0.06	-0.06	-0.10	-0.06	-0.06	-0.13	0.00	0.00	0.00	-0.06	-0.06	-0.13	-0.06	-0.06	-0.13
15	2380-2600	-0.01	-0.01	-0.01	-0.01	-0.01	-0.01	0.00	0.00	0.00	-0.01	-0.01	-0.01	-0.01	-0.01	-0.01
Total	10-3250	-0.38	-0.38	-0.44	-1.00	-1.10	-1.55	0.12	0.08	0.08	-1.12	-1.19	-1.63	-1.02	-1.11	-1.55

Chapter 5

Clear-Sky Longwave Radiative Transfer in the Arctic

The principal objective of this thesis chapter is to compare observations of downward longwave radiances and fluxes during clear-sky conditions to those calculated by a line-by-line and rapid radiative transfer model. This work simultaneously addresses the specification of the clear-sky atmospheric state, radiometric measurements, and radiative transfer modeling through a detailed closure analysis. An important component of this intercomparison is the examination of the radiative fields from both a broadband and spectral perspective. Comparing observed and modeled radiances within specific spectral intervals reveals whether or not specific physical processes are correctly represented in either the models or the specification of the atmospheric state. Figure 5.1 illustrates the closure process. The details of the model calculations, observations, and accompanying uncertainties are discussed throughout this chapter.

This closure analysis closely parallels the Atmospheric Emitted Radiance Interferometer and line-by-line radiative transfer model (AERI/LBLRTM) Quality Measurement Experiment and the Broadband Quality Measurement Experiments (QMEs) underway at the ARM Southern Great Plains Cloud and Radiation Testbed (SGP CART) site [*Clough et al.*, 2000; *Revercomb et al.*, 2002], the AERI-ER/LBLRTM intercomparison for the Surface Heat Budget of the Arctic Ocean Project (SHEBA) [*Tobin et al.*, 2000], and the First and Second International Pyrgeometer and Absolute Sky-scanning Radiometer Comparison (IPASRC-

I and IPASRC-II) [*Philipona et al.*, 2001; *Marty et al.*, 2003]. The QMEs and IPASRCs have been critical in the identification of a number of issues, such as a dry bias in the radiosonde relative humidity measurements, AERI and PIR calibration issues.

5.1 Background

The importance of the arctic region in the study of global climate change has been increasingly recognized over the last decade [*IPCC*, 1997]. Modeling studies predict that the polar latitudes are likely to respond to global temperature changes earlier than other climatic regions. Such changes in the arctic will impact global climate by modifying ocean circulations and radiative energy transport.

As discussed by *Stamnes et al.* [1999], the Department of Energy Atmospheric Radiation Program (ARM) established a high-latitude measurement site to elucidate the physical processes which are important in the arctic climate system and to provide a long-term data set from which general circulation models can be validated. The North Slope of Alaska/Adjacent Arctic Ocean Cloud and Radiation Testbed (NSA CART) site, Figure 5.2, is centered at Barrow, Alaska (N 71° 19.378';W 156° 36.934'). The NSA CART site is characterized by extremely cold temperatures and low water vapor amounts. At 70°N, *Serreze et al.* [1995] reported the zonal, monthly mean column-integrated precipitable water vapor to range from 2.9 mm in February to 16.2 mm in July. Very strong and persistent temperature inversions are present throughout much of the year due to the absence of sunlight.

The NSA CART site is equipped with a suite of instrumentation that greatly enhances intercomparisons between observations and model calculations of atmospheric radiation. Such intercomparisons are an important tool in the evaluation of atmospheric fluxes calculated by general circulation models (GCMs). In particular, an Extended-Range Atmospheric Emitted Radiance Interferometer (AERI-ER) is deployed at the NSA CART site. The AERI-ER, developed at the University of Wisconsin with the support of the ARM Program, measures downward longwave radiance from 400 to 3000 cm^{-1} with a spectral resolution of 0.482 cm^{-1}, outputting a sky radiance spectrum every 8 minutes. Typical winter time radiance spectra observed by the AERI-ER channel 1 and AERI-ER channel 2 are shown in the top panels of Figure 5.3 and Figure 5.4, with the estimated calibration

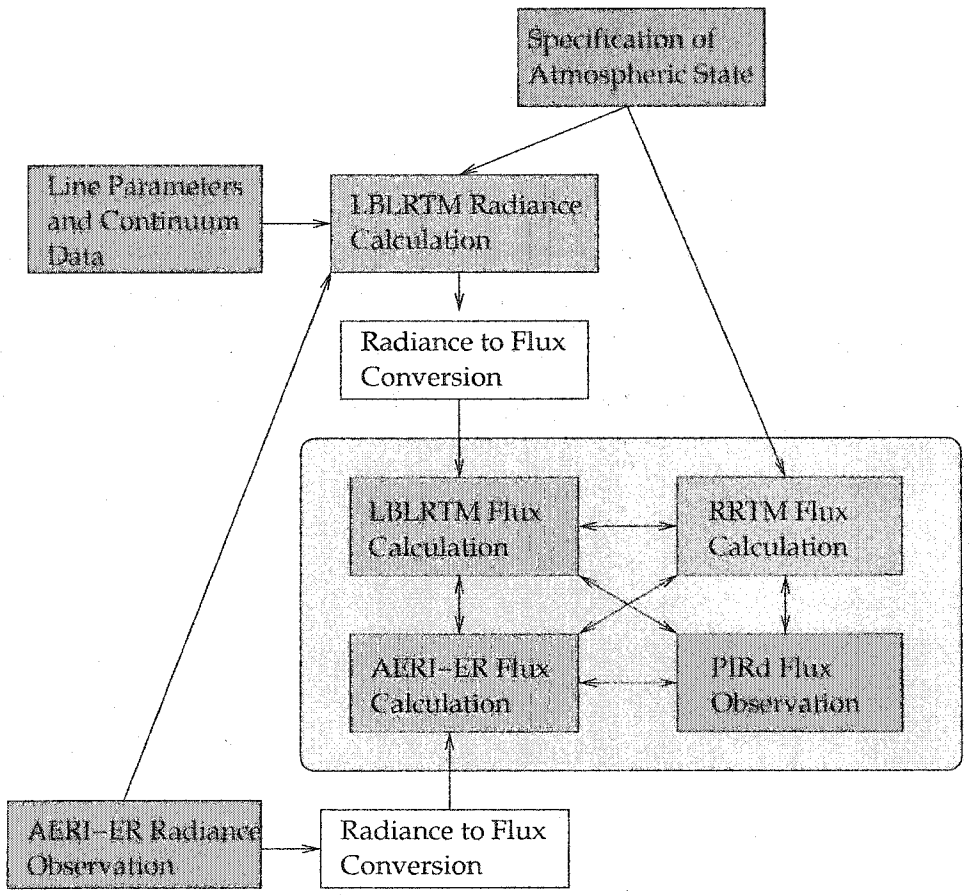

Figure 5.1. Flow diagram for radiance and flux closure analysis at NSA CART site. Flow diagram for radiative transfer model and observation closure analysis, which utilizes the AERI-ER, the PIRd, LBLRTM, and RRTM. The specification of the atmospheric state, radiometric measurements, and radiative transfer modeling are simultaneously assessed through such closure analysis.

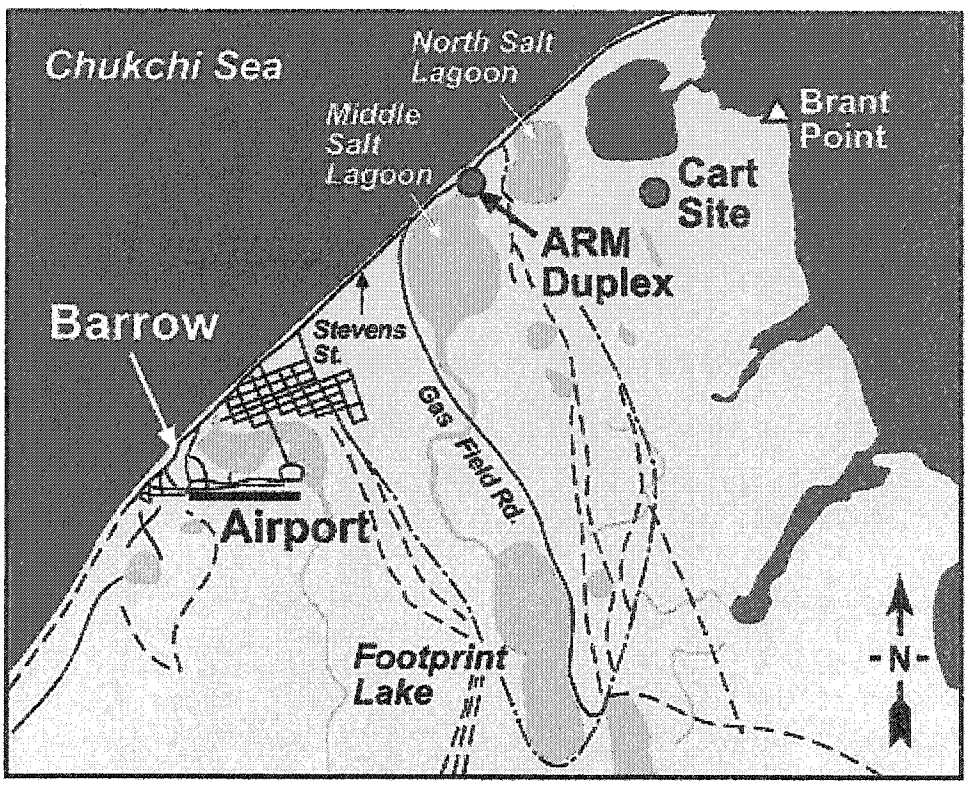

Figure 5.2. Map of the ARM NSA CART site. The NSA CART site is centered at Barrow, Alaska. Data from the NSA CART site provides important information about cloud and radiation processes at high latitudes [*Stamnes et al.*, 1999]

.

uncertainty in the observation shown in the bottom panels.

A desirable feature of ground-based AERI-ER is that it views a portion of the strong purely rotational band of water vapor between 0 and 1000 cm^{-1}. In the cold, dry arctic climate there are numerous arctic microwindows, regions between spectral line centers which become transparent in the water vapor rotational band. *Tobin et al.* [1999] have succinctly summarized the multitude of reasons why this spectral region is important for clear-sky radiative transfer studies: (1) when the arctic microwindows become transparent their impact on longwave cooling to space increases [*Clough et al.*, 1992; *Stamnes et al.*, 1999]; (2) the surface conditions of the arctic are often similar to those at high altitudes; therefore, knowledge gained from ground-based observations of this spectral region will improve high-altitude modeling capability [*Stamnes et al.*, 1999]; and (3) measurements in this spec-

tral region are useful for comparisons to theoretical studies of H_2O-X collisions and spectral lineshapes, which are critically important in radiative transfer modeling [*Rosenkranz*, 1987; *Clough et al.*, 1992].

To complement the high-resolution spectral measurements Eppley Laboratory, Inc. pyrgeometers (PIRs) are operational at the NSA CART site. Pyrgeometers are the most widely used instruments for measuring atmospheric broadband longwave fluxes for meteorological and climatological networks [*Philipona et al.*, 2001]. They have proven to operate reliably in harsh weather conditions, and their relatively low cost is an additional benefit.

5.2 Description of North Slope of Alaska Cloud and Radiation Testbed Site Radiance and Flux Analysis Components

5.2.1 Physical Configuration of the NSA CART Site

The instruments at the NSA CART site are located within or above the the Portable Arctic Atmospheric Radiation and Cloud Station shelter (also known as the Great White) shown in Figure 5.5. The base of the Great White pilons is approximately 8 m above sea level; the top of the Great White is 13 m above sea level. Located roughly 150 m from the Great White is a 40 m meteorological tower.

Note that all altitudes in the remaining text are presented relative to the surface.

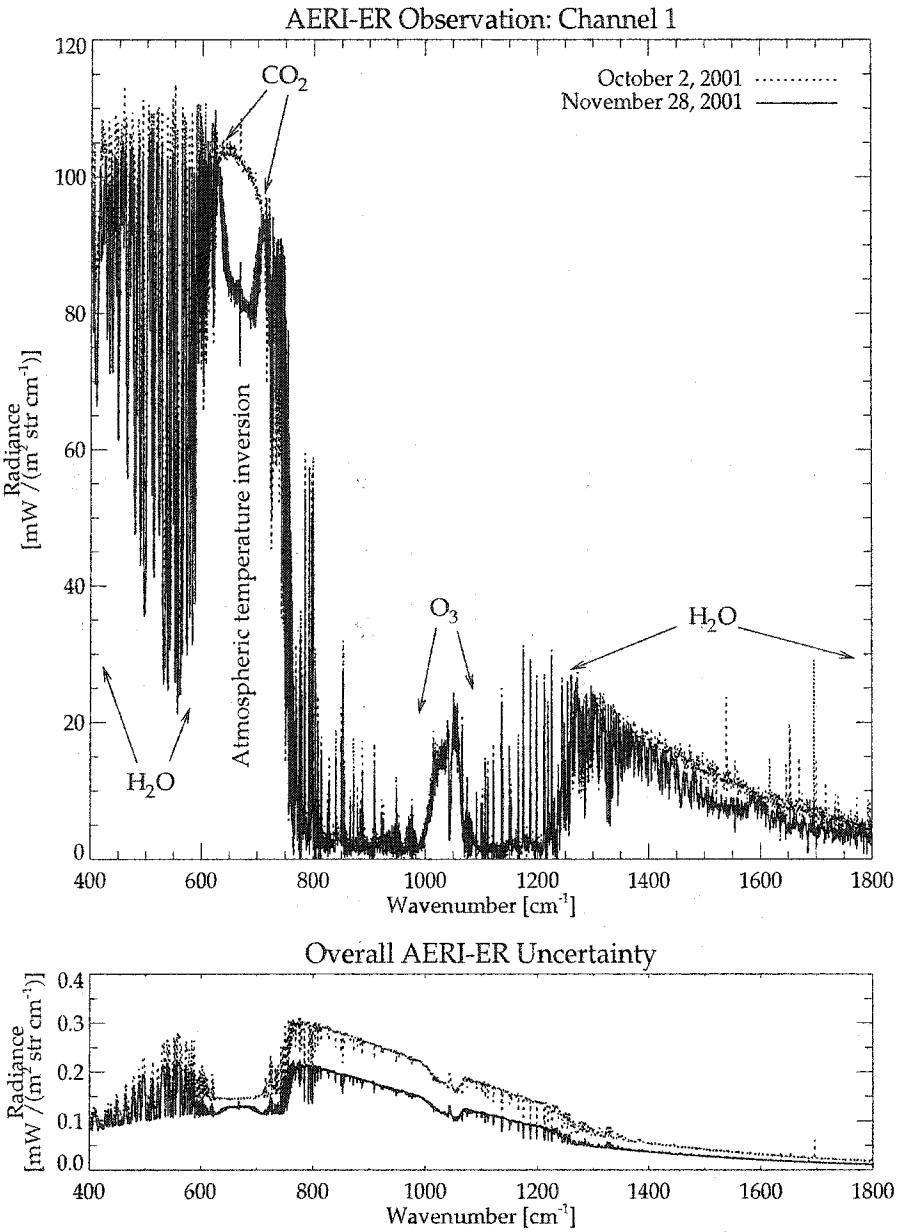

Figure 5.3. AERI-ER channel 1 observations of longwave radiances and corresponding calibration uncertainties. AERI-ER channel 1 observation of longwave radiance (top panel) and corresponding calibration uncertainties (bottom panel) for two winter atmospheres [October 2, 2001 (dotted lines) and November 28, 2001 (solid lines)] at the NSA CART site. The spectral coverage of the AERI-ER includes a significant portion of water vapor rotation band (0 to 1000 cm^{-1}), which plays an important role in near-surface radiative cooling at high latitudes [*Stamnes et al.*, 1999].

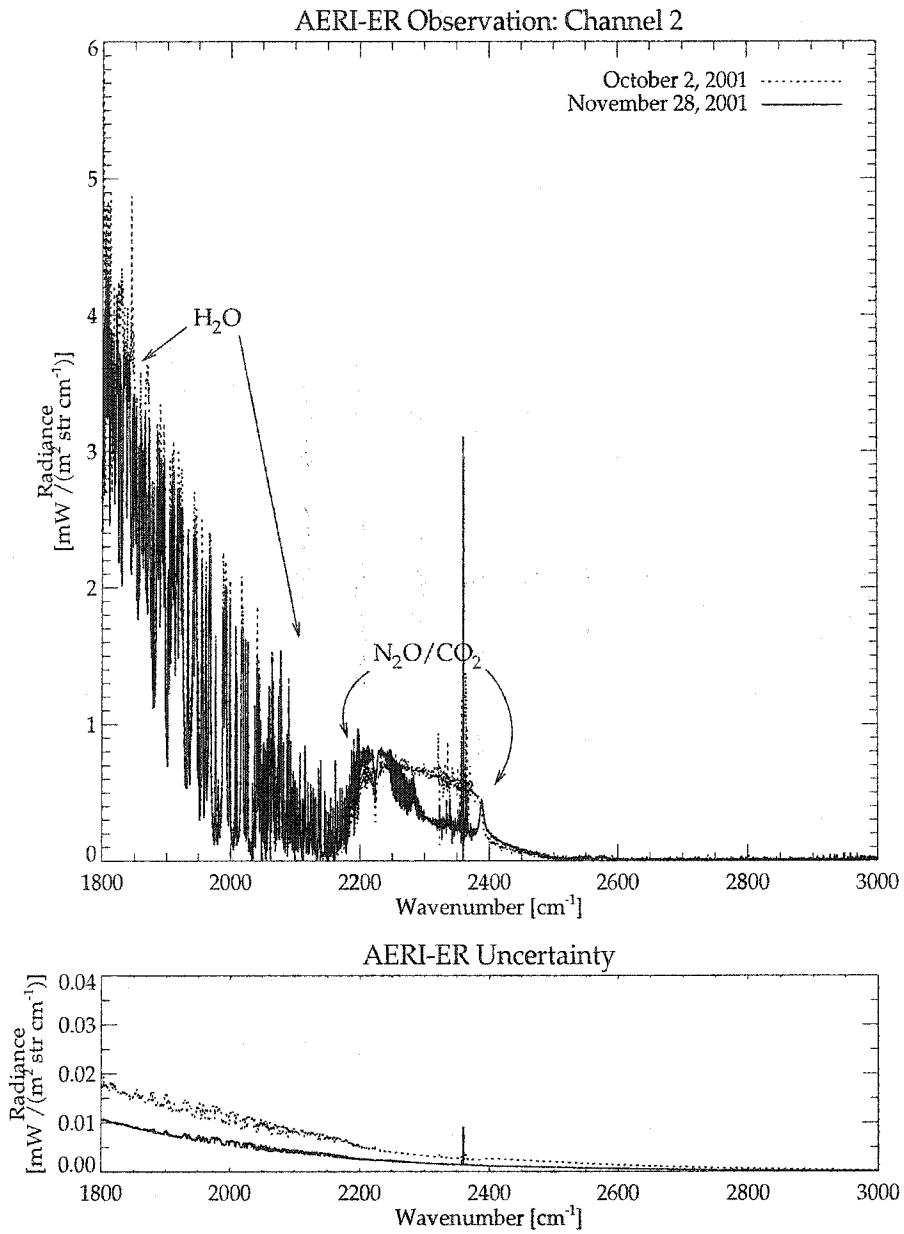

Figure 5.4. AERI-ER channel 2 observations of longwave radiances and corresponding calibration uncertainties. AERI-ER channel 2 observations of longwave radiance (top panel) and corresponding calibration uncertainties (bottom panel) for two winter atmospheres [October 2, 2001 (dotted lines) and November 28, 2001 (solid lines)] at the NSA CART site.

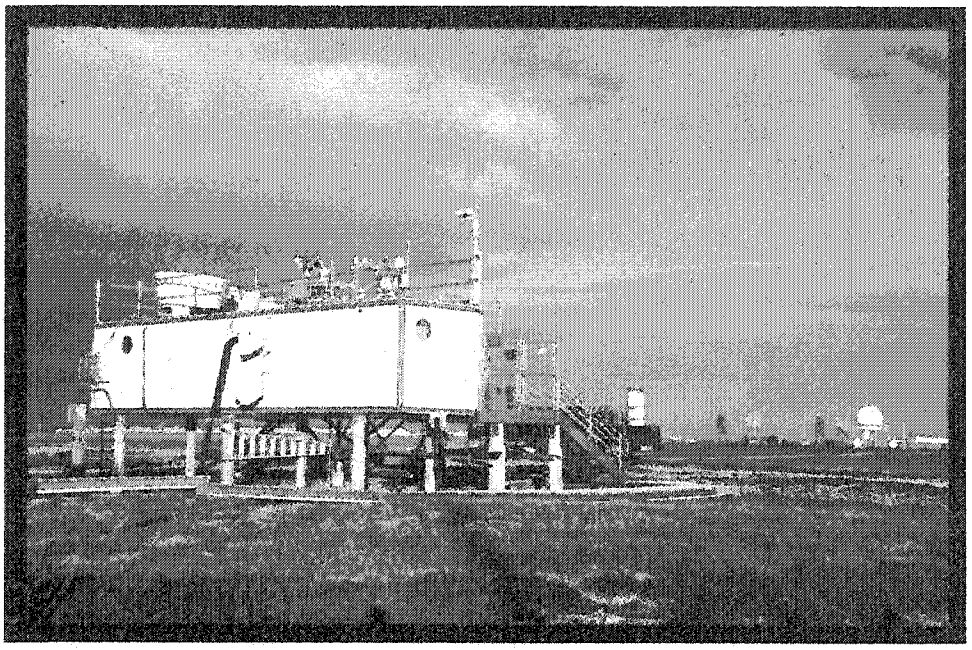

Figure 5.5. NSA CART site Portable Arctic Atmospheric Radiation and Cloud Station shelter. The NSA CART site Portable Arctic Radiation and Cloud Station shelter, also known as the Great White, is located on the tundra just to the south of Pt. Barrow, Alaska. This shelter houses the AERI-ER and other instrument hardware. Additional instruments, such as the PIRs, are installed on the platform above the shelter. Imaged obtained from the internet site http://www.arm.gov.

5.2.2 Specification of the Atmospheric State

A number of instruments are available at the NSA CART site to characterize the thermodynamic and gaseous profile of the atmosphere, as well as to identify the presence of clouds. These data are required for radiative transfer calculations.

Radiosonde Measurements of Pressure, Temperature, and Relative Humidity

A radiosonde is a balloon-borne instrument package which provides in-situ measurements (vertical profiles) of the thermodynamic state of the atmosphere. Primary quantities measured are pressure, temperature, relative humidity; secondary derived quantities are altitude, dew point, ascent rate, and latitude/longitude of the flying radiosonde. The radiosondes flown at the NSA CART site in 2001 were Vaisala RS80-15H, which transmit

their data to a fixed groundstation. The manufacturer's specifications for the thermodynamic sensor resolution and precision, respectively, are: 0.1 hPa and 0.5 hPa for the pressure sensor, 0.1 degrees and 0.2 degrees for the temperature sensor, and 1% and 3% for the relative humidity sensor.

Measurements collected by the radiosonde may be influenced by a number of factors, including humidity sensor saturation or sensor icing. Additionally, RS-80 Vaisala radiosondes can exhibit a dry-bias in the relative humidity measurements [*Wang et al.*, 2002]. The dry bias is due to contamination of the polymer used in the capacitive relative humidity sensor; the magnitude of the bias is a function of the age of the sensor and the measured relative humidity, but is of the order of 8% at 80% relative humidity after 1.5 years [*Miller et al.*, 1999]. *Wang et al.* [2002] conducted a series of laboratory tests to develop methods to correct several humidity measurement errors, which include the chemical contamination error. The correction methods (hereafter referred to as the Vaisala correction) were applied to 8129 Vaisala RS80 soundings from the Tropical Ocean and Global Atmosphere Coupled Ocean-Atmosphere Experiment (TOGA COARE), and improvement was demonstrated in the accuracy of the radiosonde data set.

Radiosonde measurements for the NSA CART site can be obtained from the ARM data archive. There are two types of radiosonde files available at the ARM data archive: the raw data, and 10-second data. For this study, 10-second data was used, where the 10-seconds refers to the fact that each vertical sample in the file is calculated from a 10-second window surrounding the raw data (sampled at approximately 1.5 seconds). Additionally the 10-second data at the ARM archive is in "a1" format. The a1 flag indicates that the data has been converted only to the standard ARM data format (netCDF); no other processing has been performed. To use the soundings in radiative transfer calculations the a1 sounding data was further processed to: (a) remove all bad data points, indicated by -999 in the raw data, (b) remove all data points between the initialization time of the radiosonde and the actual launch time, and (c) remove all data points in which the radiosonde reversed direction from ascent to descent (since most radiative transfer models require input profiles in ascending-by-altitude order only).

The Barrow Meteorology Station

The Barrow Meteorology Station (BMET) consists of in-situ air temperature, relative humidity, wind speed, and wind direction sensors mounted on a tower at 2, 10, 20, and 40 m above the surface. The air temperature and relative humidity sensors are located on the same probe, and enclosed in a aspirated radiation shield to minimize radiation and icing errors. The tower is located roughly 150 m from the Great White. Barometric pressure is also measured, but the sensor is located at the Great White rather than at the tower location. The BMET is not a calibrated system, but each sensor and the sensor's data collector are calibrated individually in the field against calibrated references. A field calibration check on the instruments were made on September 18, 1999 and October 13, 2001. All instruments were within manufacturer-specified tolerances.

Microwave Radiometer

The column-integrated precipitable water vapor (PWV) and cloud liquid water are routinely retrieved from the standard ARM dual-channel microwave radiometer (MWR) at the NSA CART site. The MWR was built by Radiometrics Corporation in Boulder, Colorado, and operates at 23.8 and 31.4 GHz. It is identical to the MWR deployed at the ARM SGP CART site and for SHEBA [*Liljegren*, 2000a].

The PWV has been an extremely useful product in characterizing the atmospheric water vapor profile at the ARM SGP CART site. To account for the dry-bias of the radiosondes, the radiosonde water vapor profiles from the SGP CART site are typically scaled to match the PWV measured by the MWR. This procedure has considerably improved the spectral residuals between the AERI and LBLRTM [*Revercomb et al.*, 2002].

Uncertainties in the MWR Measurements

The ARM MWRs are continuously and automatically self-calibrated using an algorithm outlined extensively in [*Liljegren*, 2000b]. This calibration algorithm, when applied to the sky signal recorded by the MWR, produces an effective blackbody temperature. This procedure maintains the MWR calibration to within a 0.2 - 0.3 K root-mean-square (RMS) error.

Uncertainties in the Integrated Column Water Vapor Retrieval

The PWV is retrieved from the microwave brightness temperature at 23.8 GHz, respectively, using a statistical retrieval, with retrieval coefficients specifically derived for the month of the measurement. For 0.2 K RMS in measured brightness temperatures, *Liljegren* [2000a] estimates the RMS error in the PWV using a statistical retrieval to be 0.01 cm in January to 0.025 cm in July.

There is a considerable research effort being put forth by the ARM science community to address other sources of model and/or measurement uncertainties. For example, S. Clough and K. Cady-Pereira (personal communication) have demonstrated that there is a bias between modeled and observed brightness temperatures of $\pm$ 0.7 K at 23.8 GHz. Such biases could translate into larger uncertainties in the PWV retrieval.

Carbon Dioxide Measurements

Located within 1 kilometer of the NSA CART site is a National Oceanic and Atmospheric Administration Climate Monitoring and Diagnostics Laboratory (NOAA CMDL). The Barrow CMDL station measures a number of important atmospheric constituents which are capable of altering the climate (i.e. carbon dioxide and ozone). In-situ carbon dioxide measurements are continuously taken with a non-dispersive infrared analyzer. These measurements, supported by the NOAA CMDL Carbon Cycle Group, are available at the internet site http://www.cmdl.noaa.gov.

Ozone Measurements

The column of ozone between the surface and the top of the atmosphere is routinely measured with a Dobson Ozone Spectrophotometer and the Total Ozone Mapping Spectrometer (TOMS)[1]

The Dobson spectrophotometer in Barrow is one of 15 spectrophotometers operated and maintained by NOAA CMDL, and is part of a global effort to monitor the effects of stratospheric ozone on the global population and climate. Data from the NOAA CMDL Barrow instrument were obtained from the World Ozone and Ultraviolet Radiation Data

[1]The total column of ozone is reported in Dobson units (DU) at NOAA CMDL. One Dobson unit refers to a layer of ozone that would be 0.01 m thick under conditions of standard temperature (0° C) and pressure (the average pressure at the surface of the Earth).

Center (http://www.msc-smc.ec.ga.ca/woudc), operated by the Experimental Studies Division of the Meteorological Service of Canada.

The Total Ozone Mapping Spectrometer, launched in July 1996 onboard an Earth Probe Satellite (TOMS), provides long-term daily mapping of the global distribution of the Earth's atmospheric ozone from the Antarctic to the arctic. TOMS has largely supplied the ozone maps which illustrate the slow but steady change in the stratospheric ozone layer. TOMS data can be conveniently obtained on the internet from the site "Ozone over Your House" (http://toms.gsfc.nasa.gov/teacher/ozone_overhead.html).

Dobson and TOMS data are available only when sunlight is present above the NSA CART site.

5.2.3 Specification of the Longwave Radiation Field

The Extended-Range Atmospheric Emitted Radiance Interferometer

The Extended-Range Atmospheric Emitted Radiance Interferometer (AERI-ER) measures the zenith, absolute longwave spectral radiance (watts per square meter per steradian per wavenumber), outputting a spectrum every 8 minutes [*Revercomb et al.*, 1996; *Knuteson et al.*, 1998]. The usable spectral range of the instrument is 400 to 3000 cm^{-1} with a spectral resolution of 0.4812 cm^{-1} and field-of-view of 1.3 degrees. The AERI-ER is deployed within the Great White and operates continuously. The interferometer mirror views the outside scene through a hatch opening in the shelter, and the AERI-ER enclosure is ventilated with ambient air. During periods of precipitation the hatch opening is automatically covered, and the data are marked with a quality control flag.

Uncertainties in the AERI-ER Measurements

To use the AERI-ER for retrieval of atmospheric temperature and humidity, a primary scientific goal for the instrument, requires high radiometric precision and accuracy. To achieve this, the AERI-ER system provides a real-time data calibration by adjusting the mirror on the interferometer to view two high-emissivity, blackbody cavities between every scene view (one blackbody at ambient temperature, one blackbody at 330 K) [*Revercomb et al.*, 1988]. This method of calibration provides accurate temperature reference points using standards traceable to the National Institute of Standards and Technology [*Best et al.*,

1997]. The radiometric accuracy of the observed AERI-ER radiances depends on the uncertainties in the blackbody temperatures and emissivities. The bottom panels of Figure 5.3 and Figure 5.4 show the estimated uncertainties for the two sky scenes presented in the top panels. The algorithm for calculating the spectral AERI-ER uncertainty was authored by D. Tobin and D. Turner at the University of Wisconsin.

The Pyrgeometer

A pyrgeometer is a radiometer which measures hemispheric, broadband longwave irradiance on a planar surface (watts per square meter). During the period of this study two Eppley Laboratory, Inc., Precision Infrared Radiometers (PIRs) were operational at the NSA CART site. The PIR is constructed with an Eppley thermopile, covered with a precision-ground silicon dome to protect the thermopile detector and to filter out all but longwave radiation.

The PIRs operate continuously, and are mounted on a stand about 2 m above Great White trailer to provide maximum hemispheric access. One of the PIRs is covered by a solar-tracking mechanism to block the direct shortwave (solar) flux from the thermopile detector. This PIRd (known as the PIR diffuse in ARM nomenclature) is used in the intercomparison.

Uncertainties in the PIR Measurements

For the standard ARM pyrgeometer, the longwave flux, F_{PIR}, is computed from the raw data using the [*Albrecht et al.*, 1974] formula:

$$F_{PIR} = \frac{U_{emf}}{C} - K\sigma_{sb}(T_D^4 - T_B^4) \tag{5.1}$$

where U_{emf} is the thermopile signal, T_B and T_D are the absolute temperature of the pyrgeometer body and dome, σ_{sb} is the Stefan-Boltzmann constant, and C and K are the pyrgeometer calibration and dome correction factors. The pyrgeometers in the ARM program are calibrated annually with blackbody sources at an off-site location.

In the early 1990s uncertainties of up to 10% were present in atmospheric longwave flux measurements [*Dehne et al.*, 1993]. However, through intensive investigations of pyrgeometer calibration methods and the improved blackbody sources the PIR uncertainty

has been reduced to 2-3%. A number of additional factors can contribute to uncertainties in PIR measurements, including accumulation of precipitation or dust on the optical surfaces of the instrument or positioning of the instrument off of the horizontal plane. A number of steps have been taken to reduce these uncertainties, such as (a) installation of a ventilation system to reduce accumulation of materials on the instrument dome, and (b) installation of a spirit level to ensure horizontal positioning.

5.2.4 Radiative Transfer Models

Two radiative transfer models are used in this intercomparison: the line-by-line model radiative transfer model LBLRTM and the rapid radiative transfer model RRTM. LBLRTM calculates spectral transmittances, radiances, and fluxes with high accuracy at monochromatic resolution. LBLRTM radiance calculations have been extensively validated against high-resolution spectral measurements for many climatic conditions. Line parameters for the LBLRTM calculations have been obtained from the HITRAN 2000 database and the water vapor continuum data from the CKD model, version 2.4. RRTM was designed to reproduce the results of line-by-line models within the constraints of increased computational efficiency. These models have been extensively described in Chapter 1 and Chapter 4.

Uncertainties in the Model Calculations

To calculate atmospheric radiances and fluxes requires an input profile of the atmospheric temperature, pressure, and trace gas profiles. Atmospheric temperature, pressure, and water vapor typically come from balloon-borne sounding systems, while the remaining trace gases are specified either by satellite/ground-based instrument retrievals or available climatology (often the standard McClatchey atmospheres). There is no prescribed percent radiance or flux uncertainty due to errors in the input atmospheric profile, but the uncertainty can be estimated by bracketing the input profile with a high and low estimate of the most important parameters [i.e. perturbing the temperature and water vapor profile].

Consideration of the Instrument Locations in the Radiative Transfer Calculations

The relative placement of the instruments is a consideration in the measurement-model intercomparison. The PIRd is located on a deck above the Great White, but the AERI-ER was enclosed roughly two meters below the PIRd within the Great White. The AERI-ER enclosure is ventilated with outside air to minimize the introduction of warmer, inside air into the path of the interferometer. Since it is the atmospheric radiance/flux which is ultimately of interest, the location of the PIRd is considered as the reference location, and all flux calculations occur from the top of the atmosphere to the PIRd. Therefore, an effective AERI-ER radiance was developed which best represents the spectral radiance and flux at the position of the PIRd. The effective AERI-ER radiance $R_{aerier-eff}$ for each spectral element was determined as follows:

- Compute the radiance, $R_{lblrtm-path}$, and transmittance, $T_{lblrtm-path}$, with LBLRTM in the vertical path between the PIRd and the AERI-ER
- Compute the effective AERI-ER radiance from the actual AERI-ER measurement, $R_{aerier-msd}$, using the relation

$$R_{aerier-eff} = \frac{(R_{aerier-msd} - R_{lblrtm-path})}{T_{lblrtm-path}} \tag{5.2}$$

For consistency this technique is also applied to LBLRTM calculations of atmospheric flux at the PIRd.

Radiance to Flux Conversion for AERI-ER and LBLRTM

The AERI-ER measures zenith atmospheric radiance over the spectral range from 400 to 3000 cm^{-1}. Since the PIRd observes a broadband flux, an algorithm has been constructed to convert the AERI-ER spectral radiances, measured only from 400 to 3000 cm^{-1}, to a broadband irradiance. This conversion occurs in three steps: (a) the atmospheric state is defined for the time of the AERI-ER measurement, and LBLRTM is used to compute radiances from 10 to 400 cm^{-1}, and 3000 cm^{-1} to 3250 cm^{-1}, (b) the limited AERI-ER spectral domain is extended to 10 cm^{-1} using LBLRTM-calculated radiances, and (c) a radiance-to-irradiance algorithm is applied to the AERI-ER radiances [*Clough et al.*, 2000]. To directly compare

AERI-ER radiances with LBLRTM-calculated radiances, a sinc function with a half-width-half-maximum of 0.29096 has been applied to the LBLRTM-calculated radiances to account for the AERI-ER instrument response function, and the calculated radiances output to the same wavenumber grid as the AERI-ER.

The ratio of the flux to zenith radiance depends on the transmittance of the atmosphere for a given spectral element. For opaque conditions the radiation field is isotropic and this ratio equals π. However, for non-opaque conditions the ratio is greater than π. To obtain the appropriate ratio, RRTM is employed. Utilizing the same atmospheric profile as that for the LBLRTM calculation, RRTM computes the ratio of downward surface flux (using three Gaussian quadrature angles) to the downward zenith surface radiance for each of its 16 spectral bands. For each RRTM spectral band, the AERI-ER radiances falling with the band are summed and the RRTM flux-to-radiance ratio applied; the 16 spectral-band fluxes are then summed to produce the broadband AERI-ER flux. For consistency, the LBLRTM-calculated flux is obtained from the LBLRTM radiance in a manner identical to that used for the AERI-ER conversion.

The uncertainty associated with the radiance-to-flux conversion is small compared to other underlying uncertainties in the radiative transfer calculations, such as in the water vapor profile.

5.3 Selection of Clear Sky Cases

Cases for this intercomparison were selected from one annual cycle, January 1, 2001 to December 31, 2001. Requirements for a case to be selected for this intercomparison were: clear skies for 5 minutes before and 30 minutes after a radiosonde launch, and the existence of all necessary data (AERI-ER, PIRd, radiosonde, one or more cloud detection instruments). As a first screening, a visual inspection was done on an archive of "quick-look plots", which are daily time-series plots of instrument data. These plots are easily accessible from the NSA CART site/University of Alaska site operations web-page (http://nanuna.gi.alaska.edu).

A list of possible times was compiled, and all supporting data from these times were obtained from the ARM archive (http://www.arm.gov). To further ensure that radiatively

important clouds were not present surrounding the radiosonde launch, a value-added product available from the ARM archive was employed. The Active Remotely-Sensed Clouds Locations (ARSCL VAP) combines data from a Vaisala laser ceilometer, microwave radiometer, and a micropulse lidar to produce a time series of cloud hydrometeors over the NSA CART site. In cases when the ARSCL VAP did not exist, the data for any one of the individual cloud-detections instruments were obtained and screened. Additionally, in cases in which the presence of a cloud was in question the time series of broadband longwave and shortwave flux data were examined. Fluctuations in the flux data indicate a cloud could be present; therefore, the case would not be used.

Since radiosondes require manual labor to launch, radiosondes are limited to once-per-day through the work week (holiday/operator vacation periods also excluded). This severely restricts the number of clear-sky candidates, as well as the ability to look at diurnal variations in the measurements. For this intercomparison, 17 cases were examined with PWV values ranging between 0.10 and 1.6 cm, and near-surface air temperatures between -36 °C and 7 °C. The ensemble radiosonde temperature and two water vapor profiles, corresponding to both the original radiosonde measurement and a Vaisala-corrected water vapor profile (discussed in Section 5.2.2), are shown in Figure 5.6. Since the first screening for intercomparison cases was done visually, there may have been additional times which fit the criteria for the intercomparison. However, due to the large volume of data, the screening process was not automated since this would require all the NSA CART site data initially.

5.4 Radiance and Flux Closure Analysis

For each of the 17 cases, baseline downward radiances were calculated with LBLRTM v6.01 from the top of the atmosphere to the AERI-ER, and compared to the AERI-ER observation centered within 7 to 15 minutes of the radiosonde launch. The baseline atmosphere was constructed using the original radiosonde measurements of altitude, pressure, temperature, and water vapor to describe the lower 15-20 km of the atmosphere (depending on the location of the last usable radiosonde measurement), and the subarctic-winter/summer climatology to describe the region from 20 km to the top of the atmosphere. The car-

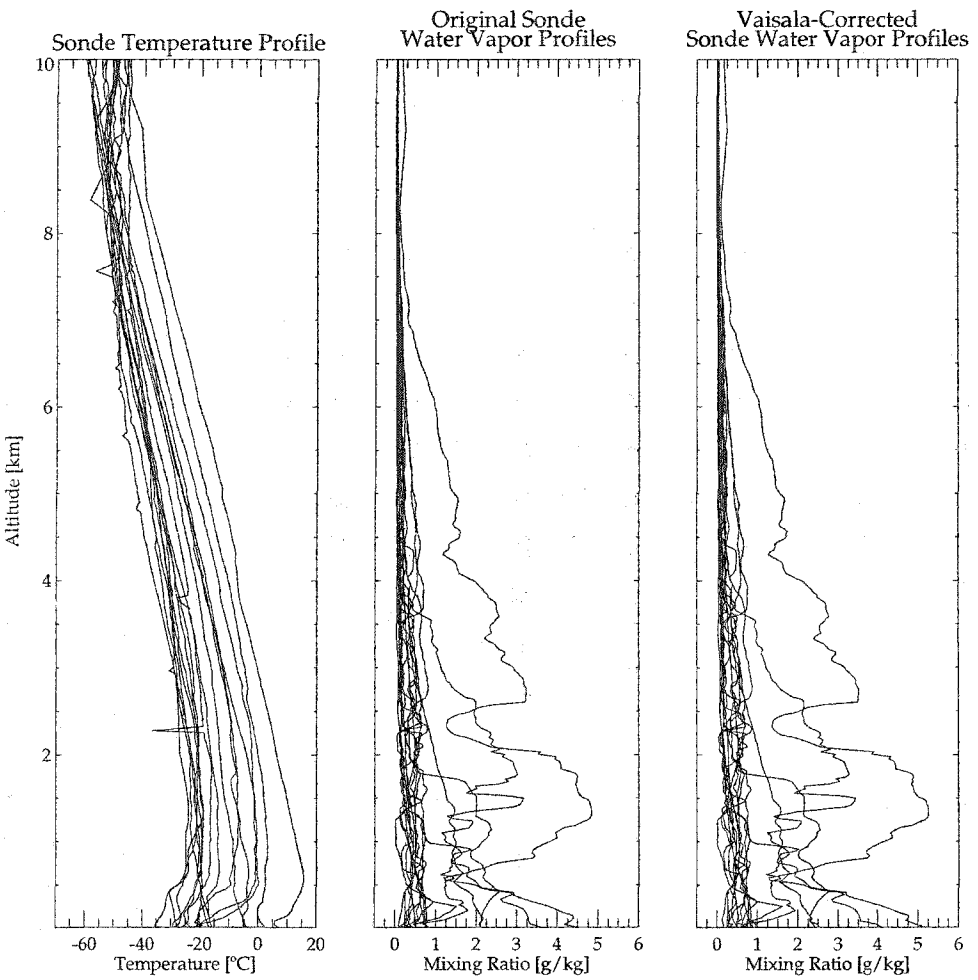

Figure 5.6. Ensemble of atmospheric profiles for the NSA CART site model and observation intercomparison. The temperature profiles are presented in the left panel; the water vapor mixing ratio profiles, derived from the RS-80 Vaisala radiosonde relative humidity measurements, are shown in the center panel. The RS-80 relative humidity measurements are known to have a dry-bias. *Wang et al.* [2002] developed a correction algorithm for the dry-bias; this correction was applied to the relative humidity measurements, and the corrected water vapor mixing ratios are shown in the right panel.

bon dioxide mixing ratio was obtained from the NOAA CMDL instrumentation; all other gases were set to the sub-arctic winter/summer climatological values. No aerosols were considered, and multiple-scattering was ignored in the radiative transfer calculations. The choices for the baseline atmosphere were chosen to mimic the approach commonly taken in construction of atmospheric profiles from standard data.

Figure 5.7 illustrates the baseline spectral mean and standard deviation (blue lines) of the observation - calculation for the ensemble of profiles in the intercomparison. The spectral residuals offer the chance to investigate the sources of error associated with the atmospheric state description, the radiometric measurements, and the radiative transfer models. Careful analysis of the spectral residuals has resulted in an improved set of radiance calculations with LBLRTM (hereafter referred to as the best-estimate calculations), and are represented by the red lines in Figure 5.7.

The best-estimate, LBLRTM-calculated radiances were then adjusted to account for the atmospheric path between the AERI-ER and the PIRd, and converted to flux. RRTM fluxes were also computed to show the performance of RRTM both against LBLRTM and the field measurements. This intercomparison is important given the prominence of broadband measurements both in climate model evaluations and weather forecasting.

5.4.1 Spectral Analysis: AERI-ER and LBLRTM

The Atmospheric Window

The transparent spectral region (800 to 1200 cm^{-1}) plays an important role in the Earth's climate since it provides a window for the Earth's emission to escape to space. In the presence of clouds this window can become opaque. The mean residuals for this spectral region (with the exception of the ozone band from roughly 980 to 1080 cm^{-1}) are on the order of 0.75 $mW/(m^2\ str\ cm^{-1})$, irrespective of the atmospheric temperature profile and column water vapor amount. Possible explanations for these residuals are either contamination by aerosols or diamond dust, large errors in the water vapor field, or an error in the AERI-ER calibration or observation. Large errors in the water vapor field are unlikely, since this error would be seen to a much greater extent in the spectral regions sensitive to water vapor. It is possible that contamination by aerosols or diamond dust could explain

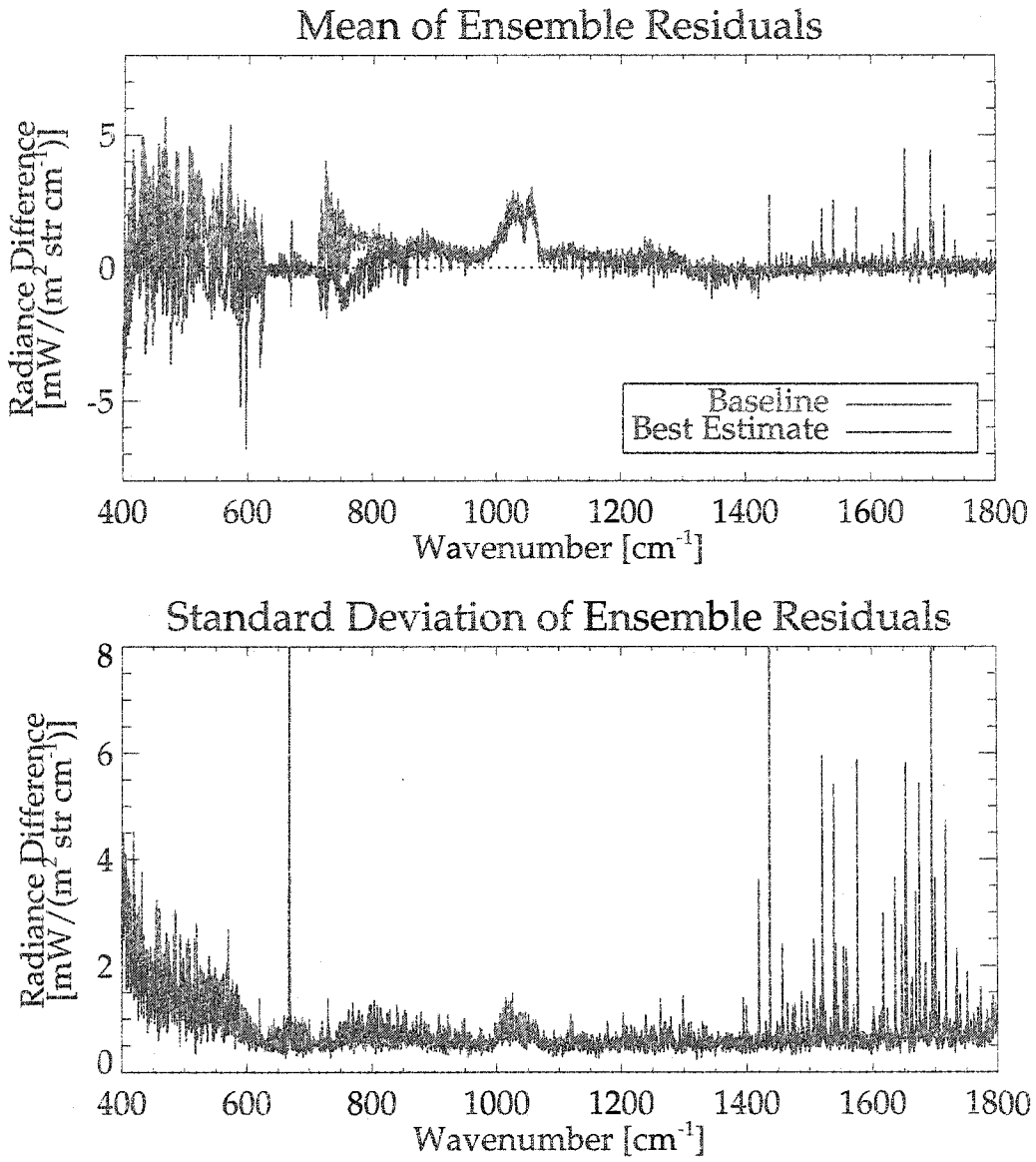

Figure 5.7. Mean and standard deviation of AERI-ER - LBLRTM spectral residuals for baseline and best-estimate calculations. Mean and standard deviation of AERI-ER - LBLRTM spectral residuals for the ensemble set of 17 NSA CART site atmospheres. The blue lines represents the baseline mean (top panel) and standard deviation (bottom) of the baseline spectral residuals. Careful analysis of the physical processes which contribute to the modeled baseline radiance profiles has yielded improvements in the methods used to characterize the atmosphere state as well as in the model LBLRTM itself. These improvements are reflected in the best-estimate mean and standard deviation of the spectral residuals (red lines).

a small percent of these residuals. However, these residuals have been seen consistently at the ARM SGP CART site, where diamond dust is not observed [*Tobin et al.*, 2000]. Therefore, the AERI-ER calibration is a strong candidate for the explanation of these residuals. The University of Wisconsin team that developed the AERI-ER is investigating possible calibration issues, and a report on their findings shall be forthcoming within the next year (personal communication, D. Turner).

Temperature Profile Analysis

The absorption characteristics of the strong 15-μm carbon dioxide band make it a useful tool for examining the thermal structure of the lowest 3 kilometers of the atmosphere [*Feltz et al.*, 1998]. Emission from carbon dioxide is related directly to the atmospheric temperature. The most opaque region of the CO_2 band is its center (667 cm^{-1}); therefore, emission received at the AERI-ER detector originates from the instrument face. Moving away from the center of the band in wavenumber space the atmospheric emission from CO_2 originates from higher altitudes due to the decreased absorption efficiency of CO_2 [*Feltz et al.*, 1998]. The top panel of Figure 5.3 demonstrates this concept. In the case of the atmosphere whose temperature decreases with altitude through the boundary layer (October 2, 2001) the AERI-ER radiance decreases with increasing wavenumber distance from the band center. Conversely, when the atmospheric temperature increases with altitude, such as on November 21, 2001, the radiance dramatically increases outward from the band center. The spike at 667 cm^{-1} is an artifact of the AERI-ER calibration and should be discounted.

The vertical profile of atmospheric temperature is typically measured by a radiosonde. The quality of the radiosonde temperature measurements can be examined by comparing modeled spectral downward radiances in the 15-μm carbon dioxide band, where the emission is a strong function of atmospheric temperature, to those observed by the AERI-ER. Using the radiosonde temperature profile the spectral downward radiance was calculated by LBLRTM for each NSA CART site case study. The spectral residuals for these baseline calculations are shown in Figure 5.8 (blue lines); the spectral residuals for the mean ensemble of profiles is shown in Figure 5.7. The date and time of each case study is denoted on the top of each panel using standard ARM nomenclature: *yyyymndy.hhmm*, where *yyyy* is the four-digit year, *mn*, *dy*, *hh*, and *mm*, is a two-digit month, day, hour, and minute,

respectively. For example, 20010311.1113 denotes March 11, 2001, 11:13 GMT. A number has been assigned as well to each case study, denoted in the top, left corner of each panel.

There are several examples of cases, such as case 1, case 2, and case 17, in which the model - calculation differences exceed the differences which would be expected from uncertainties in the measurement. These residuals can be attributed to an incorrect specification of the atmospheric temperature in the lowest part of the atmosphere. During the annual cycle of 2001 the radiosonde was initialized with temperature and pressure information from NOAA CMDL instrumentation as well as launched from NOAA CMDL, located about 100 meters from the Great White instrument trailer. After activation of the radiosonde it is brought inside an enclosed garage, attached to the flight balloon, brought back outside, and released without (necessarily) adequate environmental acclimation of the sensors. Additionally, with the rapid ascent of the balloon-borne radiosonde the temperature structure in the lowest hundred meters of the atmosphere may not be accurately represented by the 10-second radiosonde data (described in Section 5.2.2), and low-level temperature inversions can be missed.

An alternative to using the radiosonde to describe the low-altitude temperature profile is to use the temperature profile from the BMET tower, located about 100 meters from the Great White. To incorporate the BMET data, all radiosonde temperature, pressure, and humidity data below 50 m were replaced with the BMET data at 2, 10, 20, 40 m at the time of the radiosonde launch. Figure 5.9 shows the difference in the two atmospheric temperature profiles for each case study; the BMET data points are represented by the (+) symbol and solid line, and the radiosonde points are represented by the (*) symbol and dashed line. The case numbers are noted in the upper-left corner of each panel. In the one case (case #7) where BMET data are missing, the sonde data were used.

The downward surface radiances were re-calculated using the modified temperature profile. The new spectral residuals for each case study are shown by the red lines in Figure 5.8. Comparing the spectral residuals from the baseline calculations (blue lines in Figure 5.8) to the spectral residuals resulting from the modified temperature profile demonstrate that 6 out of 17 cases improve by replacing the radiosonde data with the BMET data, 1 case deteriorates, and 9 cases do not change significantly. The cases with significant change correspond to the largest differences in the radiosonde and BMET data. For case 1 and case

2 (20010311.1113 and 20010312.1059) the spectral residuals resulting from the calculations with only the radiosonde temperature profiles are positive, e.g. the observed radiances are greater than the calculated radiances. This implies that the temperature of the actual atmosphere was warmer than the temperatures reported by the radiosonde 10-second data. The BMET data for case 1 and case 2 indicate a strong temperature inversion was, indeed, present in the lowest 40 m of the atmosphere; hence, the spectral residuals using the combination of the BMET and radiosonde temperature profiles improve significantly. For case 17 (20011204.2308) the spectral residuals from the radiosonde-only calculations are negative, indicating that the temperature of the actual atmosphere was colder than the temperature reported by the radiosonde. An examination of the radiosonde temperature profile versus the BMET data indicate there was an erroneously warm radiosonde point at 25 m; hence, the radiances calculated from the combined BMET-radiosonde profile are in good agreement with observations. For case 10 (20010702.2255) there are residuals for either temperature characterization; however, there is an improvement in the center of the band, which indicates that the lower atmosphere is characterized correctly but there are remaining problems with the characterization of the temperature field above 40 m.

The temperature field is the dominant source of error in model calculations of radiance in the 15-μm CO_2 band. In the case studies presented, the radiances calculated from the radiosonde temperature field generally agree well with the AERI-ER radiances. Improvement in the residuals can be made in the most opaque regions of the band by improving the characterization of the temperature field in the lowest 40 m of the atmosphere, as demonstrated in Figure 5.8. The residuals are well above the uncertainty in the AERI-ER measurement, which is roughly 0.1 mW/(m^2 str cm^{-1}) in the 15-μm CO_2 band, as shown in Figure 5.3 and above the uncertainty associated with specification of the CO_2 mixing ratio. Given the uncertainties associated with the radiosonde launch and the apparent improvement in the residuals associated with the BMET data, it is appropriate that comparisons of LBLRTM-calculated radiances with those observed by the AERI-ER utilize the BMET data.

Feltz et al. [1998] and others have successfully retrieved temperature (and water vapor) profiles within the planetary boundary layer using data from AERI instruments. The algorithms developed for these retrievals (known as AERI Plus) will soon become operational at the NSA CART site [*Feltz et al.*, 2001]. This information will be extremely valuable both

in evaluating radiosonde measurements but also to provide boundary layer temperature profiles on the 8-minute time grid of the AERI measurements. The nominal vertical resolution of the current AERI Plus retrieval is 10 mbars between 1000 mbars and 900 mbars, 20 mbars and greater above 900 mbars.

Water Vapor Profile Analysis

The water vapor profile of the atmosphere has an enormous impact both on downward radiance and flux throughout a large portion of the longwave spectral region (as discussed extensively in Chapter 1). A unique feature of the AERI-ER is its ability to observe radiance in a portion of the purely rotational band of water vapor (400 to 620 cm^{-1}). In this spectral region the residuals are particularly dependent on the water vapor profile rather than other regions where the water vapor lines are more opaque. The mean residuals for the baseline ensemble of cases, illustrated by the blue line in Figure 5.7 have a positive trend, indicating that there may be a dry bias in the water vapor profile. This finding is consistent with residual analysis from the SGP CART site. To account for this dry bias, the SGP CART site AERI/LBLRTM QME now scales the PWV measured by the radiosonde to that of the SGP CART site microwave radiometer (MWR). Studies by *Wang et al.* [2002] concluded that the radiosondes were biased due to contamination of the polymer used in the capacitive relative humidity sensor. To assess the uncertainties in the water vapor profile, the baseline case was perturbed both to scale the original radiosonde measurement by a correction algorithm recommended by *Wang et al.* [2002] as well as by the MWR at the NSA CART site.

Figure 5.10 illustrates the ensemble spectral mean and standard deviation of the observations - calculations for the original radiosonde (OSD, blue line), Vaisala-corrected radiosonde (VSD, red line), and the MWR-scaling of the original radiosonde (MSD, green line). For the 400 to 620 cm^{-1}, the mean residuals for the original radiosonde profiles are slightly positive, averaging +1.5 $mW/(m^2\ str\ cm^{-1})$; the mean residuals for the MWR-scaled radiosondes are slightly negative, averaging -1 $mW/(m^2\ str\ cm^{-1})$ whereas the mean residuals for the Vaisala-corrected radiosonde are centered around the zero line.

Closer examination of the 17 cases reveal a number of important considerations to be made when choosing the most appropriate method to characterize the atmospheric water

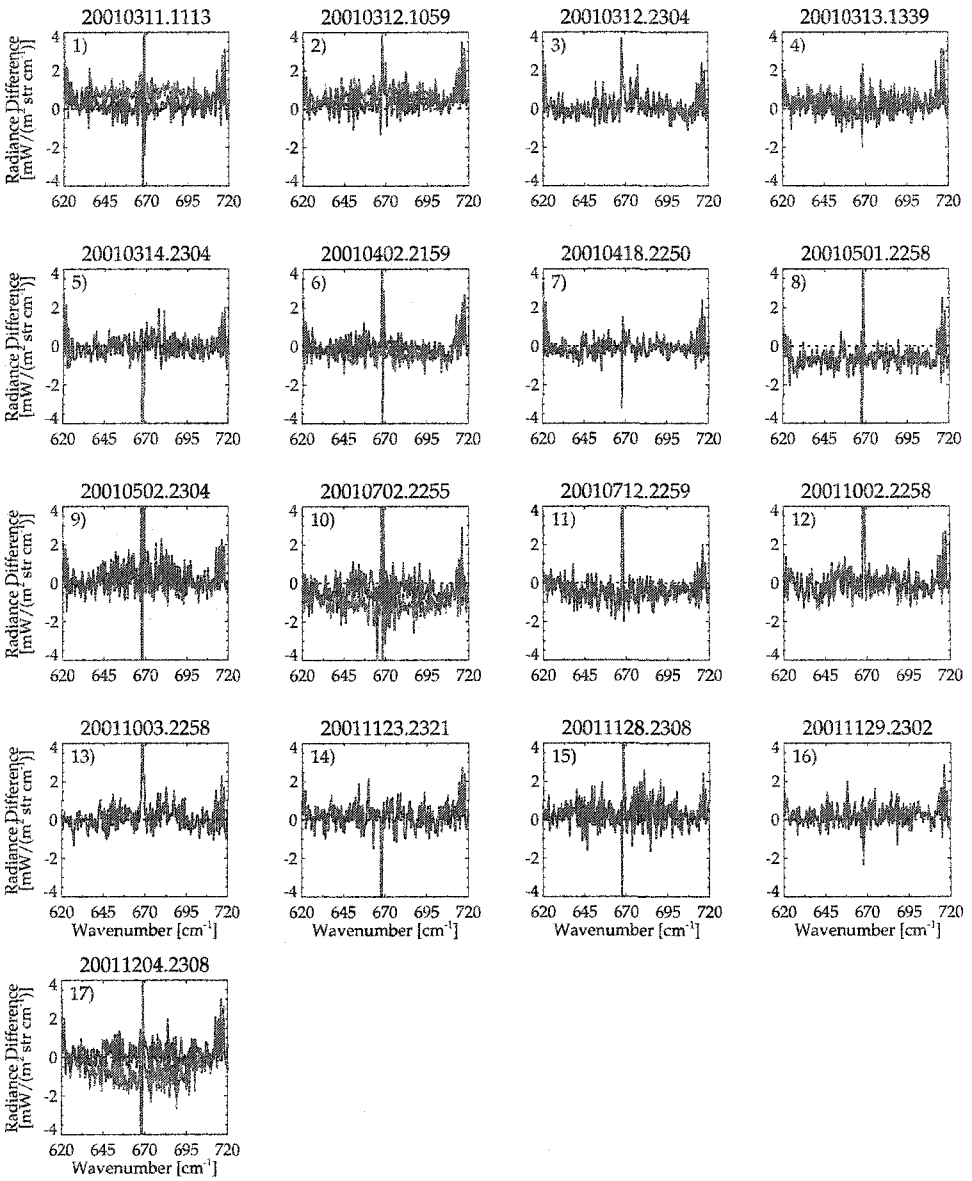

Figure 5.8. Spectral residuals for each NSA CART site case study in the 15-μm band of CO_2. Radiance differences between the AERI-ER radiance spectrum and LBLRTM-calculated radiance spectrum, which used temperature profile obtained from radiosonde measurements as input, for the 15-μm carbon dioxide band are presented for 17 case studies at the NSA CART site (blue lines). The radiance differences can be reduced (red lines) when the model calculations use temperature profiles in which the temperature of the lowest 40 m of the atmosphere is obtained from the BMET, rather than the radiosonde data. The case number is noted in the upper-left corner of each panel.

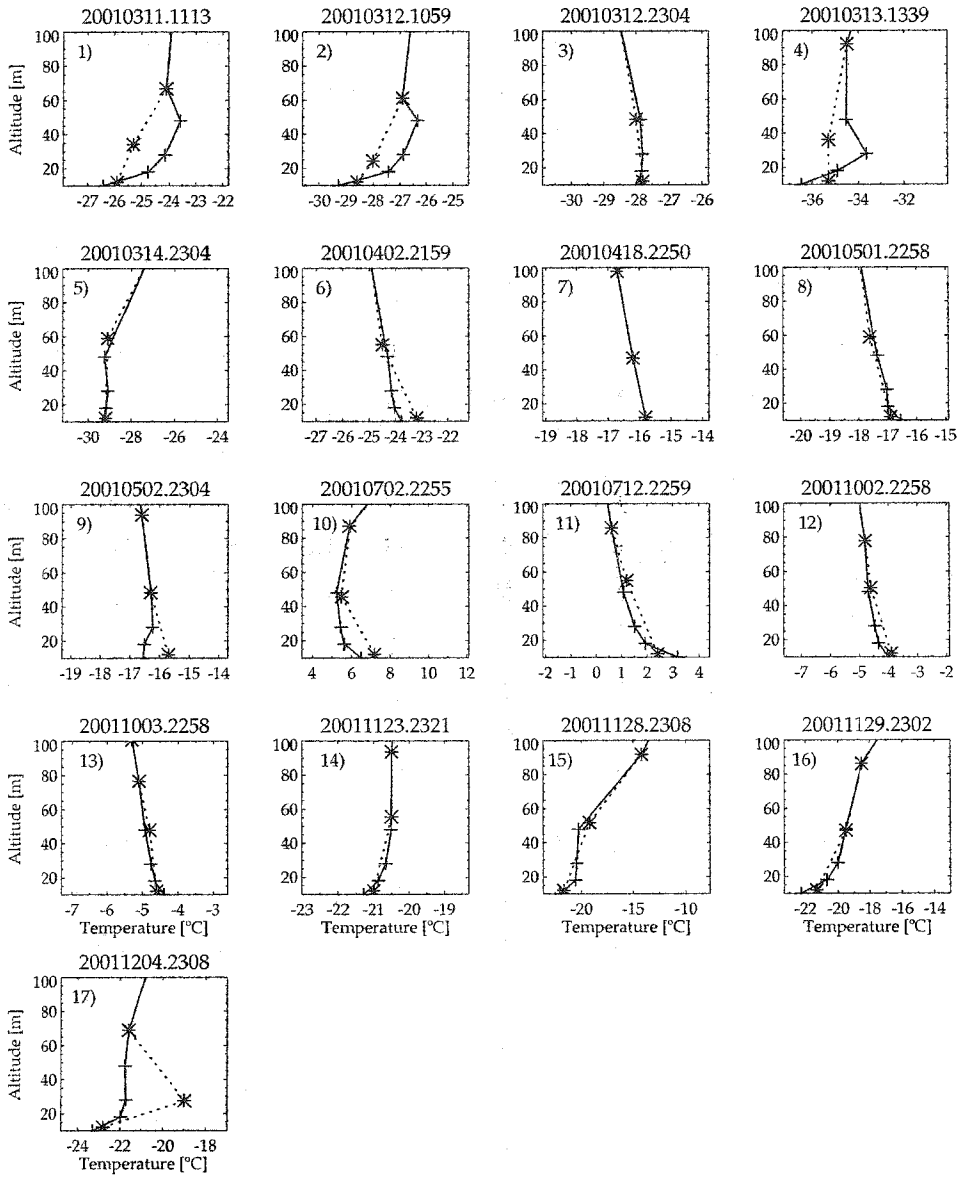

Figure 5.9. Sonde and BMET profiles for the ensemble of NSA CART site case studies. radiosonde (dotted line, *) and BMET profiles (solid line, +) for the ensemble of NSA CART case studies, arranged by date and time (noted on the title of each panel). The case number is noted in the upper-left corner of each panel.

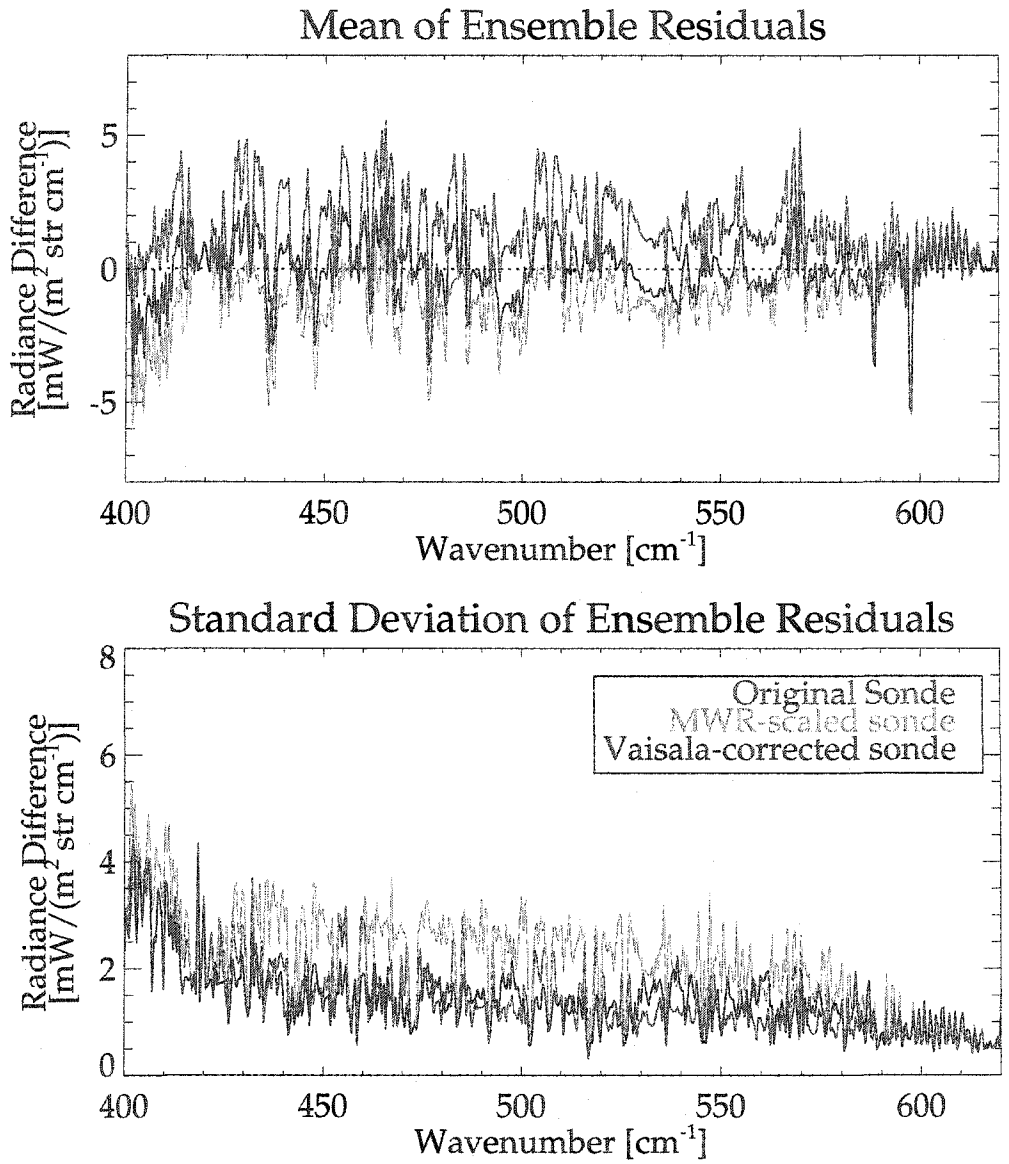

Figure 5.10. Mean and standard deviation of spectral residuals for variations in atmospheric water vapor. Mean and standard deviation for three treatments of the atmospheric water vapor profile for ensemble of cases: original radiosonde (blue line), applying Vaisala correction to the original radiosonde data (red line), and scaling the original radiosonde to match the PWV retrieved from the MWR (green line).

vapor profile. The individual case residuals are shown for the OSD (blue line) and MSD (green line) in Figure 5.11, and similarly for the OSD (blue line) and VSD (red line) in Figure 5.12. The panels in these figures have been arranged in order of increasing PWV as measured by the original radiosonde. The MSD radiances exhibit greater variability with respect to the AERI-ER observation, particularly in cases of low water vapor, than the VSD radiances, as is also evident in the standard deviation panel of Figure 5.10. However, the residuals in the MWR-scaled sonde radiance calculations improve with increasing water vapor in the atmosphere. This result is not unexpected, as a similar result was found in the [*Tobin et al.*, 2000] analysis for SHEBA AERI-ER/LBLRTM intercomparison. There are several known and currently-under-investigation uncertainties associated with MWR retrievals of PWV. Until these uncertainties are quantified to a greater extent, the MWR-scaling for the 17 cases presented is not adequate, but MWR-scaling should not be eliminated as an option for future intercomparisons.

In the case of the Vaisala-corrected radiosondes, the PWV always increases from that of the original radiosondes. In cases where the PWV is extremely low (below 0.3 cm) the Vaisala-corrected radiosondes appear to improve the residuals. In the cases with higher PWV, the VSD radiosondes sometimes overestimate the water vapor field, resulting in calculated radiances that are higher than the AERI-ER and, thus, negative residuals. The Vaisala-correction showed improvement in the water vapor characterization for the entire TOGA COARE data set, but is not necessarily expected to improve the water vapor profile of each individual radiosonde.

Clearly there is substantial uncertainty in the characterization of the water vapor field. The three scenarios presented bracket these uncertainties. To produce the smallest residuals for each case requires a combination of methods. The ARM scientific community is working on improving retrievals of PWV from the MWR at the NSA CART site, as well as exploring the possibility of using additional frequencies for the retrieval. For the 17 cases presented here the best estimate will utilize the Vaisala-correction algorithm to reduce the dry bias in the original radiosonde.

The known AERI-ER calibration uncertainties are on the order of 0.15 mW/(m^2 str cm^{-1}), placing it below the uncertainties introduced through the water vapor profile. However, it must be noted that a possible AERI-ER calibration error, discussed in section 5.4.1,

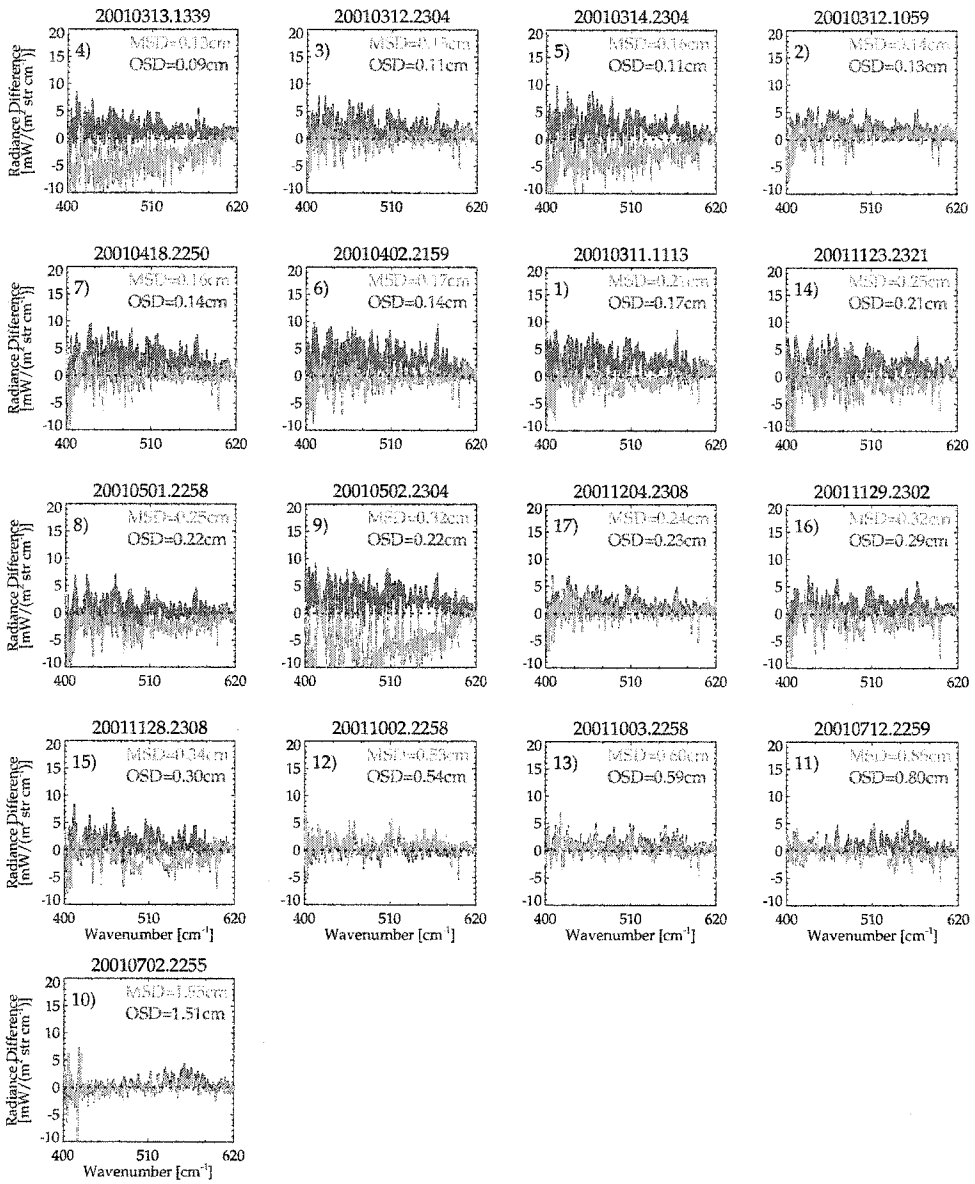

Figure 5.11. Spectral residuals for each NSA CART site case study in the 400 to 620 cm^{-1} portion of the purely rotational water vapor band: Original sonde v. MWR-scaled radiosonde. Spectral residuals for each case study in the 400 to 620 cm^{-1} portion of the purely rotational water vapor band. The blue line represents the baseline calculation with only the original radiosonde water vapor profile; the green line represents a calculation with the radiosonde PWV scaled to match that retrieved from the MWR.

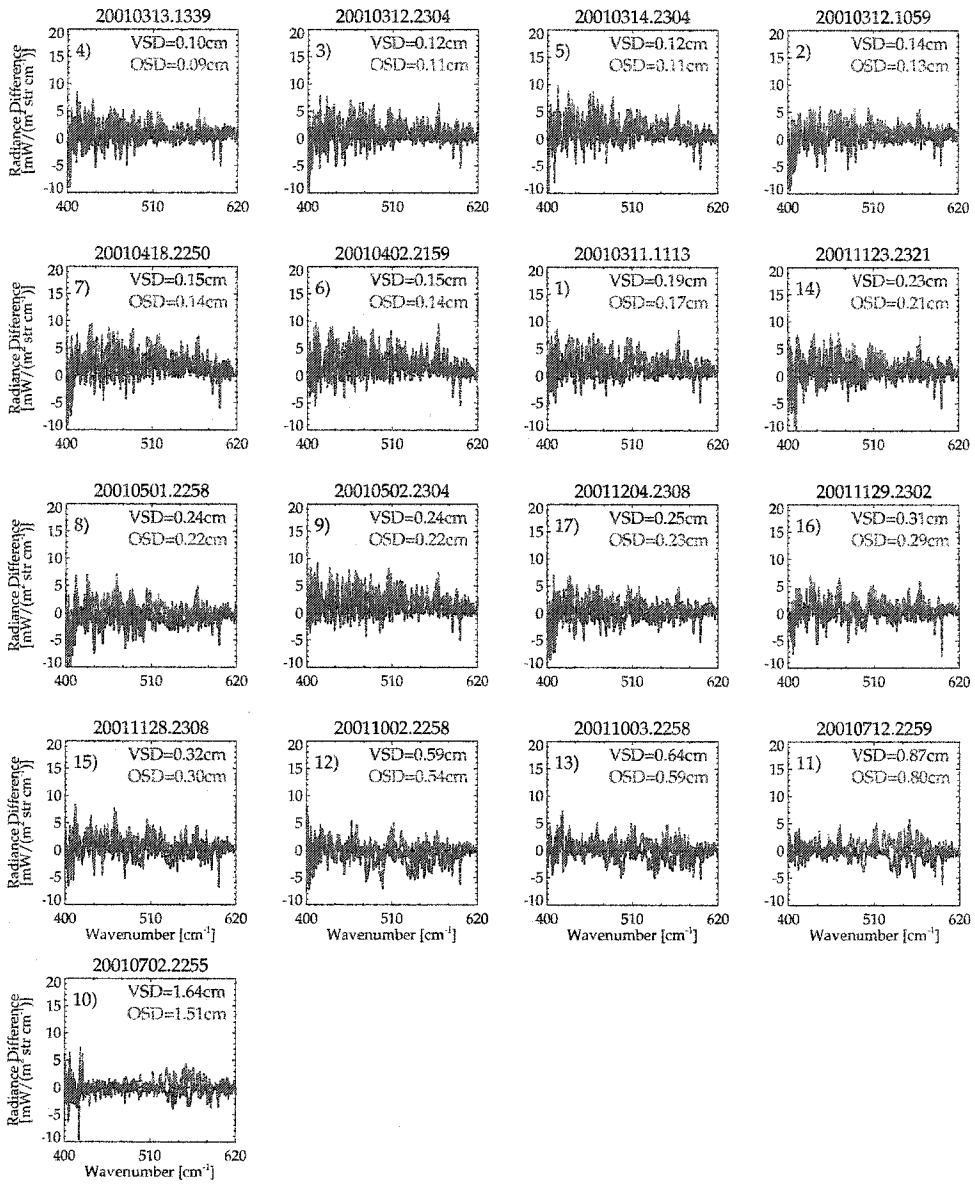

Figure 5.12. Spectral residuals for each NSA CART site case study in the 400 to 620 cm^{-1} portion of the purely rotational water vapor band: Original sonde v. Vaisala-corrected radiosonde. Spectral residuals for each case study in the 400 to 620 cm^{-1} portion of the purely rotational water vapor band. The blue line represents the baseline calculation with only the original radiosonde water vapor profile; the red line represents a calculation with the original radiosonde water vapor corrected by the Vaisala algorithms [*Wang et al.*, 2002].

may play a role in the apparent residual improvement associated with the VSD cases.

Ozone Profile Analysis

The fundamental vibration modes of ozone combine to form the prominent ozone band from 980 to 1080 cm^{-1}. There is a noted increase in observed - calculated residuals in this spectral region in Figure 5.7, indicating the climatological specification of the ozone field is not correct. A common practice in the specification of atmospheric ozone is to scale the total ozone column specified by climatology to match the total column ozone retrieved by the Total Ozone Mapping Spectrometer (TOMS). With the TOMS scaling, the spectral residuals do decrease slightly, as noted by the red line in Figure 5.7.

The NSA CART site also benefits from the NOAA CMDL Dobson spectrophotometer measurement of total column ozone. The Dobson measurement and the TOMS agree relatively well so for these case studies, no benefit is gained from using the Dobson instrument. To improve the residuals would likely require specific knowledge of the distribution of ozone throughout the atmospheric column, but there are no regular launches of ozone sondes to provide this information.

A portion of the residuals in this region may be attributed to the uncertainty in the AERI-ER observation.

Carbon Dioxide Line Shape and Continuum Analysis

After altering the water vapor profile, temperature field, and analyzing the impact of the ozone profile, there remain large spectral residuals on the wings of the CO_2 band (600 to 630,720 to 750 cm^{-1}). The magnitude and shape of these residuals were similar to those obtained in radiance comparisons between LBLRTM v6.01 and other high-resolution spectral instruments. As a result of these similarities *Shephard et al.* [2003] concluded the current CO_2 line shape parameters used in LBLRTM v6.01 could be improved, and the systematic errors in radiance and/or brightness temperature decreased. This was accomplished by reducing the carbon dioxide optical depths through an adjustment of the chi line shape factor and the carbon dioxide continuum. These changes were principally based on validations with the University of Wisconsin space-borne and ground-based interferometric

measurements. The improvement is illustrated in the baseline (blue line) and best-estimate residuals (red line) in Figure 5.7.

Overall Improvement in Spectral Residuals

The AERI-ER/LBLRTM intercomparison for the NSA CART site has yielded several improvements in the methods used to characterize the atmospheric state as well as an improvement to the model LBLRTM. Specifically, this study has shown that:

- The specification of the lower atmosphere temperature can be improved by replacing the radiosonde temperature profile below 40 m with the temperature profile from the meteorological tower BMET.
- The specification of the water vapor profile from the radiosonde exhibits a dry-bias, which can be corrected with the Vaisala-correction algorithm [*Wang et al.*, 2002].
- The specification of the ozone profile from climatology alone is not sufficient to accurately model downward atmospheric emission in the ozone band from 980 to 1080 cm^{-1}; however, scaling the total ozone column from the climatology to match that measured by TOMS does decrease the mean ensemble residuals.
- modeled emission from the wings of the carbon dioxide band, centered at 667 cm^{-1}, was too low, resulting in large positive spectral residuals; the spectral residuals improved when adjustments were made to the methodology that LBLRTM used to compute carbon dioxide optical depths.

It is important to note that the issue of the water vapor profile is still under consideration given the uncertainties in the AERI-ER observations, as noted earlier.

5.4.2 Flux Analysis

The subtleties revealed in the spectral analysis concerning the methodology for characterizing the atmospheric profile and the modeling of atmospheric gases will not necessarily be apparent in a broadband flux analysis. The AERI-ER/LBLRTM radiance analysis can be extended to the flux domain with steps outlined in Section 5.4.1. The ensemble mean flux

change from the baseline to the best-estimate scenario are presented in Figure 5.13 for both AERI-ER and LBLRTM. Panel A illustrates the total flux change in the LBLRTM calculations from the baseline (red bar) to the best-estimate calculation (orange bar), as well as the change in the AERI-ER flux calculation. From the baseline to the best-estimate scenario, the LBLRTM flux increased 2 W/m^2 from 168.4 to 170.4 W/m^2, whereas the AERI-ER flux decreased 0.3 W/m^2 from 171.8 to 171.5 W/m^2. (Note that the AERI-ER flux has a modeled component, as described in Section 5.4.1, which explains why the AERI-ER flux changes between the baseline and best-estimate scenario.) The spectral intervals plotted in the figure correspond to RRTM bands which were designed to enclose important absorption bands. Flux changes associated with the processes discussed above are plotted as follows: Panel B and Panel D (10 to 350 and 630 to 700 cm^{-1}, respectively) primarily illustrate changes in the temperature profile, Panel C and Panel H (350 to 600 and 1180 to 3250 cm^{-1}, respectively) primarily illustrate changes in the water vapor profile, Panel G (980 to 1080 cm^{-1}) illustrates changes in the ozone profile and highlights the approximately 0.5 W/m^2 residual remaining between AERI-ER and LBLRTM, Panel F (820 to 980, 1080 to 1180 cm^{-1}) illustrates the remaining residual in the atmospheric window, possibly attributable to the AERI-ER observation itself.

For each of the 17 atmospheric profiles, panel A of Figure 5.14 compares the best-estimate fluxes computed by LBLRTM to those from the PIRd (blue circles), the AERI-ER (red diamonds), and the rapid radiative transfer model RRTM v3.0 (green squares). Although a formal error analysis has not been performed, an estimate of the largest source of error is denoted by the black bar. The error in the PIRd is on the order of 3%, which generally exceeds that of the uncertainties in the fluxes due to model input, the model themselves, or the AERI-ER measurements. Therefore, the PIRd was increased and decreased by 3%, resulting in a range of uncertainty for the PIRd and LBLRTM differences. In all cases the flux residuals fall within the uncertainty of the broadband flux measurements. This indicates that there is good agreement in the flux domain between the high-resolution measurements from the AERI-ER, the line-by-line radiative transfer model LBLRTM, the rapid radiative transfer model RRTM, and the broadband measurement from PIRd for the cases presented.

To examine the possibility of trends in the residuals, the same residuals plotted in Panel

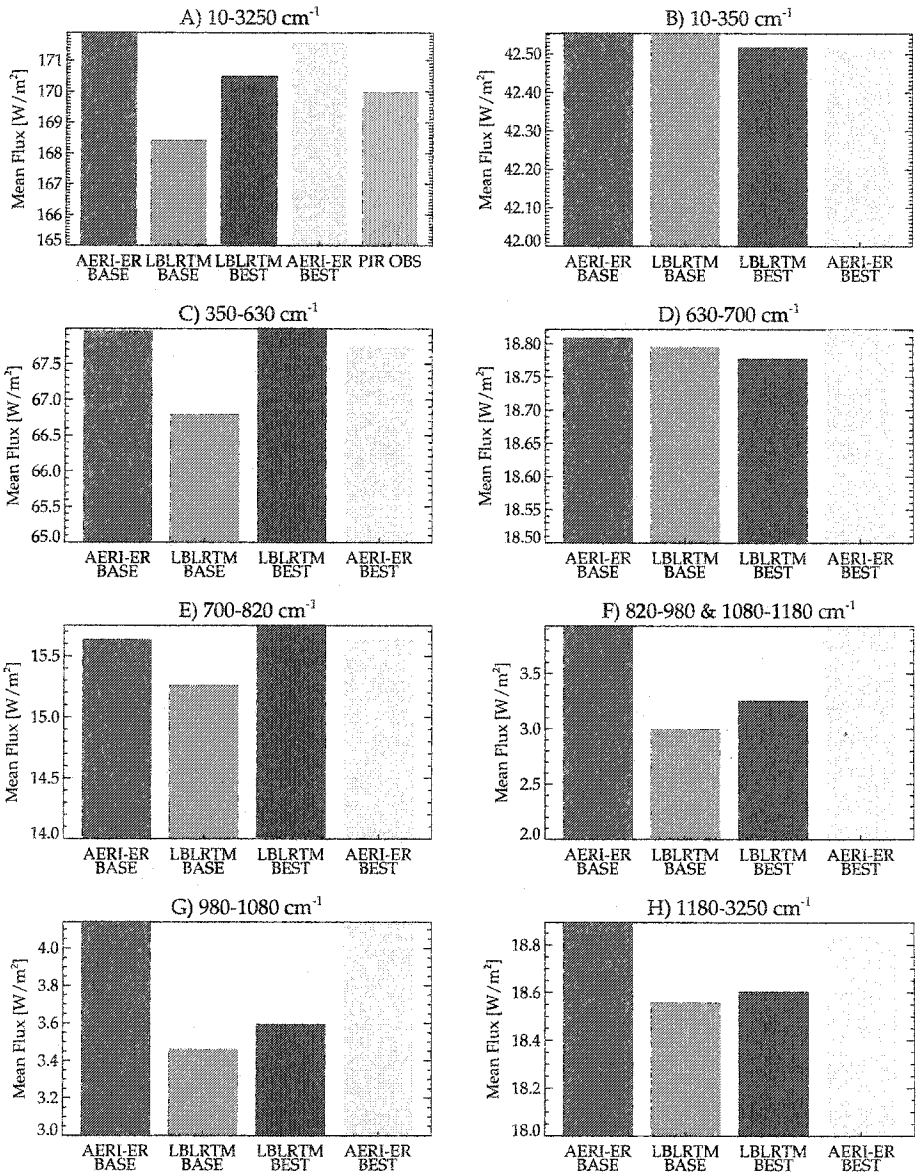

Figure 5.13. Estimate of flux impact on baseline to best-estimate changes. Mean calculated and observed AERI-ER and LBLRTM fluxes for the baseline (BASE) and best estimate (BEST) intercomparison for both the broadband and individual spectral bands. The mean PIRd broadband observation is also plotted. From the baseline to the best-estimate scenario, the LBLRTM flux increased 2 W/m^2, whereas the AERI-ER flux decreased 0.3 W/m^2.

A, Figure 5.14, are replotted as a function of PWV (Panel B), surface temperature (Panel C), broadband flux observed by the PIRd (Panel D), and as a function of the AERI-ER - LBLRTM residuals in the 350 to 600 cm^{-1} region (Panel E). The most significant trend that emerges is between the AERI-ER and LBLRTM fluxes when plotted as a function of the water vapor band residual (Panel E). This can be explained by re-examining the mean spectral residual plot in Figure 5.7. When there are negative radiance differences between the AERI-ER and LBLRTM in the 350 to 600 cm^{-1} spectral region, the integrated radiance difference improves due to a cancellation with the positive radiance differences in the atmospheric window and ozone region. As the water vapor band residuals become increasingly positive the overall residuals continue to increase as well.

Discussion of PIR Calibration

The Second International Pyrgeometer and Absolute-Sky Scanning Radiometer Comparison (IPASRC-II) [*Marty et al.*, 2003] was conducted at the NSA CART site in March 2001. Participants from 11 international institutions deployed 14 pyrgeometers, in addition to the Absolute Sky-scanning Radiometer (ASR) developed at the Physikalish-Meteorologisches Observatorium Davos and World Radiation Center [*Philipona et al.*, 2001]. The ASR measures radiance in a narrow 6° field-of-view at four elevation angles, and eight azimuthal directions. The downward flux is obtained by using Gaussian quadrature to integrate over the 32 ASR measurement points. The ASR, considered a reference quality instrument, is blackbody calibrated, and via these absolute temperature measurements are traceable to internationally accepted standards.

Marty et al. [2003] demonstrated the importance of calibration techniques in determining the precision of a pyrgeometer. The standard blackbody calibration, described in Section 5.2.3, is a good first step but an on-site determination of the calibration correction factor, using a reference instrument like the ASR, is the optimal method of calibration. Both IPASRC-I and IPASRC-II showed that the nighttime precision of an optimized pyrgeometer can reach levels of ± 1 W m^{-2}.

It should be noted that the ARM PIRd performed very well against the ASR. Of the 17 cases used in this intercomparison, three were from periods when the ASR flux measurements were available. For these three cases the PIRd agreed with the ASR to within 1 W

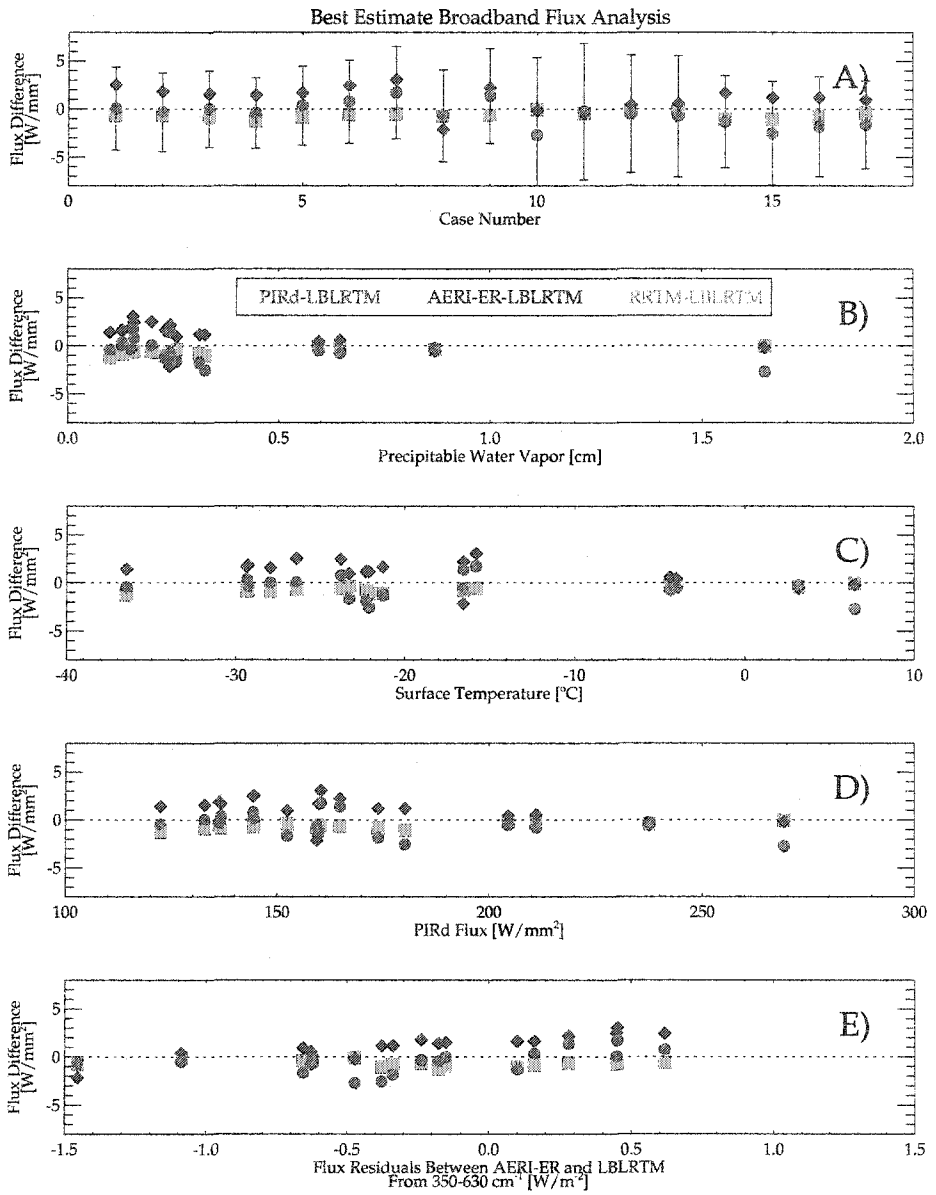

Figure 5.14. Flux residuals for each NSA CART site case study. Flux differences for the best-estimate flux intercomparison between the AERI-ER, PIRd, RRTM, and LBLRTM. The residuals are plotted as a function of case number (Panel A), total precipitable water vapor (Panel B), surface temperature (Panel C), and AERI-ER-LBLRTM residuals for a water vapor band (Panel D). The errors bars associated with the PIRd-LBLRTM, obtained by perturbing the PIRd measurement by its roughly 3% uncertainty, represent the largest overall uncertainty. This figure indicates that there is good agreement between the 4 tools used to obtain the downward flux at the surface of the NSA CART site.

m^{-2}. Two different PIRd's were used over the 2001 annual cycle at the NSA CART site. The PIRd at the NSA CART site for IPASRC-II was swapped with another PIRd on March 15, 2001, for its annual calibration. Therefore, the 3% uncertainty in the PIR measurements presented in Figure 5.14 can not necessarily be reduced.

Rapid Model Performance

The NSA CART site intercomparison offered an opportunity to compare the performance of the highly-accurate line-by-line radiative transfer model LBLRTM with a rapid radiative transfer model RRTM. Such a comparison provides useful information on the ability of GCMs, which include RRTM as their radiative transfer algorithm, to calculate accurate fluxes for cold, dry conditions arctic conditions. The baseline calculations for the intercomparison were performed using RRTM v3.0 and LBLRTM v6.01; the best-estimate calculations for the intercomparison were performed using LBLRTM v6.12, which was modified to improve the CO_2 line parameter formulation. To illustrate the sensitivity of the RRTM and LBLRTM flux differences to changes in LBLRTM itself, the mean flux of the ensemble of atmospheric profiles was calculated by three models, RRTM v3.0, LBLRTM v6.01, and LBLRTM v6.12, using the best-estimate atmospheres, and plotted in in Figure 5.15. The carbon dioxide absorption coefficient characteristics in RRTM v3.0 were constructed using the carbon dioxide formulation in LBLRTM v6.01, which results in only a 0.06 W/m^2 difference between RRTM v3.0 and LBLRTM v6.01. While the flux differences between RRTM v3.0 and LBLRTM v6.12 with the new CO_2 formulation are still relatively small (0.7 W/m^2), it is evident that to keep RRTM in step with LBLRTM requires that RRTM be updated to respond to changes in the advanced spectroscopy embedded in LBLRTM.

5.5 Summary

The main findings of the spectral radiance and flux analysis are summarized below:

- Specification of the vertical profile of water vapor is a large uncertainty in the characterization of the cold, dry arctic atmospheres. Radiosondes typically exhibit a dry bias, which can be corrected with the Vaisala correction algorithm [*Wang et al.*, 2002].

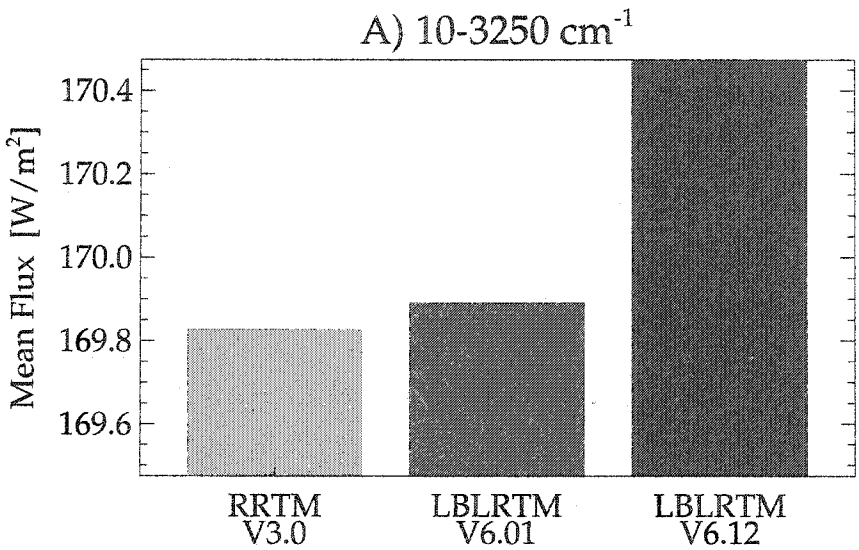

Figure 5.15. Impact of change in CO_2 absorption properties in radiative transfer model calculations. LBLRTM v6.01 (blue bar) and RRTM v3.0 (green bar) have the same CO_2 formulation, which results in only a 0.06 W/m^2 difference between the two models. LBLRTM v6.12 (red bar) has a modified formulation of CO_2 absorption, resulting in a 0.7 W/m^2 difference between RRTM v3.0 and LBLRTM v6.12.

The best uncertainty reduction may come from forthcoming improvements in microwave radiometry and retrievals.

- Radiances calculated using the vertical distribution of atmospheric ozone, as prescribed by standard climatologies, do not match radiances observed at the surface with the AERI-ER. Scaling the total column ozone of the climatology to match satellite retrievals of total column ozone does reduce the spectral residuals, but not significantly. Proper characterization of the vertical distribution of ozone, scaled to the Dobson or TOMS total column, would likely reduce the residuals. Ozone sondes are currently the best method to characterize the vertical ozone profile, but ozone sondes are expensive. Therefore, when measurement campaigns occur at the NSA CART site in which calculated longwave radiative fluxes are important, ozone sondes should be launched periodically.

- In general, fluxes observed by the pyrgeometer agree with model calculations and the flux derived from a high-resolution radiance instrument (AERI-ER). The maintenance and calibration of the PIRd is critical in preserving this agreement.

- The spectroscopy in line-by-line radiative transfer models benefit greatly from high-resolution spectral measurements. The spectroscopic improvements can then be transferred into rapid radiative transfer models, which are a critical component of climate and numerical weather forecasting models.

Chapter 6

Summary and Future Work

6.1 Thesis Summary

Radiative processes create regions of heating and cooling in the atmosphere which directly affect the dynamics and thermodynamics of Earth's atmosphere. The accuracy of weather forecasts and climate change predictions are, in part, determined by the accuracy of the radiative transfer calculations within the forecast and climate models. In the longwave spectral region, the complex line structures of the numerous radiatively active gases make radiative transfer calculations particularly demanding. Line-by-line models compute radiative quantities with fine spectral resolution and, therefore, are highly accurate but computationally expensive. A number of numerical strategies have been developed to reduce computational expense but maintain accuracy in radiative transfer calculations. The correlated-k distribution is a popular method used to obtain this goal [*Goody et al.*, 1989; *Lacis and Oinas*, 1991; *Fu and Liou*, 1992; *Mlawer et al.*, 1997]. It is an efficient procedure that substantially reduces the number of calculations within a spectral interval compared to a line-by-line model without compromising accuracy. It is also conducive to calculations in inhomogeneous atmospheres in which multiple scattering due to clouds and aerosols is present.

Although the theory behind the correlated-k distribution is well established, a substantial effort is often required to implement the method for specific applications. As part of this thesis, a a FLexible Radiative Transfer Tool (FLRTT) has been developed to facilitate

the generation of correlated-k radiative transfer models, which provide accelerated calculations of radiances, fluxes, and cooling rates in inhomogeneous atmospheres without comprising accuracy. This generic tool has been used to create two new rapid radiative transfer models: RRTM_HIRS and RRTM v3.0. Applications of these models were presented in this thesis.

Satellite radiance observations are an effective tool for evaluating thermodynamic and trace gas profiles simulated by general circulation models (GCMs). For example, *Iacono et al.* [2003] evaluated upper tropospheric water vapor (UTWV) simulated by the National Center for Atmospheric Research Community Climate Model, CCM3, by comparing modeled, clear-sky brightness-temperatures to those observed from space by the High-resolution Radiation Sounder (HIRS). As part of this evaluation CCM3 was modified to utilize the rapid radiative transfer model RRTM [*Mlawer et al.*, 1997] and a separate radiance module, RRTM_HIRS, to calculate the brightness temperatures in two HIRS channels. By incorporating these accurate radiative transfer models into CCM3, the longwave radiative transfer calculations have been removed as a significant source of error in the simulations. An important result of this study is that CCM3 exhibits moist and dry discrepancies in UTWV of 50% or more in particular climatic zones, which may be attributed to errors in the CCM3 dynamical schemes.

RRTM v3.0 is a correlated-k longwave radiative transfer model with 16 spectral bands. The speed of execution and the accurate flux and heating rate calculations of RRTM v3.0 make it an excellent candidate for inclusion into GCMs and numerical weather prediction models (NWPs). RRTM v3.0 is an update of RRTM v2.3 [*Mlawer et al.*, 1997], but has a number of significant algorithm changes as well as absorption coefficients derived from newer line parameters. For a set of 42 diverse atmospheres, the fluxes calculated by RRTM v3.0 agree with those computed by LBLRTM to within 1.0 W m^{-2} at all levels, and the computed cooling rates agree to within 0.1 K day^{-1} in the troposphere and 0.3 K day^{-1} in the stratosphere. Other notable changes between RRTM v2.3 and RRTM v3.0 are improved stratospheric cooling rates, as well as improved flux and cooling rates for atmospheres with trace gas abundances substantially different from modern-day atmospheres.

RRTM v3.0 is part of a suite of radiative transfer models which has been developed at Atmospheric and Environmental Research, Inc. (AER) over the last decade. The devel-

opment of RRTM v3.0 was sponsored by the Department of Energy Atmospheric Radiation Measurement Program. RRTM v3.0 is available to the scientific community on the AER,Inc. web-site (http://rtweb.aer.com).

Finally, an examination of clear-sky longwave radiative transfer at the Atmospheric Radiation Measurement Program's North Slope of Alaska Cloud and Radiation Testbed (NSA CART) site was undertaken. The goal of this research was to evaluate current longwave radiation measurement and modeling capabilities in a climatically-extreme environment, such as the North Slope of Alaska. A number of clear sky time periods from the 2001 annual cycle have been utilized to simultaneously address the specification of the atmospheric state, longwave radiometric measurements, and radiative transfer calculations at the NSA CART site. Consistent with findings from other radiation measurement and observation intercomparisons [*Clough et al.*, 2000; *Tobin et al.*, 2000; *Marty et al.*, 2003], the specification of the atmospheric water vapor and ozone profile are two large sources of uncertainty in modeled radiances and fluxes. Improvements in the specification of carbon dioxide optical depths within LBLRTM resulted, in part, from the NSA CART site observation and model intercomparison.

6.2 Future Work

Overall, the scientific community's ability to both model and observe longwave radiation is strong. This thesis demonstrates that this ability has not faltered even in the cold, dry conditions of the arctic. While clear-sky longwave radiative transfer is certainly an important topic, it is only part of the total global radiative energy budget.

6.2.1 Rapid Models for the Shortwave Spectral Regime

It was noted in the thesis introduction that the InterComparison of Radiation Codes in Climate Models demonstrated significant variability in flux calculations when operating on the same atmospheric profile. This is true not only for the longwave but also the shortwave spectral region. A recent intercomparison of 25 1-dimensional solar radiative transfer codes (ICRCCM-III) [*Barker et al.*, 2002] demonstrated that most 1-dimensional codes typically underestimate atmospheric absorption by 15-25 W m^{-2} at overhead sun for a

tropical atmosphere, regardless of clouds. AER, Inc. has a shortwave line-by-line radiative transfer model (LBLRTM/CHARTS [*Moncet and Clough*, 1997]) which has been extensively compared to high-quality spectral surface irradiance measurements [*Mlawer et al.*, 2000]. As a result of these extensive validations, LBLRTM/CHARTS was used as a benchmark model in the ICRCCM-III intercomparison. A rapid correlated-k shortwave radiative transfer model (RRTM_SW) was developed to calculate fluxes and cooling rates consistent with LBLRTM/CHARTS [*Mlawer and Clough*, 1996].

As is true for the longwave spectral region a substantial effort is often required to implement the correlated-k method for specific applications; therefore, a future goal is to extend FLRTT to produce k distributions and generic radiation codes for the shortwave which are consistent with CHARTS and RRTM_SW. Two significant updates to FLRTT are required to achieve this: a) Rayleigh scattering and the solar source function must be incorporated, just as the Planck function is included in the longwave version of FLRTT, and b) a scattering radiative transfer algorithm must be included to account for Rayleigh scattering, and scattering by other particles such as aerosols or clouds.

6.2.2 Rapid Models for Cloudy and Aerosol-Loaded Atmospheres

RRTM and RRTM_SW both include popular ice and liquid cloud optical property parameterizations, appropriately averaged for each spectral band, thereby allowing them to calculate fluxes for cloudy atmospheres. A future addition to FLRTT will be the implementation of a routine which calculates and stores cloud optical properties for any size spectral band. As a first estimate the cloud properties could be considered constant over the band, which may be a good approximation if the spectral band is not too wide. However, if the band is too wide, the correlated-k method mapping $\nu \rightarrow g$ must be considered in determining the cloud optical properties for each subinterval j.

RRTM_SW includes an option to include the radiative effects of aerosols. Aerosols are extremely important in the shortwave, and are increasingly recognized as contributors to longwave radiative transfer. It is planned to add an aerosol option both to RRTM and potentially to a FLRTT-generated model as well.

Proper treatment of clouds in either the shortwave or the longwave require require solving the radiative transfer equation in the presence of multiple-scattering. RRTM_SW

includes the scattering radiative transfer algorithm, DISORT [*Stamnes et al.*, 1988], but the current longwave code, RRTM v3.0, does not. The next release of RRTM will contain an option to use DISORT to solve the radiative transfer equation.

6.2.3 Extending the Closure Analysis at NSA

The closure analysis described in Chapter 5 was presented for only clear-sky longwave radiative transfer, and for only 17 cases. However, the NSA site has been operational for several years, and a large volume of radiometric and cloud observation data has been collected. A future goal is an extensive closure analysis at NSA which utilizes the dataset collected at the site over the last several years in combination with modeled radiances and fluxes. A dataset of the vertical profile of cloud microphysical properties over the NSA CART site is being generated by a suite of retrieval algorithms at the NOAA Environmental Technology Laboratory, and would be an essential component in such a study. The proposed future research would cover the entire radiative regime, thermal and solar, contributing to the radiative energy balance. Such a multi-year data set would be a resource for the research community to evaluate new parameterizations, new cloud property retrievals both from satellites and ground-based measurements, and arctic regional climate models. It would also provide valuable statistics about the interaction between cloud fields and radiation in the arctic.

Appendix A

Summary of Updates to RRTM v3.0

- The line parameters were obtained from HITRAN 1996 database [*Rothman et al.*, 1998]. The water vapor lines in the HITRAN 1996 database in the spectral range of 500 to 2880 cm^{-1} were replaced with water vapor line parameters measured by Dr. Bob Toth at the Jet Propulsion Laboratory (personal communication to AER, Inc.). These parameters for water vapor are consistent with the HITRAN 2000 database. Line coupling coefficients have been utilized for the important Q-branches of carbon dioxide. These line coupling coefficients have been updated for consistency with the HITRAN 1996 carbon dioxide line strengths.

- The water vapor continuum absorption coefficients were obtained from CKD 2.4. Note that contributions to the optical depth from both the self and foreign water vapor continuum are explicitly calculated in RRTM v3.0. Continuum contributions from nitrogen and oxygen are also included.

- RRTM calculates fluxes and cooling rates in the longwave spectral region (from 10 to 3250 cm^{-1}. In the previous version, RRTM v2.3, the spectral region extended only to 3000 cm^{-1}.

- The errors in computed stratospheric cooling rates have been substantially reduced. In RRTM v3.0 the average maximum stratospheric cooling rate error (for a representative set of 42 atmospheric profiles) is 0.27 K day^{-1}, compared with an average error of 0.53 K day^{-1} for RRTM v2.3.

- The fluxes and cooling rates computed in RRTM v3.0 are greatly improved for atmospheres having abundances of trace gases (e.g. CO2, CH4) substantially different from current abundances.
- Capability to input atmospheric profile on either altitude or pressure grid, and to output quantities on either altitude or pressure grid.
- The source function in each layer is now computed using the exact 'linear in tau' approach, in contrast to the use of a Pade approximant in RRTM v2.3. Both the exponential function and the exact 'linear in tau' function are tabulated at 5000 values and a table lookup is used in the radiative transfer calculation. It should be noted that this adds a small element of discreteness into the calculation. (This methodology is consistent with LBLRTM)
- Cloudy-sky radiative transfer calculations include options:
  - Radiative transfer algorithms for cloudy layers with random or maximum/random overlap.
  - Liquid water cloud optical properties parameterization option: *Hu and Stamnes* [1993]
  - Ice cloud optical properties parameterization options: *Ebert and Curry* [1992] and*Fu et al.* [1998].
- The instruction manual has been updated. It includes important changes to many options, such as the number of angles used in the flux calculations, the declaration of either random or maximum/random cloud overlap assumption etc.

Figure A.1 through Figure A.17 show the band-by-band flux and cooling rate residuals between both RRTM v2.3 and RRTM v3.0 and LBLRTM v6.01 for 42 atmospheric profiles [*Garand et al.*, 2001]. Residual quantities plotted are the upward flux at the top of the atmosphere, the downward flux at the surface, the maximum net flux residual at any altitude, and the maximum tropospheric and stratospheric cooling rate error. The mean of the absolute value of the profile residuals are also quantified on the bottom, right panel of each figure.

Figures A.1, A.2, and A.17 (corresponding to band 1, 2, and 16) do not display the RRTM v2.3 results, since the spectral bandwidths have changed between the two versions. Since band 1 and band 2 are important, Figure A.3 shows the residuals, summed for band 1 and band 2.

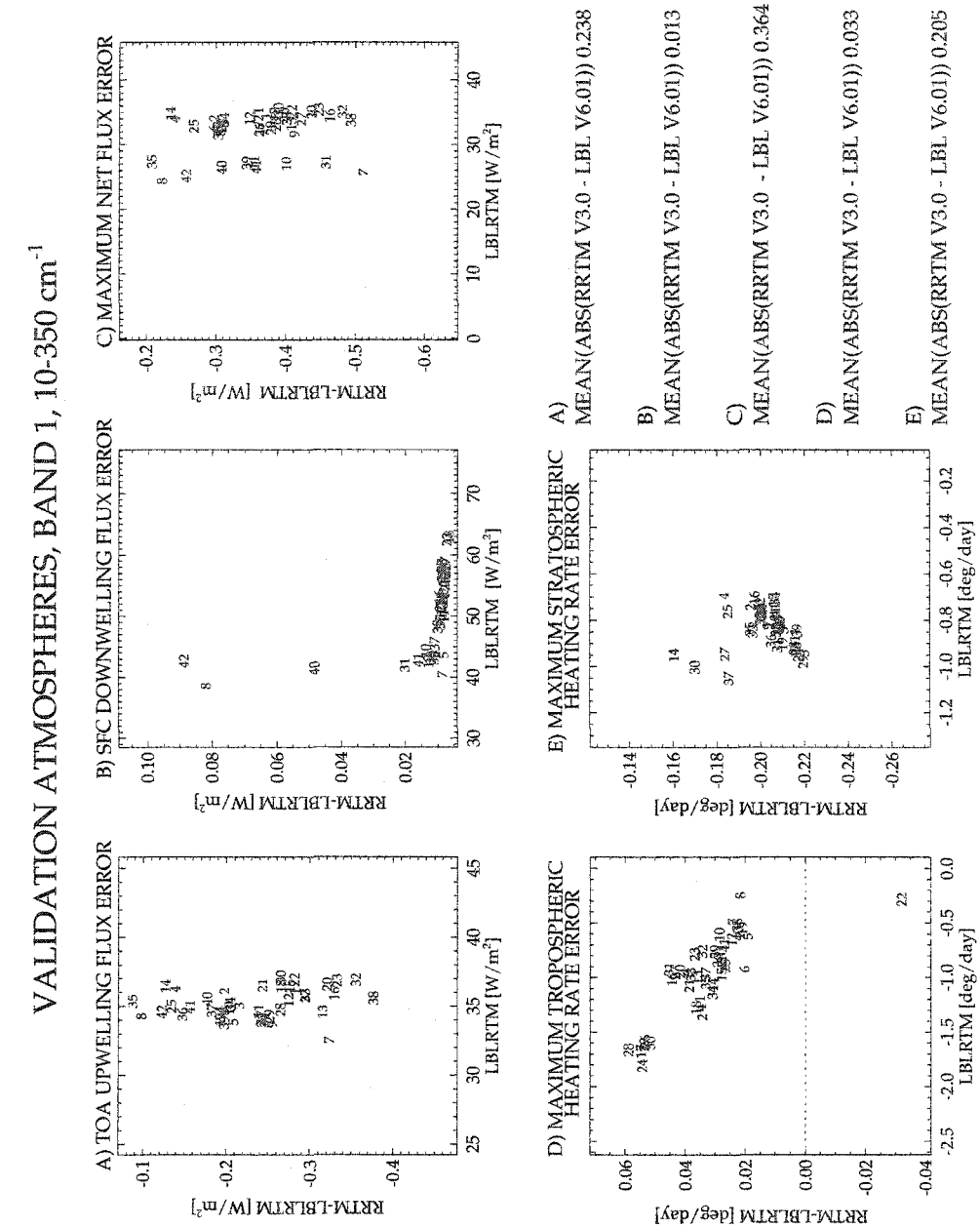

Figure A.1. Band 1 RRTM residuals for *Garand et al.* [2001] atmospheres. Band 1 (10-350 cm^{-1}) differences between RRTM and LBLRTM for 42 atmospheric profiles for a) upward flux at the top of the atmosphere, b) downward flux at the surface, and the maximum residual in in c) net flux, d) tropospheric cooling rate, and e) stratospheric cooling rate plotted as a logarithmic function of pressure.

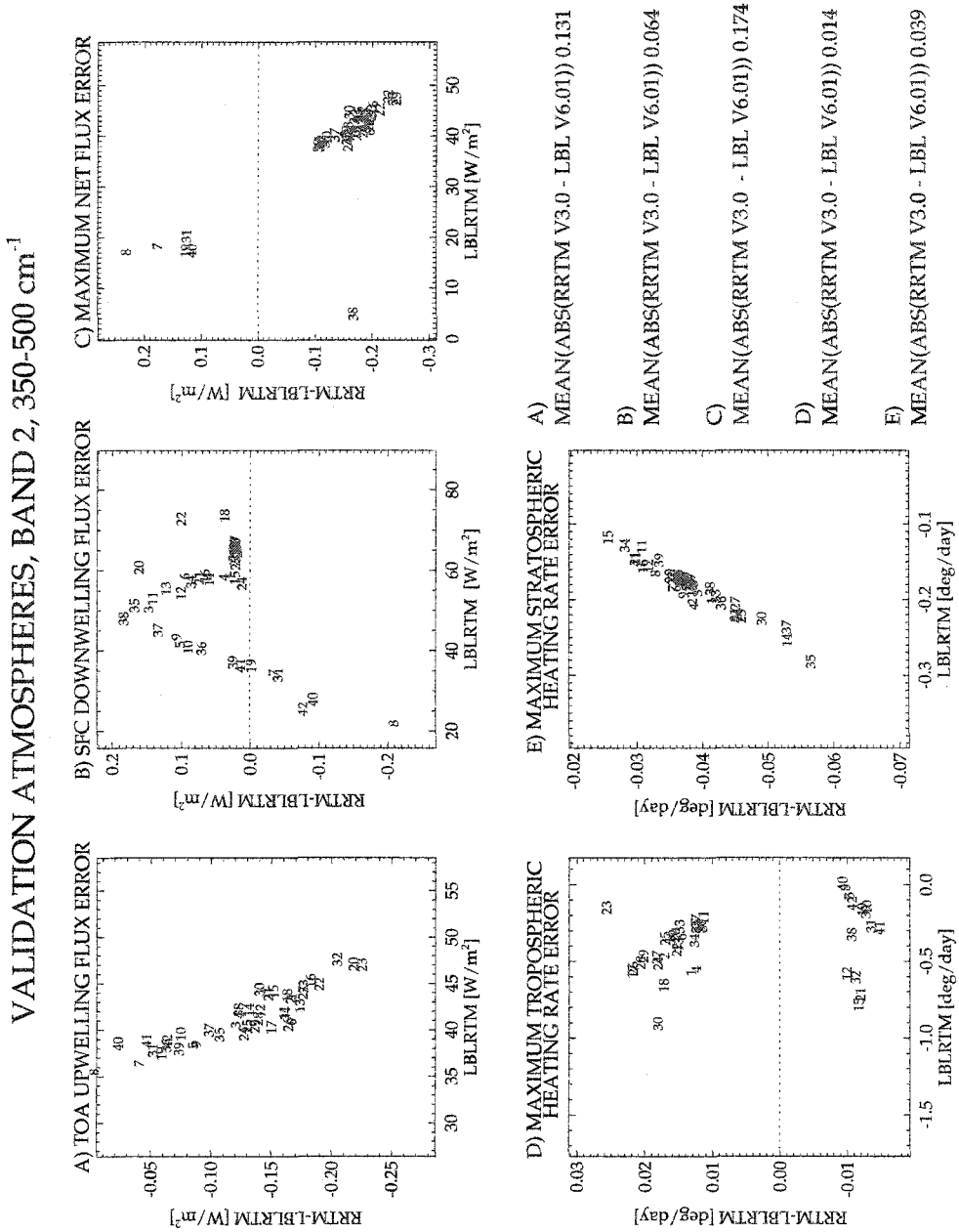

Figure A.2. Band 2 RRTM residuals for *Garand et al.* [2001] atmospheres. Band 2 (350-500 cm^{-1}) differences between RRTM and LBLRTM for 42 atmospheric profiles for a) upward flux at the top of the atmosphere, b) downward flux at the surface, and the maximum residual in in c) net flux, d) tropospheric cooling rate, and e) stratospheric cooling rate plotted as a logarithmic function of pressure.

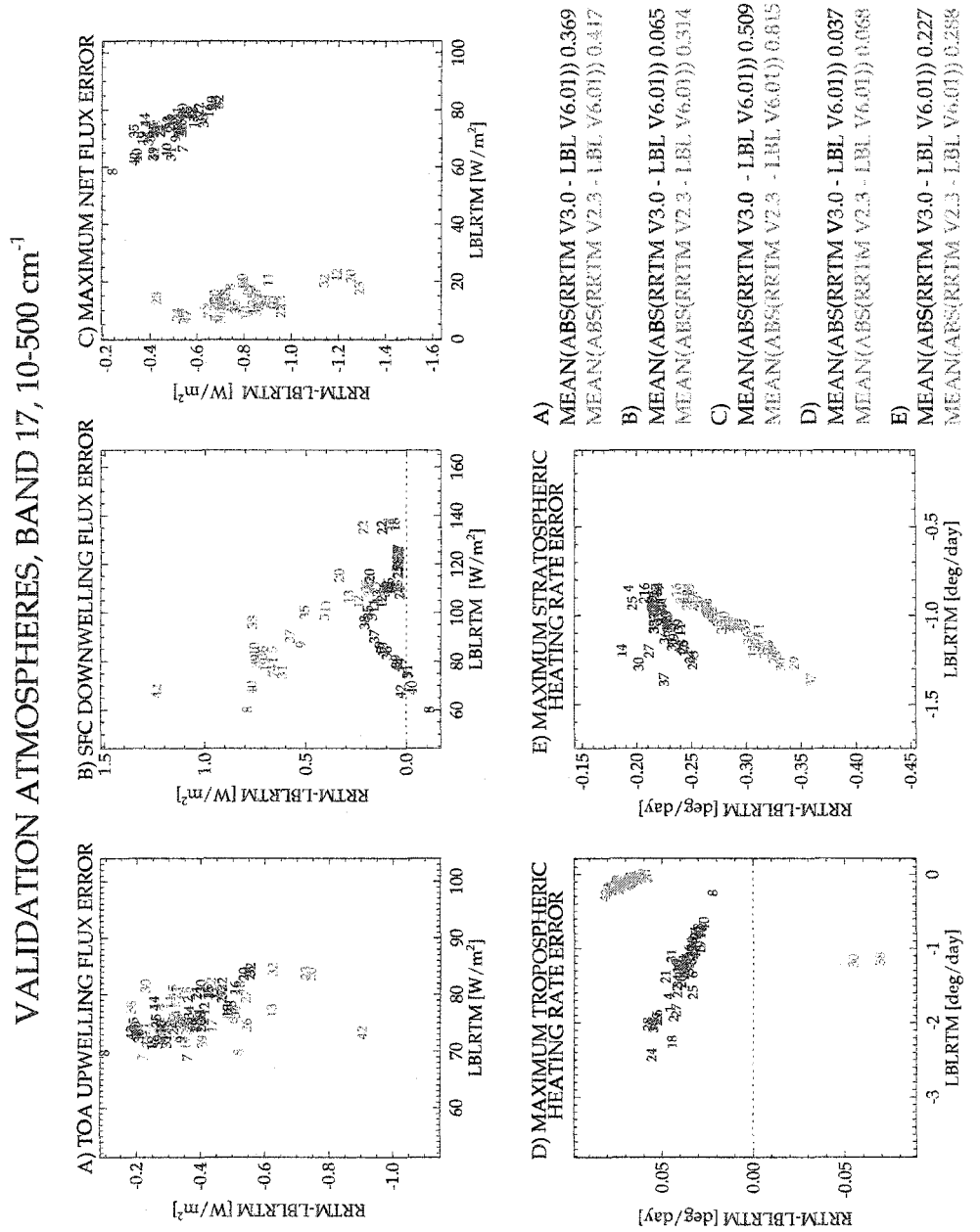

Figure A.3. Band 1 and 2 RRTM residuals for *Garand et al.* [2001] atmospheres. Band 1 and 2 (10-500 cm^{-1}) differences between RRTM and LBLRTM for 42 atmospheric profiles for a) upward flux at the top of the atmosphere, b) downward flux at the surface, and the maximum residual in in c) net flux, d) tropospheric cooling rate, and e) stratospheric cooling rate plotted as a logarithmic function of pressure.

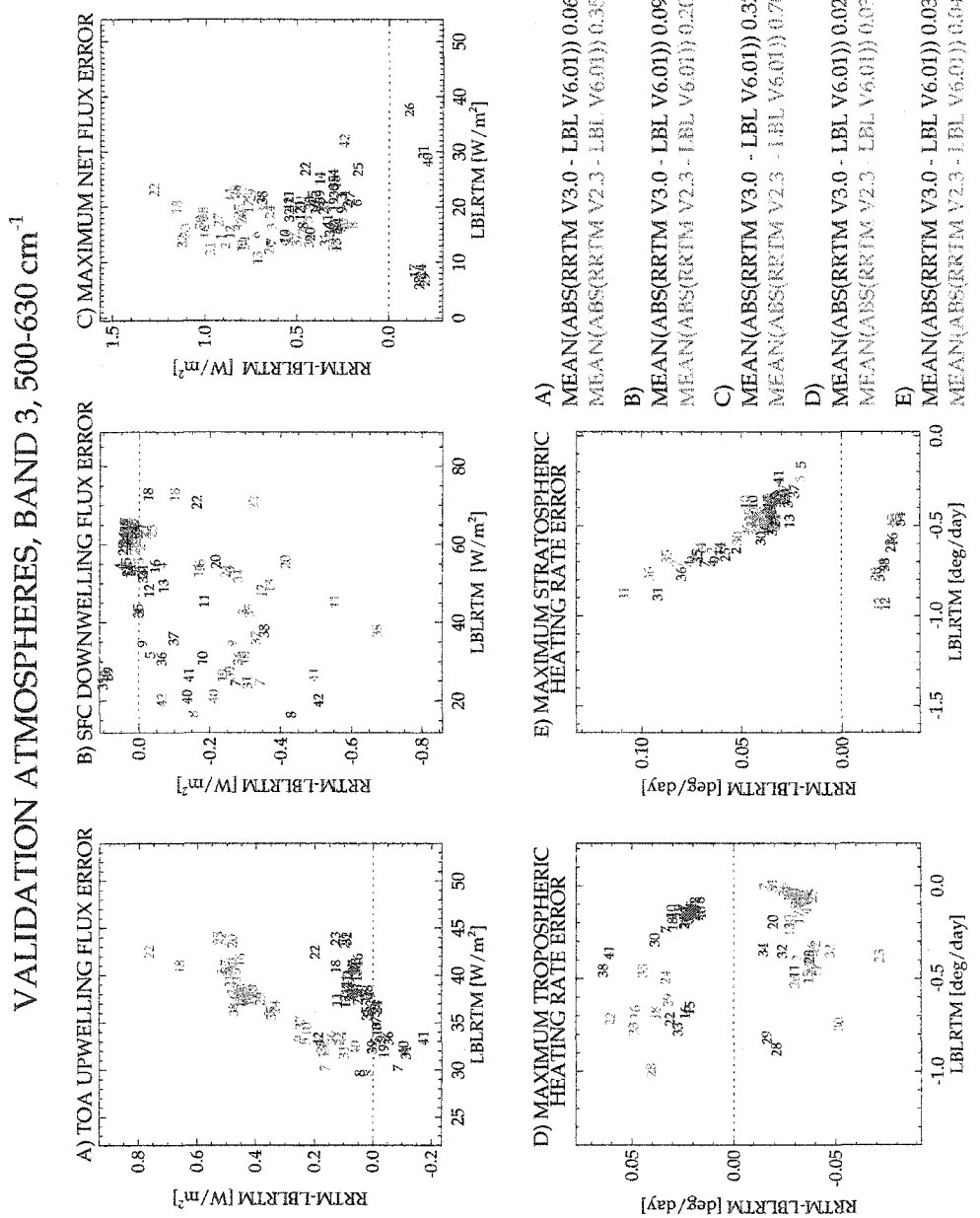

Figure A.4. Band 3 RRTM residuals for *Garand et al.* [2001] atmospheres. Band 3 (500-630 cm^{-1}) differences between RRTM and LBLRTM for 42 atmospheric profiles for a) upward flux at the top of the atmosphere, b) downward flux at the surface, and the maximum residual in in c) net flux, d) tropospheric cooling rate, and e) stratospheric cooling rate plotted as a logarithmic function of pressure.

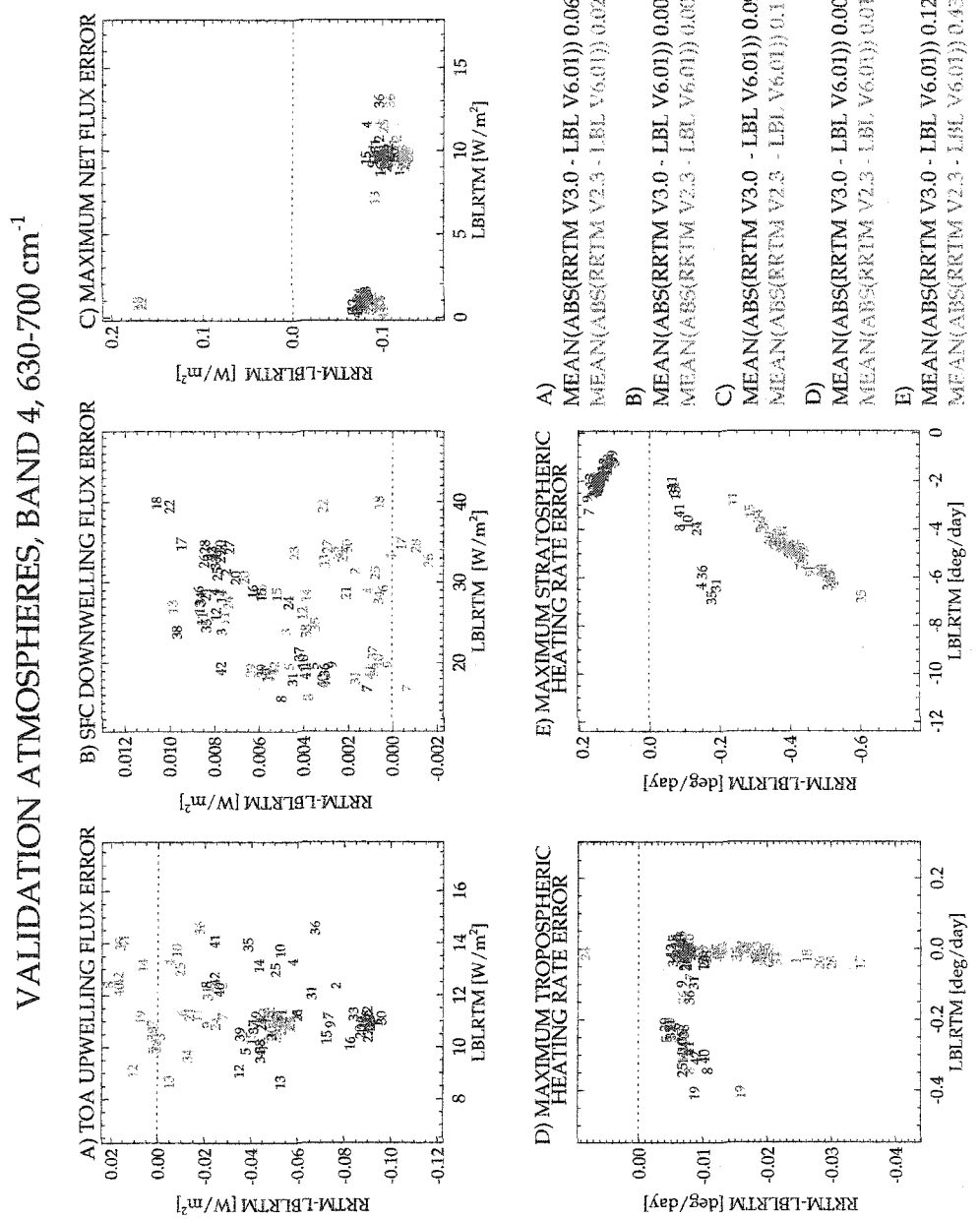

Figure A.5. Band 4 RRTM residuals for *Garand et al.* [2001] atmospheres. Band 4 (630-700 cm^{-1}) differences between RRTM and LBLRTM for 42 atmospheric profiles for a) upward flux at the top of the atmosphere, b) downward flux at the surface, and the maximum residual in in c) net flux, d) tropospheric cooling rate, and e) stratospheric cooling rate plotted as a logarithmic function of pressure.

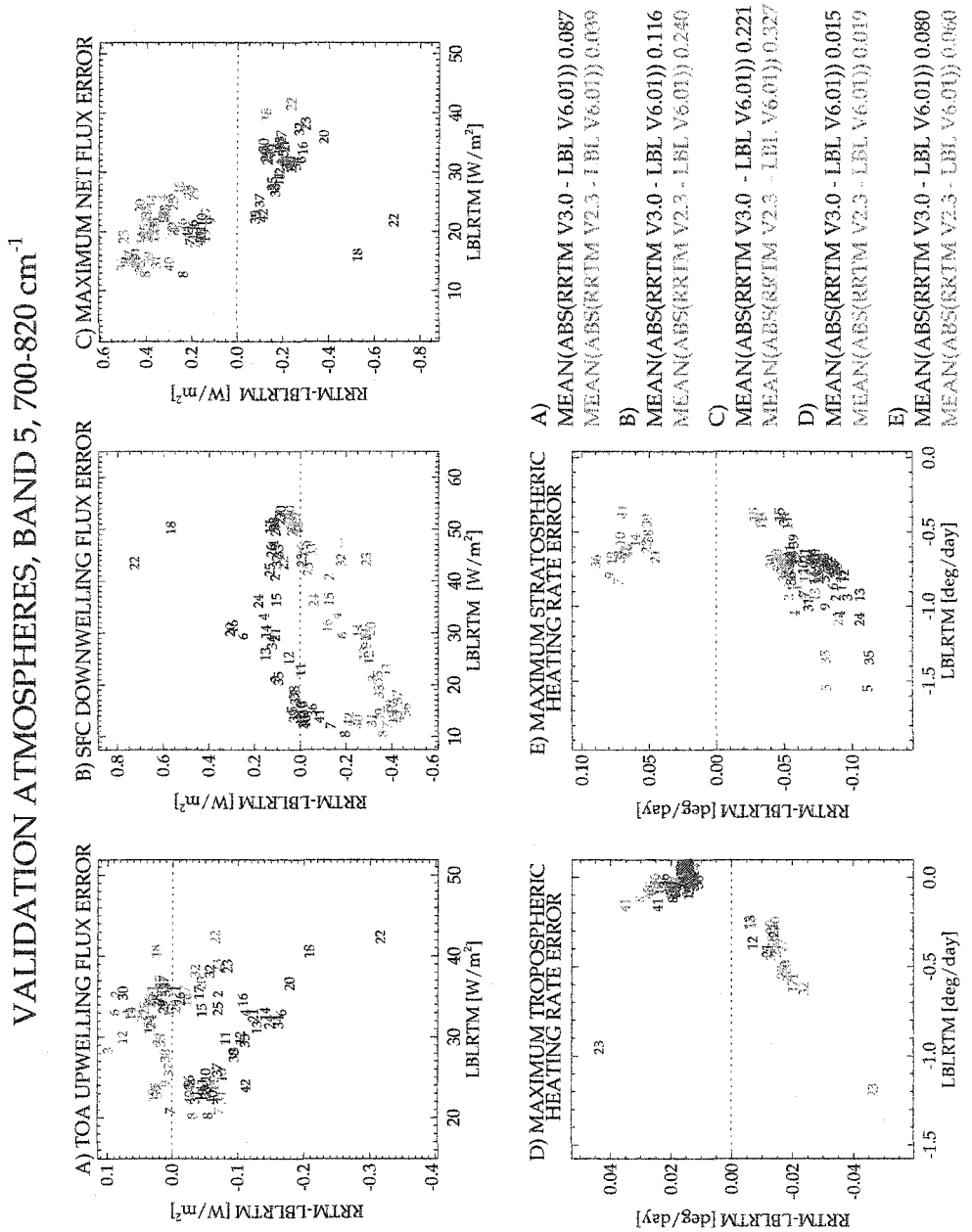

Figure A.6. Band 5 RRTM residuals for *Garand et al.* [2001] atmospheres. Band 5 (700-820 cm^{-1}) differences between RRTM and LBLRTM for 42 atmospheric profiles for a) upward flux at the top of the atmosphere, b) downward flux at the surface, and the maximum residual in in c) net flux, d) tropospheric cooling rate, and e) stratospheric cooling rate plotted as a logarithmic function of pressure.

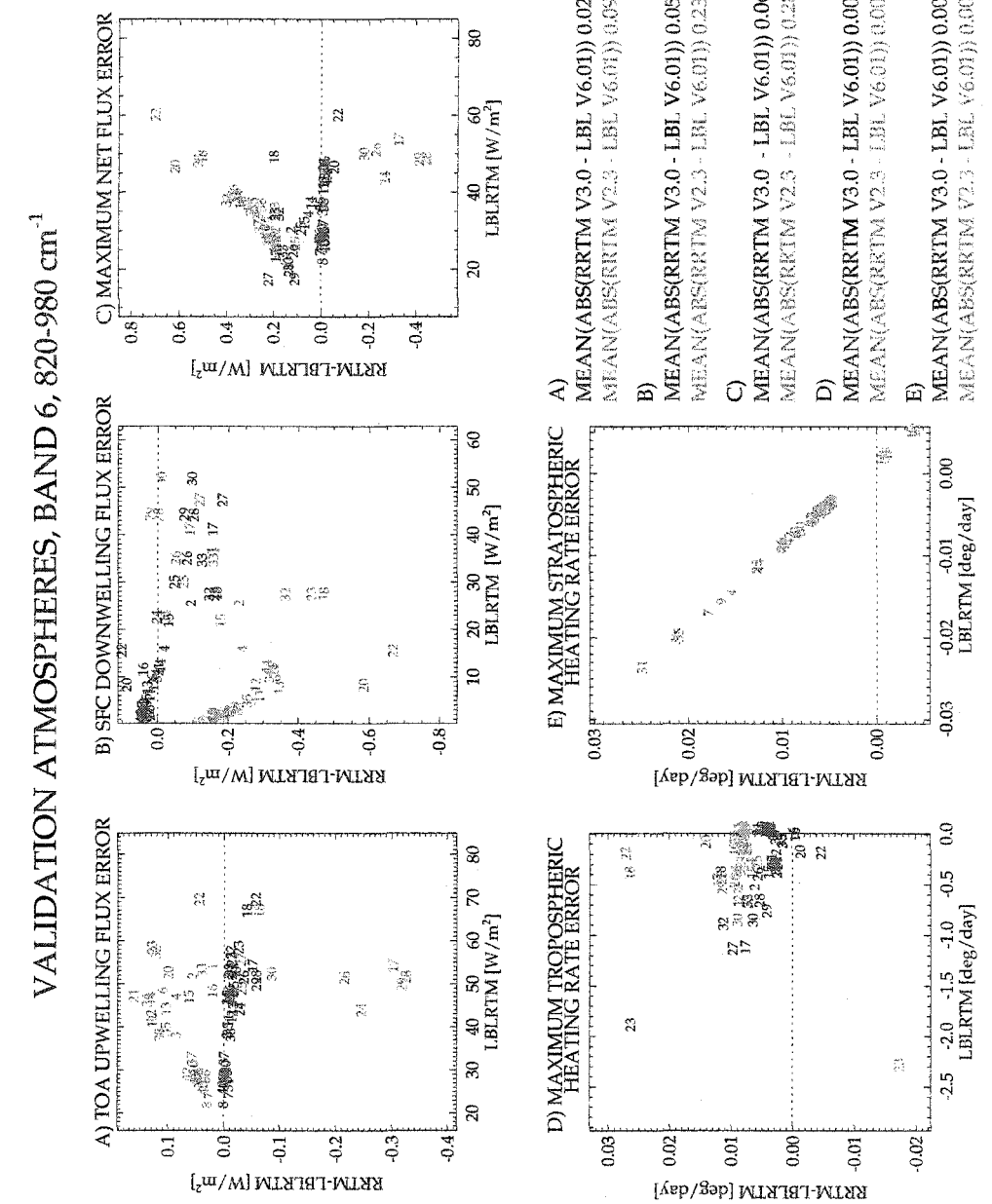

Figure A.7. Band 6 RRTM residuals for *Garand et al.* [2001] atmospheres. Band 6 (820-980 cm^{-1}) differences between RRTM and LBLRTM for 42 atmospheric profiles for a) upward flux at the top of the atmosphere, b) downward flux at the surface, and the maximum residual in in c) net flux, d) tropospheric cooling rate, and e) stratospheric cooling rate plotted as a logarithmic function of pressure.

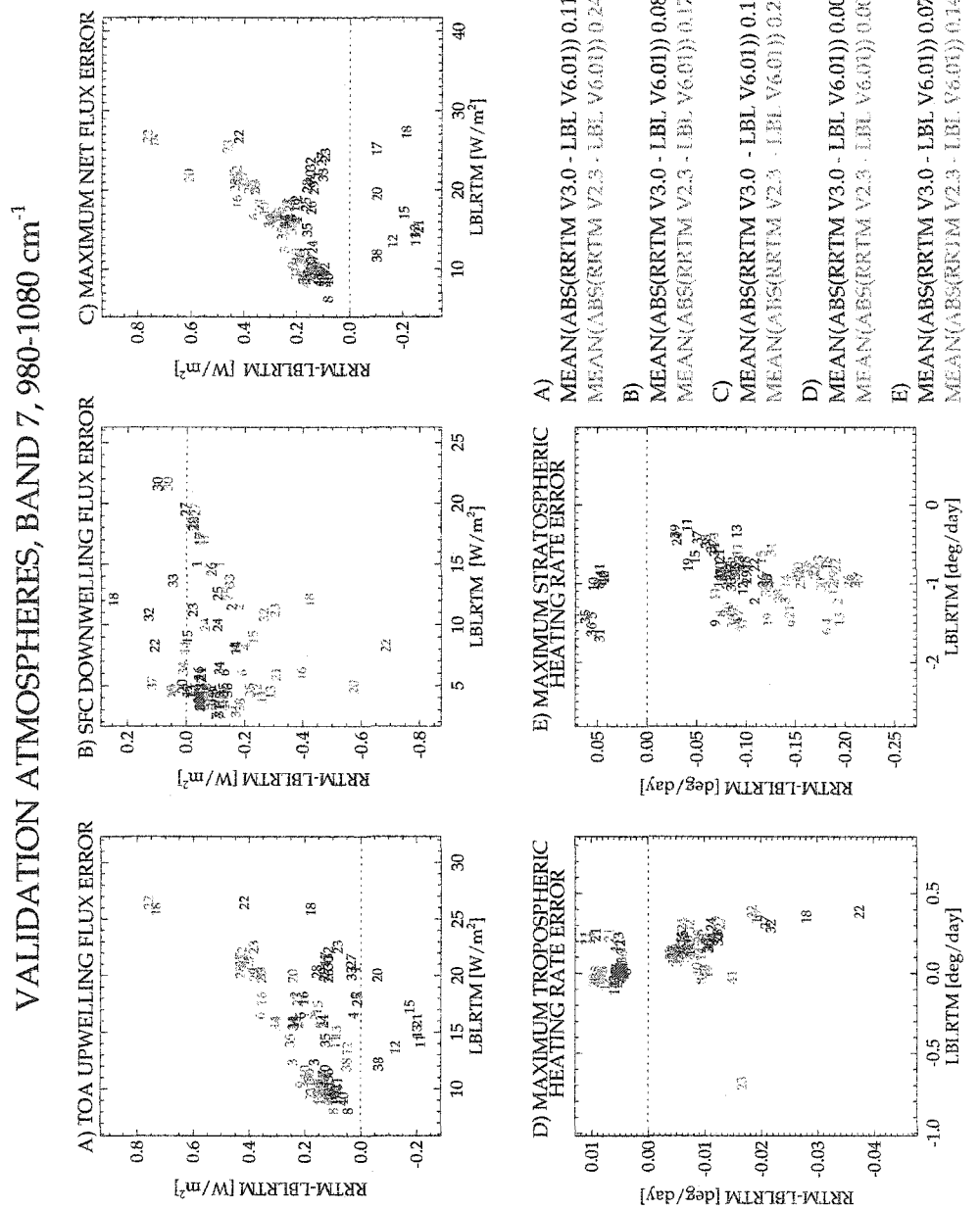

Figure A.8. Band 7 RRTM residuals for *Garand et al.* [2001] atmospheres. Band 7 (980-1080 cm^{-1}) differences between RRTM and LBLRTM for 42 atmospheric profiles for a) upward flux at the top of the atmosphere, b) downward flux at the surface, and the maximum residual in in c) net flux, d) tropospheric cooling rate, and e) stratospheric cooling rate plotted as a logarithmic function of pressure.

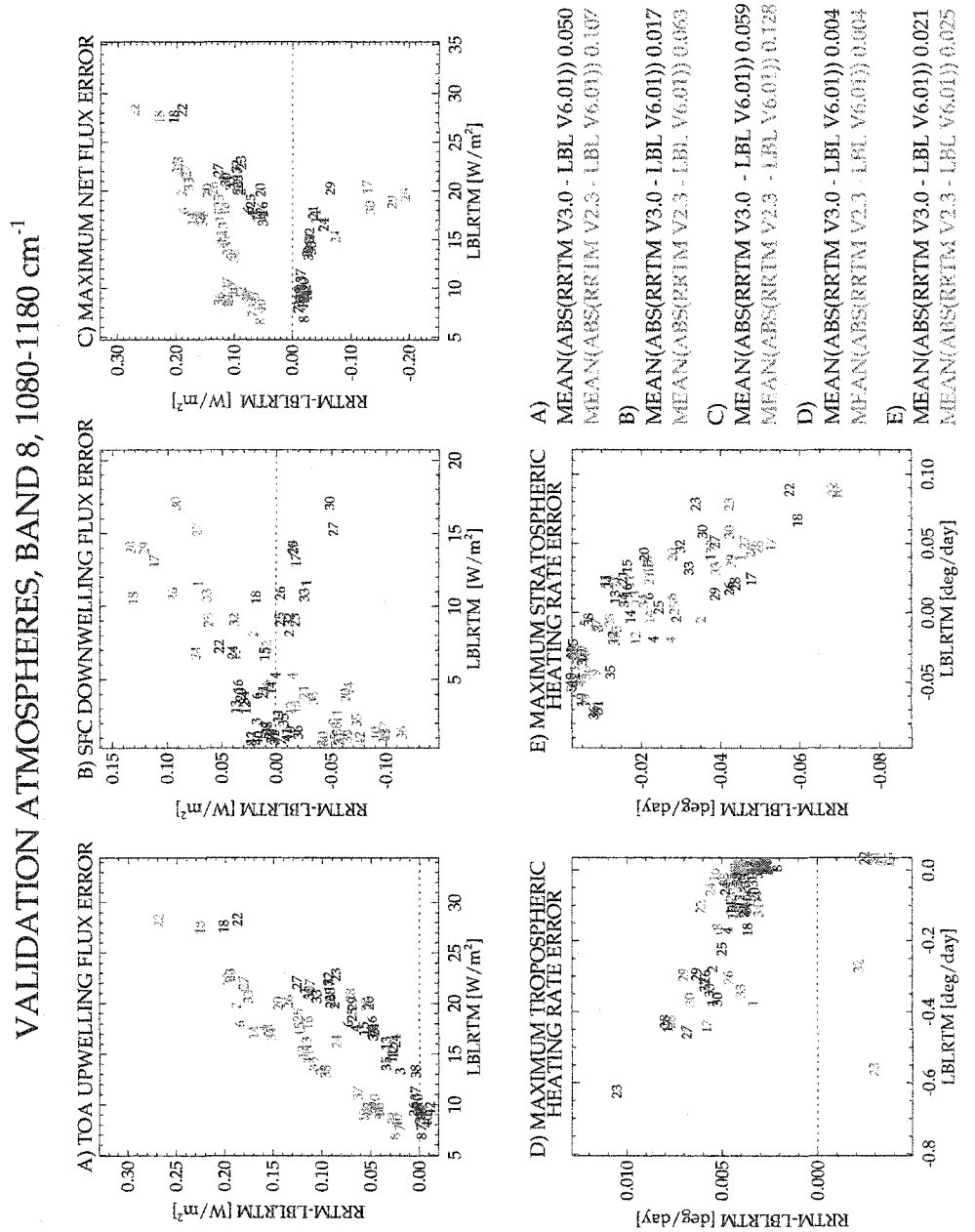

Figure A.9. Band 8 RRTM residuals for *Garand et al.* [2001] atmospheres. Band 8 (1080-1180 cm^{-1}) differences between RRTM and LBLRTM for 42 atmospheric profiles for a) upward flux at the top of the atmosphere, b) downward flux at the surface, and the maximum residual in in c) net flux, d) tropospheric cooling rate, and e) stratospheric cooling rate plotted as a logarithmic function of pressure.

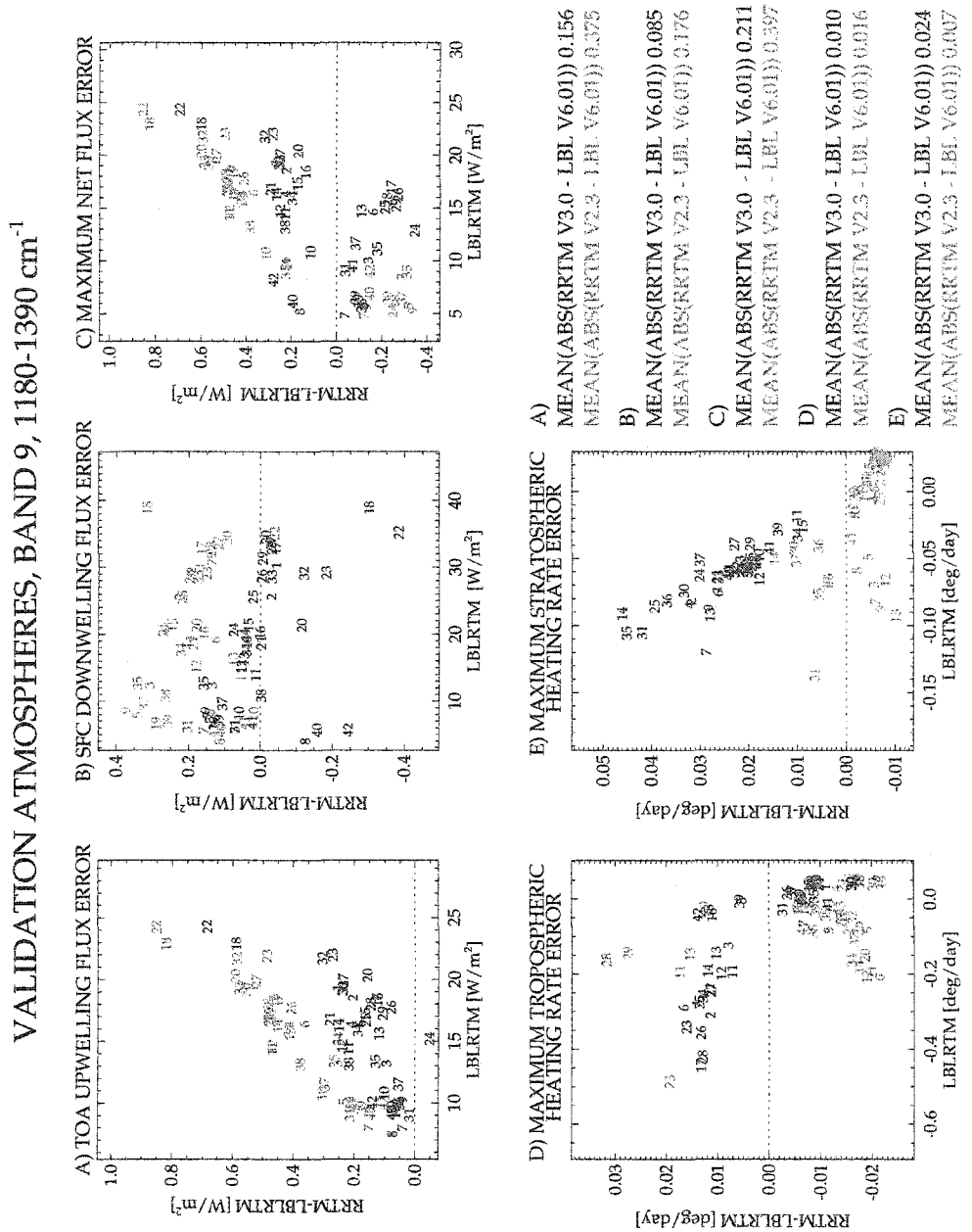

Figure A.10. Band 9 RRTM residuals for *Garand et al.* [2001] atmospheres. Band 9 (1180-1390 cm^{-1}) differences between RRTM and LBLRTM for 42 atmospheric profiles for a) upward flux at the top of the atmosphere, b) downward flux at the surface, and the maximum residual in in c) net flux, d) tropospheric cooling rate, and e) stratospheric cooling rate plotted as a logarithmic function of pressure.

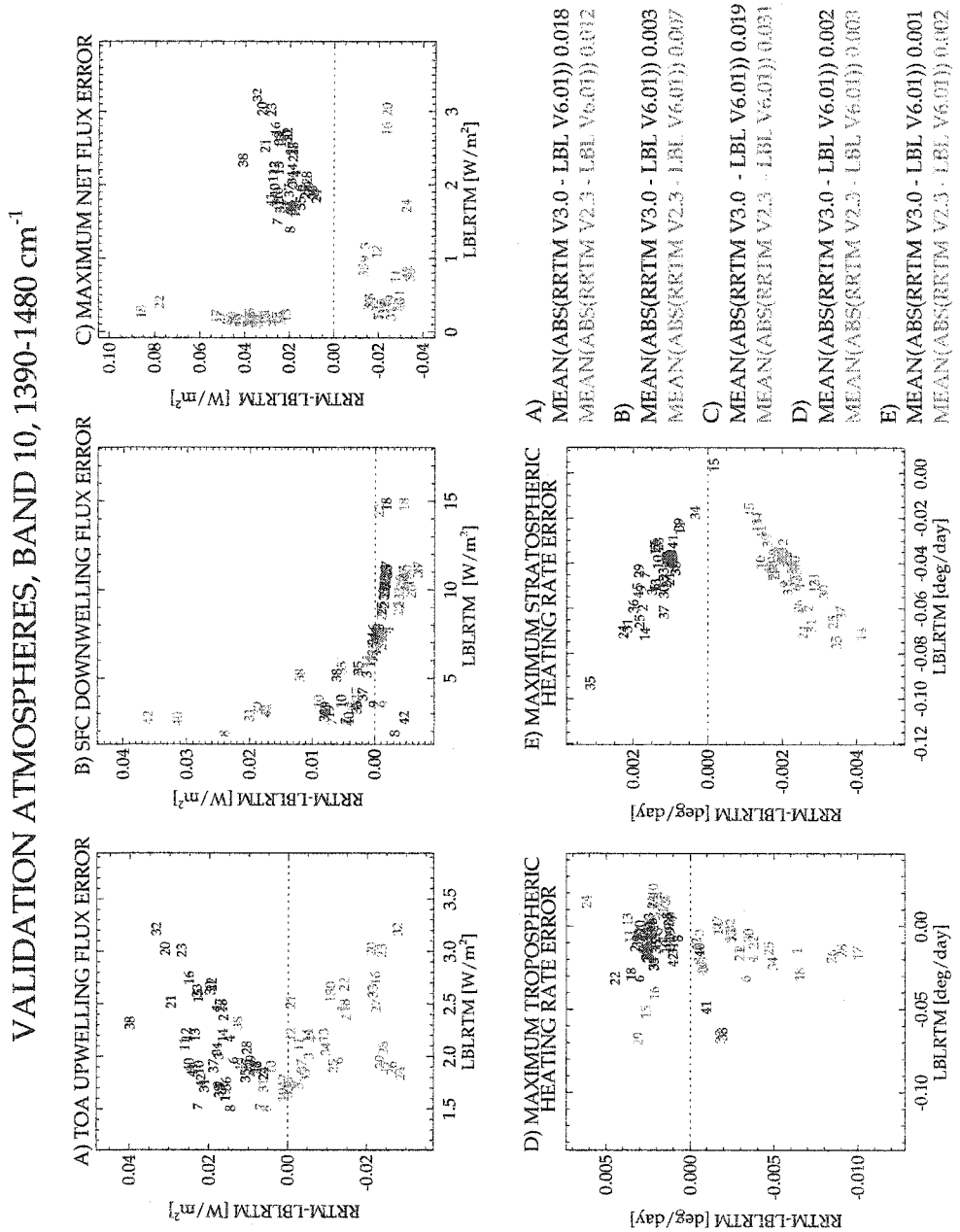

Figure A.11. Band 10 RRTM residuals for *Garand et al.* [2001] atmospheres. Band 10 (1390-1480 cm^{-1}) differences between RRTM and LBLRTM for 42 atmospheric profiles for a) upward flux at the top of the atmosphere, b) downward flux at the surface, and the maximum residual in in c) net flux, d) tropospheric cooling rate, and e) stratospheric cooling rate plotted as a logarithmic function of pressure.

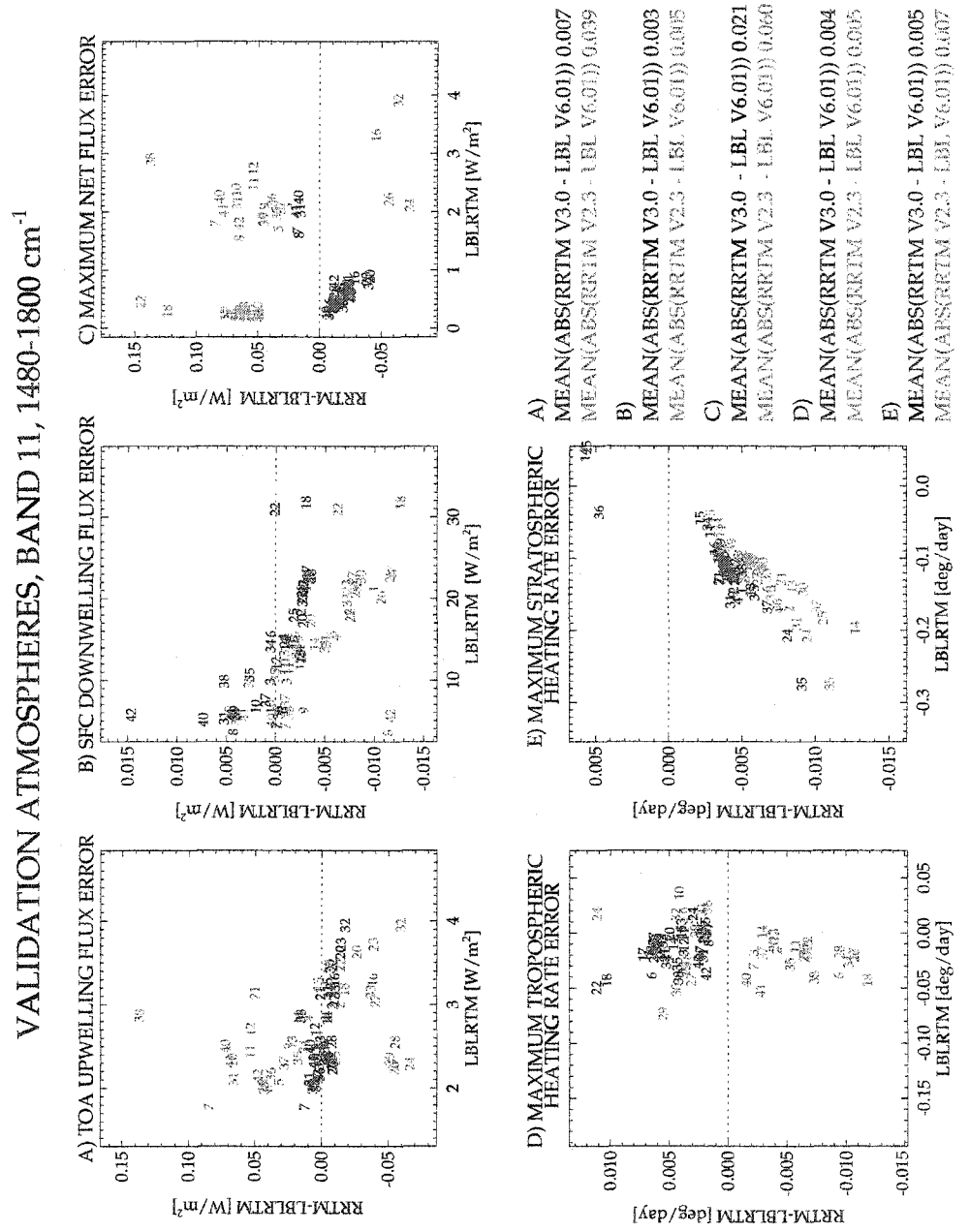

Figure A.12. Band 11 RRTM residuals for *Garand et al.* [2001] atmospheres. Band 11 (1480-1800 cm^{-1}) differences between RRTM and LBLRTM for 42 atmospheric profiles for a) upward flux at the top of the atmosphere, b) downward flux at the surface, and the maximum residual in in c) net flux, d) tropospheric cooling rate, and e) stratospheric cooling rate plotted as a logarithmic function of pressure.

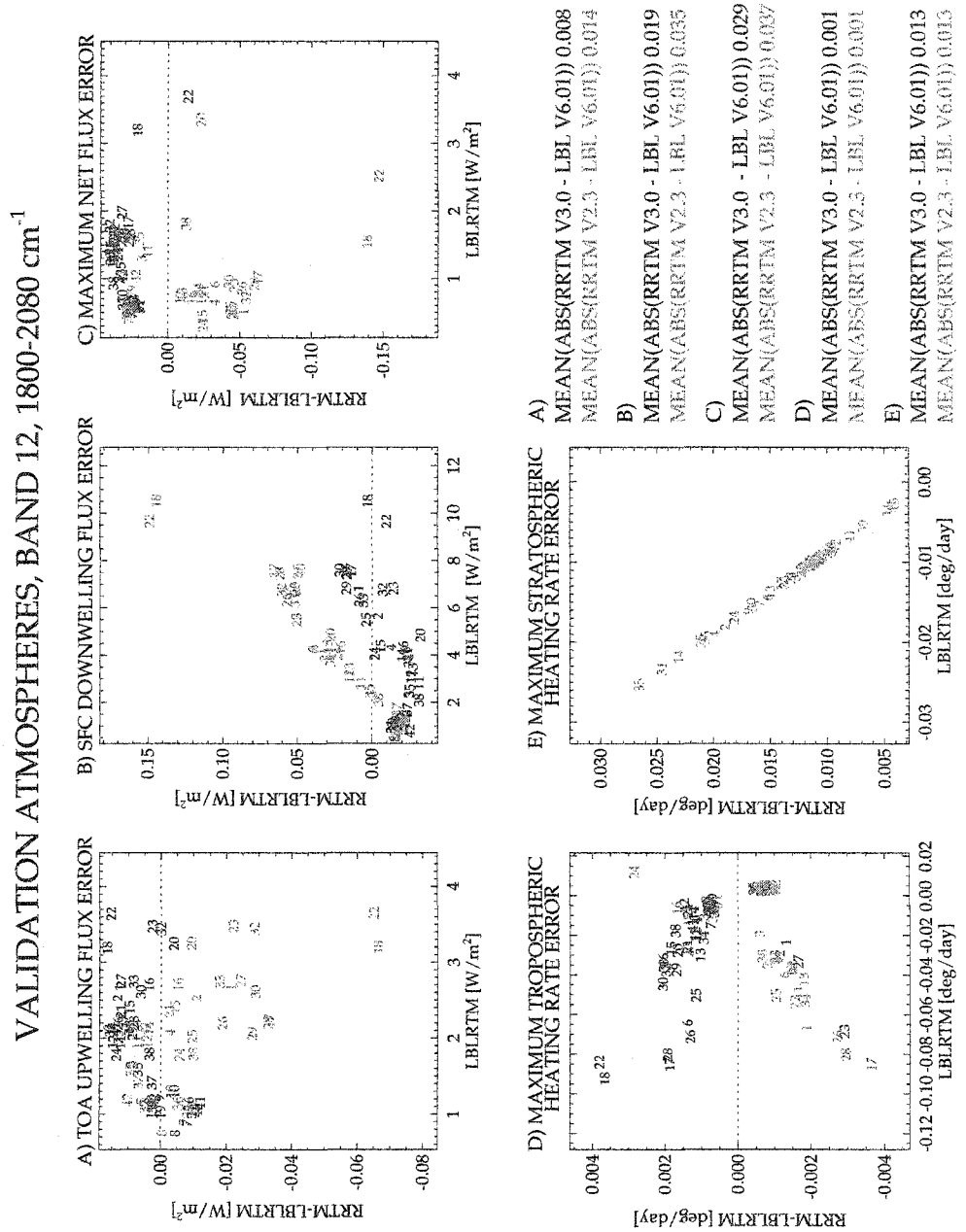

Figure A.13. Band 12 RRTM residuals for *Garand et al.* [2001] atmospheres. Band 12 (1800-2080 cm^{-1}) differences between RRTM and LBLRTM for 42 atmospheric profiles for a) upward flux at the top of the atmosphere, b) downward flux at the surface, and the maximum residual in in c) net flux, d) tropospheric cooling rate, and e) stratospheric cooling rate plotted as a logarithmic function of pressure.

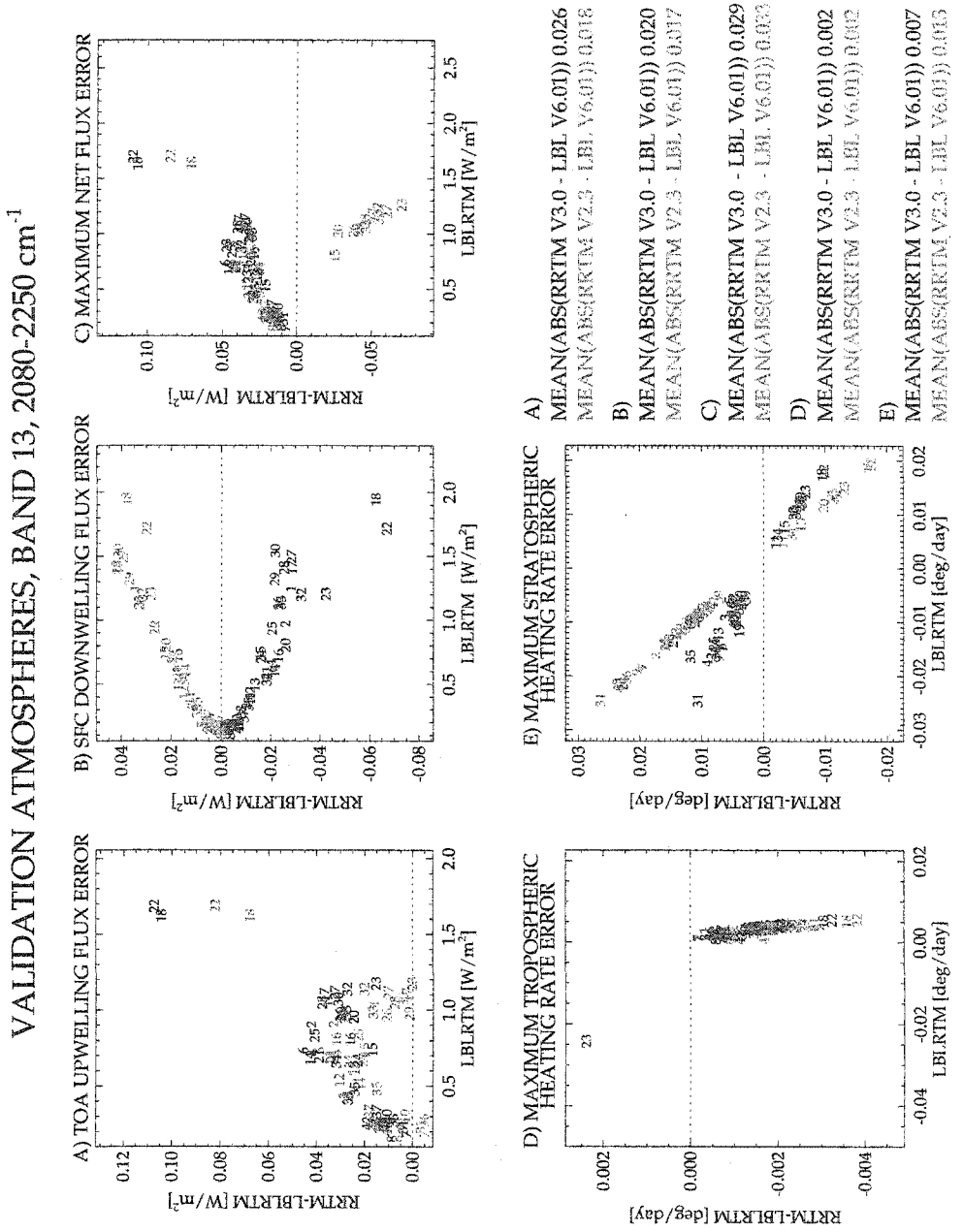

Figure A.14. Band 13 RRTM residuals for *Garand et al.* [2001] atmospheres. Band 13 (2080-2250 cm^{-1}) differences between RRTM and LBLRTM for 42 atmospheric profiles for a) upward flux at the top of the atmosphere, b) downward flux at the surface, and the maximum residual in in c) net flux, d) tropospheric cooling rate, and e) stratospheric cooling rate plotted as a logarithmic function of pressure.

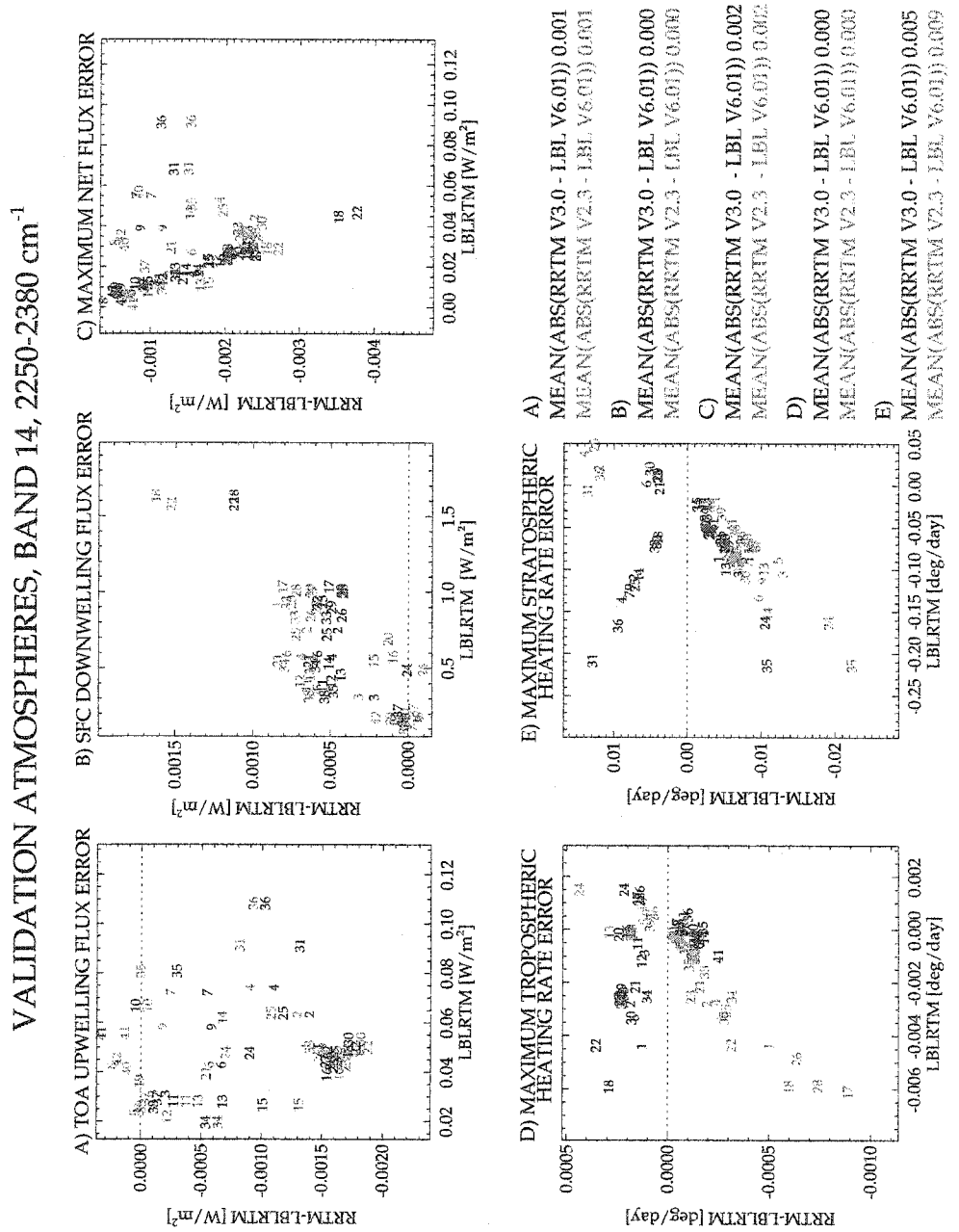

Figure A.15. Band 14 RRTM residuals for *Garand et al.* [2001] atmospheres. Band 14 (2250-2380 cm^{-1}) differences between RRTM and LBLRTM for 42 atmospheric profiles for a) upward flux at the top of the atmosphere, b) downward flux at the surface, and the maximum residual in in c) net flux, d) tropospheric cooling rate, and e) stratospheric cooling rate plotted as a logarithmic function of pressure.

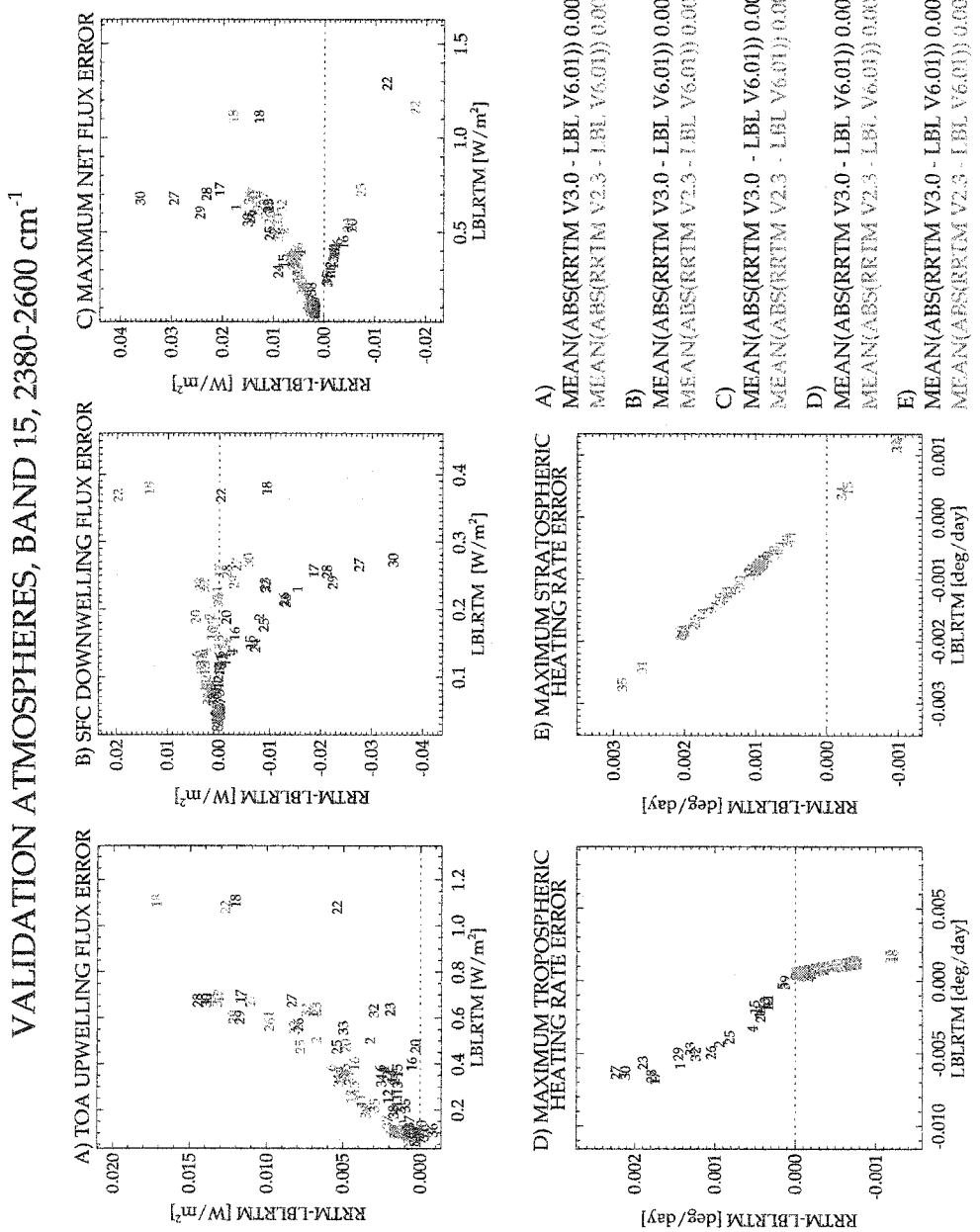

Figure A.16. Band 15 RRTM residuals for *Garand et al.* [2001] atmospheres. Band 15 (2380-2600 cm^{-1}) differences between RRTM and LBLRTM for 42 atmospheric profiles for a) upward flux at the top of the atmosphere, b) downward flux at the surface, and the maximum residual in in c) net flux, d) tropospheric cooling rate, and e) stratospheric cooling rate plotted as a logarithmic function of pressure.

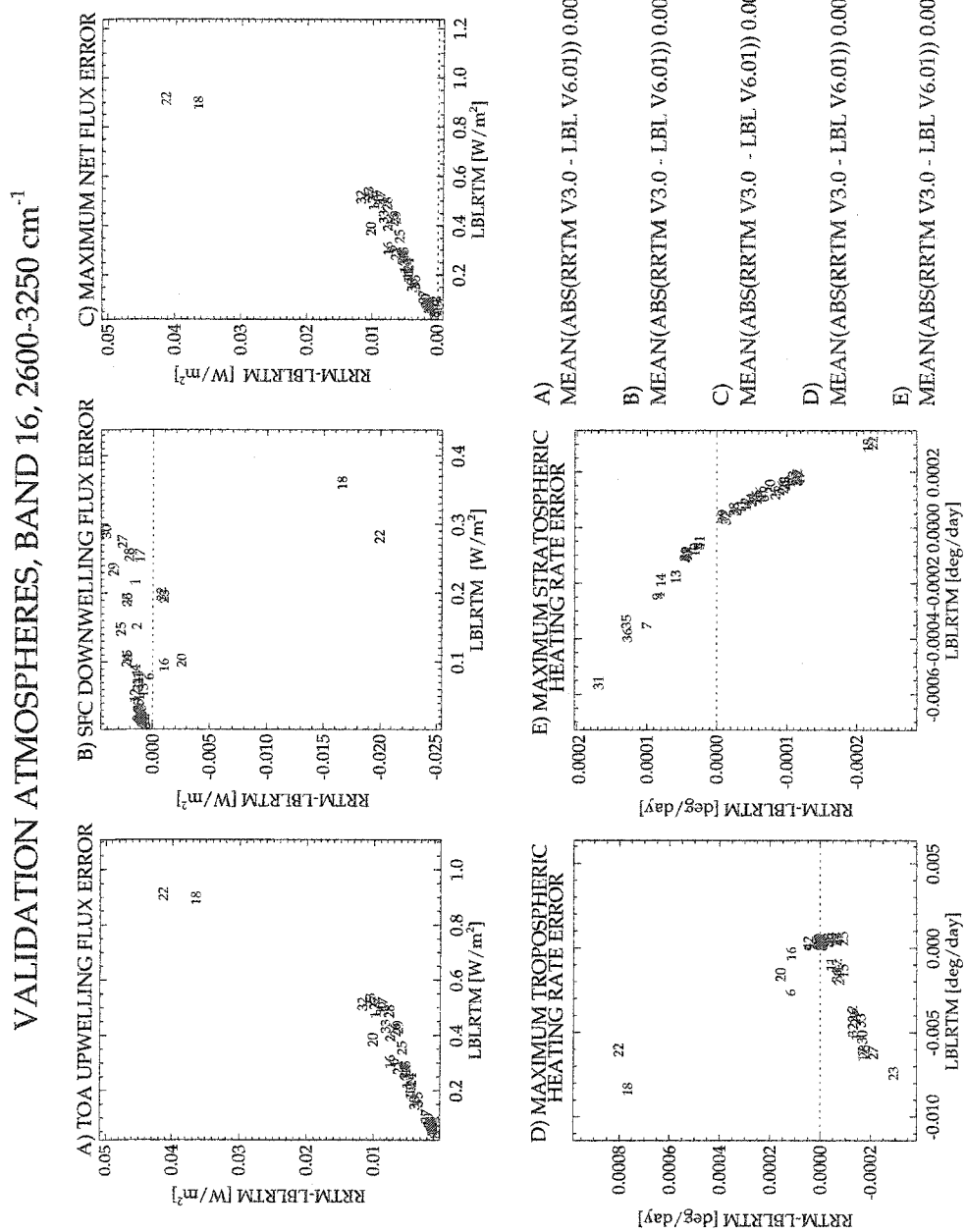

Figure A.17. Band 16 RRTM residuals for *Garand et al.* [2001] atmospheres. Band 16 (2600-3250 cm^{-1}) differences between RRTM and LBLRTM for 42 atmospheric profiles for a) upward flux at the top of the atmosphere, b) downward flux at the surface, and the maximum residual in c) net flux, d) tropospheric cooling rate, and e) stratospheric cooling rate plotted as a logarithmic function of pressure.

Bibliography

Albrecht, B., M. Pellot, and S. Cox, Pyrgeometer measurements from aircraft, *Rev. Sci. Instrum.*, *45*, 33, 1974.

Barker, H., G. Stephens, J. Bergman, K. Campana, S. Clough, J. Delamare, K. Evans, S. Freidenreich, Y. Hou, J. Li, J.-J. Morecrette, P. Raisanen, B. Ritter, M. Schlesinger, P. Sporyshev, M. Wendisch, F. Yang, P. Partain, B. Bonnel, E. Clothiaux, S. Cusack, J. Edwards, Y. Fouguart, V. Galin, S. Kato, E. Mlawer, W. O'Hirok, V. Ramaswamy, E. Rozanov, K. Shitata, Z. Sun, and N. Wood, Assessing 1D atmospheric solar radiative transfer models: Interpretation and handling of unresolved clouds, *J. Clim.*, 2002, in submission.

Bates, J. J., X. Wu, and D. L. Jackson, Interannual variability of upper tropospheric water vapor band brightness temperature, *J. Clim.*, *9*, 427, 1996.

Best, F., H. Revercomb, D. LaPorte, R. Knuteson, and W. Smith, Accurately calibrated airborne and ground-based Fourier Transform Spectrometers II: HIS and AERI calibration techniques, traceability, and testing, in *Council for Optical Radiation Measurements Annual Meeting*, National Institutde of Standards and Technology, Gaithersburg, MD, 1997.

Borysow, A., and L. Frommhold, Collision-induced rototranslational absorption spectra of n_2-n_2 pairs for temperatures from 50 to 300 k, *Astrophys. Journal*, *311*, 1043, 1986.

Cess, R. D., and et al., Comparison of the seasonal change in cloud-radiative forcing from atmospheric general circulation models and satellite observations, *J. Geophys. Res.*, *102*, 16593, 1997.

Chou, M.-D., W. Ridgway, and M. Yan, Parameterizations for water vapor IR radiative transfer in both the middle and lower atmospheres, *J. Atmos. Sci.*, 1995.

Clough, S., and M. Iacono, Line-by-line calculation of atmospheric fluxes and cooling rates 2. application to carbon dioxide, ozone, methane, nitrous oxide and the halocarbons, *J. Geophys. Res.*, 1995.

Clough, S., F. Kneizys, R. Davies, R. Gamache, and R. Tipping, *Atmospheric Water Vapor*, chap. Theoretical line for for H_2O vapor: application to the continuum, p. 25. Academic Press, 1980.

Clough, S., M. Iacono, and J. Moncet, Line-by-line calculations of atmospheric fluxes and cooling rates: Application to water vapor, *J. Geophys. Res., 97*, 15,761 , 1992.

Clough, S. A., F. X. Kneizys, and R. W. Davies, Line shape and the water vapor continuum, *Atmos. Res., 23*, 229, 1989.

Clough, S. A., P. D. Brown, C. Andronache, E. Mlawer, T. Shippert, D. Turner, D. Tobin, H. Revercomb, and R. Knuteson, A longwave broadband QME based on ARM pyrgeometer and AERI measurements, in *Proceedings of the 10th Annual ARM Science Team meeting*, U. S. Department of Energy, 2000.

Dehne, K., U. Bergholter, and F. Kasten, IEA comparison of longwave radiometers in Hamburg 1989-1990, Technical report, Meteorol. Obs. Hamburg, Hamburg, Germany, 1993.

Dudhia, J., D. Gill, K. Manning, A. Bourgeois, W. Wang, and C. Bruyere, PSU/NCAR mesoscale modeling system tutorial class notes and user's guide: MM5 system modeling Version 3, Technical report, National Center for Atmospheric Research, 2002.

Duvel, J. P., S. Bony, and H. LeTreut, Clear-sky greenhouse sensitivity to sea surface temperature changes: An evaulation of amip simulations, *Clim. Dyn., 13*, 259, 1997.

Ebert, E. E., and J. A. Curry, A parameterization of ice cloud optical properties for climate models, *J. Geophys. Res., 97*, 3831, 1992.

Ellingson, R. G., J. Ellis, , and S. Fels, The intercomparison of radiation codes used in climate models: Longwave results, *J. Geophys. Res., 96*, 8929 , 1991.

Engelen, R. J., L. D. Fowler, P. J. Gleckler, and M. F. Wehner, Sampling strategies for the comparison of climate model calcualted and satellite observed brightness temperatures, *J. Geophys. Res., 105,* 9393, 2000.

Evans, K., The spherical harmonic method discrete ordinate method for three-dimensional radiative transfer, *J. Atmos. Sci., 55,* 429, 1998.

Feltz, W., W. Smith, R. Knuteson, H. Revercomb, H. Woolf, and H. Howell, Meteorological applications of temperature and water vapor retrievals from the Ground-Based Atmospheric Emitted Radiance Interferometer AERI, *37,* 857, 1998.

Feltz, W., R. Knuteson, H. Howell, and R. Petersen, AERI Plus retrieval developments at the DOE ARM sites, in *Proceedings of the 11th Annual ARM Science Team meeting,* U.S. Department of Energy, Atlanta, GA, 2001.

Fu, Q., and K. N. Liou, On the correlated k-distribution method for radiative transfer in nonhomogeneous atmospheres, *J. Atmos. Sci.,* 1992.

Fu, Q., P. Yang, and W. B. Sun, An accurate parameterizatin of the infrared radiative properties of cirrus clouds for climate models, *J. Clim., 11,* 2223 , 1998.

Garand, L., D. Turner, M. Larocque, J. Bates, S. Boukabara, P. Brunel, F. Chevallier, G. Deblonde, R. Engelen, M. Hollingshead, D. Jackson, G. Jedlovec, J. Joiner, T. Kleespies, D. McKague, L. McMillin, J. Moncet, J. Pardo, P. Rayer, E. Salathe, R. Saunders, N. Scott, P. V. Delst, and H. Woolf, Radiance and jacobian intercomparison of radiative transfer models applied to HIRS and AMSU channels, *J. Geophys. Res.,* 2001.

Goody, R., R. West, L. Chen, and D. Crisp, The correlated-k method for radiation calculations in nonhomogeneous atmospheres, *J. Quant. Spectroscop. Radiat. Transfer,* 1989.

Goody, R. M., and Y. L. Yung, *Atmospheric Radiation: Theoretical Basis,* second ed., Oxford University Press, New York, NY, 1989.

Hu, Y. X., and K. H. Stamnes, An accurate parameterization of the radiative properties of water clouds suitable for use in climate models, *J. Clim., 6,* 728 , 1993.

Iacono, M., E. J. Mlawer, S. A. Clough, and J.-J. Morcrette, Impact of an improved longwave radiation model, rrtm, on the energy budget and thermodynamic properties of the ncar community climate model, ccm3, *J. Geophys. Res., 105*, 14873, 2000.

Iacono, M. J., J. S. Delamere, E. J. Mlawer, and S. A. Clough, Evaluation of upper tropospheric water vapor in the NCAR community climate model, CCM3, using modeled and observed HIRS radiances, *J. Geophys. Res., 108*(D2), 2003.

IPCC, The regional impacts of climate change: An assessment of vulnerability, a special report of the IPCC working group II, Cambridge University Press, United Kingdom, 1997.

Kiehl, J. T., J. J. Hack, G. B. Bonan, B. A. Boville, D. L. Williamson, and P. J. Rasch, The national center for atmospheric research community climate model:CCM3, *J. Clim., 11*, 1151, 1998.

Knuteson, R., F. Best, H. Revercomb, D. Tobin, and P. vanDelst, AERI status and forward model progress, in *Proceedings of the 6th Annual ARM Science Team meeting*, U.S. Department of Energy, Tucson, AZ, 1998.

Lacis, A., and V. Oinas, A description of the correlated k distribution method for modeling nongray gaseous absorption, thermal emission, and multiple scattering in vertically inhomogeneous atmosphere, *J. Geophys. Res.*, 1991.

Lafferty, W. J., A. M. Solodov, A. Weber, W. B. Olson, and J. M. Hartmann, Infrared collision-induced absorption by n_2 near 4.3 microns for atmospheric applications: Measurements and empirical modeling, *Appl. Optic*, 1996.

Liljegren, J., *Microwave Radiometry and Remote Sensing of the Earth's Surface and Atmosphere*, chap. Observations of integrated water vapor and cloud liquid water at the SHEBA ice station, p. 155. VSP Press, 2000a.

Liljegren, J., *Microwave Radiometry and Remote Sensing of the Earth's Surface and Atmosphere*, chap. Automatic self-calibration of ARM microwave radiometers, p. 433. VSP Press, 2000b.

Liou, K. N., *Radiation and Cloud Processes in the Atmosphere*, no. 20 in Oxford Monographs on Geology and Geophysics, Oxford University Press, New York, NY, 1992.

Marty, C., R. Philipona, J. Delamere, , E. Dutton, J. Michalsky, K. Stamnes, R. Storvold, T. Stoffel, S. Clough, and E. Mlawer, Longwave irradiance uncertainty under arctic atmospheres: Comparisons between measured and modeled downward longwave fluxes, *J. Geophys. Res.*, 2003, in review.

Miller, E., J. Wang, and H. Cole, Correction for dry bias in Vaisala radiosonde RH data, in *Proceedings of the 9th Annual ARM Science Team meeting*, U. S. Department of Energy, San Antonio, TX, 1999.

Mlawer, E., and S. A. Clough, On the extension of rapid radiatve transfer model to the shortwave region, in *Proceedings of the 6th Annual ARM Science Team meeting*, U. S. Department of Energy, 1996.

Mlawer, E., S. Taubman, P. Brown, M. Iacono, and S. Clough, Radiative transfer for inhomogeneous atmospheres: RRTM a validated correlated-k model for the longwave, *J. Geophys. Res., 102*, 16,663 , 1997.

Mlawer, E., P. Brown, S. Clough, L. Harrison, J. Michalsky, P. Kiedron, and T. Shippert, Comparison of spectral direct and diffuse solar irradiance measurements and calculations for cloud-free conditions, *Geophys. Res. Let, 27*, 2653, 2000.

Mlawer, E. J., S. A. Clough, P. D. Brown, T. M. Stephen, J. C. Landry, A. Goldman, and F. J. Murcray, Observed atmospheric collision-induced absorption in near-infrared oxygen bands, *J. Geophys. Res., 103*, 3859, 1998.

Moncet, J., and S. Clough, Accelerated monochromatic radiative transfer for scattering atmospheres: Application of a new model to spectral radiance observations, *J. Geophys. Res., 102*, 21853, 1997.

Morcrette, J.-J., The surface downward longwave radiation in the ECMWF forecast system, *J. Clim., 15*, 1875, 2002.

Morcrette, J. J., E. J. Mlawer, M. J. Iacono, and S. A. Clough, Impact of the radiation-transfer scheme RRTM in the ECMWF forecasting system, *ECMWF Newsletter*, (91), 2001.

Philipona, R., E. Dutton, T. Stoffel, J. Michalsky, O. Reda, A. Stifter, P. Wendling, N. Wood, S. Clough, E. Mlawer, G.Anderson, H. Revercomb, and T. Shippert, Atmospheric long-wave irradiance unvertainty: Pyrgeometers compared to an absolute sky-scanning radiometer, atmospheric emitted radiance interferometer, and radiative transfer model calculations, *J. Geophys. Res.*, *22*, 28129, 2001.

Pinto, J., J. Curry, and C. Fairall, Radiative characteristics of the Arctic atmosphere during spring as inferred from ground-based measurements, *J. Geophys. Res.*, *102*, 6941, 1997.

Revercomb, H., H. Buijs, H. Howell, D. LaPorte, W. Smith, and L. Sromovsky, Radiometric calibration of IR Fourier transform spectrometers: solultion to a problem with the High-Resolution Interferometer Sounder, *App. Optics*, *27*, 3210, 1988.

Revercomb, H., F. A. Best, R. O. Knuteson, B. A. Whitney, T. P. Dirkx, R. G. Dedecker, R. K. Garcia, P. van Delst, W. L. Smith, and H. B. Howell, Atmospheric emitted radiance interferometer, part i: Status, basic radiometric accuracy, and unexpected errors and solutions, in *Proceedings of the 6th Annual ARM Science Team meeting*, U. S. Department of Energy, San Antonio, TX, 1996.

Revercomb, H., D. Turner, D. Tobin, R. Knuteson, W. Feltz, J. Barnard, J. Bosenberg, S. Clough, D. Cook, R. Ferrare, J. Goldsmith, S. Gutman, R. Halthore, B. Lesht, J. Liljegren, H. Linne, J. Michalsky, V. Morris, W. Porch, S. Richardson, B. Schmid, M. Splitt, T. V. Hove, E. Westwater, and D. Whiteman, The Atmospheric Radiation M measurement (ARM Program's water vapor intensive observation periods: Overview, initial accomplishments and future challenges, *Bull. Amer. Meteor. Soc.*, 2002, in submission.

Ridgway, W. L., A. Harshvardhan, and A. Arking, Computation of atmospheric cooling rates by exact and approximate methods, *J. Geophys. Res.*, *96*, 8969, 1991.

Rosenkranz, P., Pressure broadening of rotational bands, 2: Water vapor from 300 to 100 cm^{-1}, *J. Chem. Phys.*, *87*, 163, 1987.

Rothman, L., C. Rinsland, A. Goldman, S. Mussie, D. Edwards, J. Flaud, A. Perrin, C. Camy-Peyret, V. Dana, J. Mandin, J. Schroeder, A. McCann, R. Gamache, R. Wattson, K. Yoshino, K. Change, K. Jucks, L. Brown, V. Nemtchinov, and P. Varanasi, The HITRAN molecular spectroscopic database and HAWKS (HITRAN Atmospheric Workstation): 1996 Edition, *J. Quant. Spectroscop. Radiat. Transfer, 60*, 665, 1998.

Salathe, E. P., D. Chesters, and Y. C. Sud, Evaluation of upper tropospheric moisture climatology in a general circulation model using TOVS radiance observations, *J. Clim., 8*, 2404, 1995.

Salby, M. L., *Fundamentals of Atmospheric Physics*, no. 61 in International Geophysics Series, Academic Press, San Diego, CA, 1996.

Serreze, M., R. Barry, and J. Walsh, Atmospheric water vapor characteristics at 70 degrees north, *J. Clim., 8*, 719, 1995.

Shephard, M., S. Clough, J. Delamere, D. Tobin, D. Turner, H. Revercomb, R. Knuteson, and R. Beer, Validation of co2 line parameters used in temperature retrievals, in *Fourier Transform Spectroscopy Proceedings*, Optical Society of America, Quebec City, Canada, 2003, in submission.

Soden, B., and F. P. Bretherton, Evaluation of water vapor distribution in general circulation models using satellite observations, *J. Geophys. Res., 99*, 1187, 1994.

Soden, B., S. Tjemkes, J. Schmetz, R. Saunders, J. Bates, B. Ellingson, R. Engelen, L. Garand, D. Jackson, G. Jedlovec, T. Kleespies, D. Randel, P. Rayer, E. Salathe, D. Schwarzkopf, N. Scott, B. Sohn, S. de Souza-Machado, L. Strow, D. Tobin, D. Turner, P. van Delst, and T. Wehr, An intercomparison of radiation codes for retrieving upper-tropospheric humidity in the 6.3-μ band: A report from the first GVAP workshop, *Bull. Amer. Meteor. Soc., 81*, 797, 2000.

Stamnes, K., S. Tsay, W. Wiscombe, and K. Jayaweera, Numerically-stable algorithm for discrete ordinate method radiative transfer in multiple scattering and emitting layered media, *App. Optics, 27*, 2502, 1988.

Stamnes, K., R. Ellingson, J. Curry, J. Walsh, and B. Zak, Review of science issues and deployment strategies for the North Slope of Alaska/Adjacent Arctic Ocean (NSA/AAO) ARM site, *J. Clim., 12*, 46, 1999.

Sun, Z., and L. Rikus, Improved application of exponential sum fitting transmissions to inhomogenous atmosphere, *J. Geophys. Res.*, 1999.

Sun, Z., and L. Rikus, Investigation of accuracy and efficiency of correlated-k distribution method, in edited by W. L. Smith and Y. Timofeyev, *IRS 2000: Current problems in atmopsheric radiation*, International Radiation Symposium, St. Petersburg, Russia, 2001.

Thibault, F., V. Menoux, R. L. Doucen, L. Rosenman, J. M. Hartmann, and C. Boulet, Infrared collision-induced absorption by o_2 near 6,4 mincrons for atmospheric applications: measurements and empirical modeling, *Appl. Opt., 36*, 563, 1997.

Thomas, G. E., and K. H. Stamnes, *Radiative Transfer in the Atmopshere and Ocean*, Atmospheric and Space Science Series, Cambridge University Press, Cambridge, UK, 1999.

Tobin, D., R. Knuteson, and H. Revercomb, Observed and calculated downwelling longwave spectral radiances at the SHEBA ice station: Prelude to an Arctic AERI/LBLRTM qme, in *Proceedings of the 10th Annual ARM Science Team meeting*, U. S. Department of Energy, San Antonio, TX, 2000.

Tobin, D. C., F. Best, P. Brown, S. Clough, R. Dedecker, R. Ellingson, R. Garcia, H. Howell, R. Knuteson, E. Mlawer, H. Revercomb, J. Short, P. van Delst, and V. Walden, Downwelling spectral radiance observations at the SHEBA ice station: Water vapor continuum measurements from 17 to 26 μm, *J. Geophys. Res., 104*, 2081, 1999.

Valley, S. (Ed.), *Handbook of Geophysics and Space Environment*, Air Force Cambridge Research Laboratories, Bedford, MA, 1965.

Walden, V. P., S. G. Warren, and F. J. Murcray, Measurement of the downwelling longwave radiation spectrum over the antarctic plateau and comparison with a line-by-line radiative transfer model for clear skies, *J. Geophys. Res., 103*, 3825, 1998.

Wang, J., H. Cole, D. Carlson, E. Miller, and K. Beierle, Corrections of humidity measurement errors from the Vaisala RS80 Radiosonde - application to TOGA COARE data, *J. Atmos. Oceanic Technol., 19*, 981, 2002.

West, R., D. Crisp, and L. Chen, Mapping transformations for broadband atmospheric radiation calculations, *J. Quant. Spectroscop. Radiat. Transfer, 43*, 191, 1990.

Wiscombe, W. J., Extension of the doubling method to inhomogeneous sources, *J. Quant. Spectroscop. Radiat. Transfer, 16*, 477, 1976.

Wu, X., J. J. Bates, and S. J. Khalsa, A climatology of the water vapor band brightness tempearutes from noaa operational satellites, *J. Clim., 6*, 1282, 1993.

Zhu, X., On overlapping absorption of a gas mixture, *Theor. Appl. Climatol., 52*, 139, 1995.